Spring 2022

Analysis of Turbulence in the Near-Shore Marine Atmospheric Surface Layer Using Sonic Anemometer Data

Alberto Javier Bodoque Garcia
University of New Hampshire, Durham

ANALYSIS OF TURBULENCE IN THE NEAR-SHORE MARINE ATMOSPHERIC SURFACE LAYER USING SONIC ANEMOMETER DATA

BY

ALBERTO JAVIER BODOQUE GARCIA

BS, Industrial Engineering, Universidad Carlos III de Madrid, 2019

THESIS

Submitted to the University of New Hampshire
in Partial Fulfillment of
the Requirements for the Degree of

Master of Science

in

Mechanical Engineering

May, 2022

This thesis has been examined and approved in partial fulfillment of the requirements for the degree of Master of Science in Mechanical Engineering by:

Thesis Director, Christopher White,
Department Chair and Professor of Mechanical Engineering

Ivaylo Nedyalkov,
Senior Lecturer of Mechanical Engineering

Juan C. Cuevas Bautista,
Lecturer of Mechanical Engineering

On 5/5/2022

Original approval signatures are on file with the University of New Hampshire Graduate School.

This thesis is dedicated to my friends and family, who have continuously supported me through the process of completing this Masters of Science in Mechanical Engineering.

ACKNOWLEDGMENTS

I would like to thank Professor White for his constant support and Danny, for sharing with me the data he collected from the installed sonic anemometers in Wood Island and Newcastle. Without them, completing this thesis would have not been possible.

TABLE OF CONTENTS

LIST OF TABLES

Table **Page**

LIST OF FIGURES

Figure **Page**

ABSTRACT

Analysis of Turbulence in the Near-Shore Marine Atmospheric Surface Layer Using Sonic Anemometer Data

by

Alberto Javier Bodoque Garcia

University of New Hampshire, May, 2022

This thesis investigates turbulence in the marine atmospheric boundary layer (MABL), above, the wave boundary layer (WBL). To conduct this research, wind velocity and temperature data was collected by a sonic anemometer located on Wood, Island, NH, mounted to a tower 4 meters above the ground. To study turbulence in the MABL, variables such as Reynolds stress and friction velocity were calculated for different days in August 2019. Friction velocity was calculated following three different approaches: the first approach employs the eddy covariance method, the second employs a tilt correction to the eddy covariance method, and the third uses the Reynolds stress tensor invariants to calculate friction velocity, which eliminates the need for tilt correction. The three methods showed similar results for most of the days investigated. Lastly, the Monin-Obukhov Similarity Theory (MOST) was studied with the purpose of investigating how the Reynolds stress tensor invariants method for calculating friction velocity responds to scaling laws such as MOST. This analysis showed that friction velocity values are greater for the Reynolds stress tensor invariants method than for the eddy covariance method with tilt correction. Overall, the Reynolds stress tensor invariants method does not reproduce well the friction velocity values obtained from the eddy covariance method with tilt correction for any of the stability conditions of the MABL.

CHAPTER 1

INTRODUCTION

1.1 General Overview of Wave Boundary Layers

Over the past decades, important research efforts have been concerned with understanding and modeling nearshore wind-wave interaction and turbulence transport in the wave boundary layer (WBL). The wave boundary layer is the lowest part of the marine atmospheric boundary layer (MABL) above the air-sea interface and its structure and dynamics are influenced directly by surface waves. Within the WBL, a portion of momentum transfer results from wave-produced fluctuations of pressure, velocity and stresses. This is commonly called the wave-produced momentum flux (WPMF). The typical height of the WBL is defined from the formula in equation 1.1, where k_p and w_p are the peak wave-number and frequency of the wave spectrum and g is the gravitational acceleration [1]:

$$h_{WBL} \approx k_p^{-1} = g w_p^{-2}. \tag{1.1}$$

The height of the WBL for short-period waves is of the order of magnitude 1/100 of the water depth. Above this height, the boundary layer will not affect the motion of the body of water, hence one-way coupling [2].

For rest scenarios (and also for short-period waves) an estimate of h_{WBL} was obtained from numerical modeling of wave-produced motions based on the two-dimensional Navier-Stokes equations. Using the Pierson-Moskowitz spectrum for estimation of significant wave height H_s the following relation is obtained [1]:

$$h_{WBL} = 3.7 H_s. \tag{1.2}$$

Equation 1.2 shows that the WBL height is approximately four times larger than the characteristic wave height. It is important also to comment that the main dynamic atmosphere-ocean interaction takes place in the lowest part of the WBL within a height of about H_s [1].

1.2 Analysis of Turbulence

Shear stress and friction velocity are two key parameters for the mathematical treatment of multiple processes occurring in the MABL, especially those linked to the vertical transport of momentum, or turbulence generation [3]. In certain terrains, the process of determining the turbulent friction velocity is complex and non-trivial. In this thesis three different methods for calculating the turbulent friction velocity in the MABL are used and their results are compared. The first uses the eddy covariance method for calculating friction velocity, the second method the eddy covariance method with tilt correction and the third uses the Reynolds stress tensor invariant method, which does not require tilt correction.

1.2.1 Eddy Covariance Method

The formula to calculate the friction velocity for the eddy covariance method is given in equation 1.3, where ρ is density, u_* is the friction velocity and $\overline{u'w'}$ is one of the six components of the Reynolds stress tensor appropriately averaged. In $\overline{u'w'}$, the prime indicates a variable in which the mean value has been subtracted, hence a fluctuating variable.

$$u_{cm}^{*\,2} = -\overline{u'w'}^2, \tag{1.3}$$

where u^*_{cm} is the friction velocity and "cm" indicates "Covariance Method".

1.2.2 Tilt Corrected Eddy Covariance Method

This method corrects for the tilt of the anemometer relative to the time averaged boundary. In flat terrains accounting for this tilt correction is relatively simple, while is less simple in complex

terrains. There are several techniques for tilt correction: planar fit correction, double rotation of the anemometers axes or triple rotation of the anemometers axes.

Of the different tilt correction techniques, the planar fit has shown less run-to-run stress errors and provides an unbiased estimate of the lateral stress. The double rotation of the anemometers axes technique has shown to have greater run-to-run stress errors and the triple rotation even longer run-to-run stress errors. In this work, the planar fit correction method is used to correct for the tilt of the anemometer [4]. The basis of this method is explained in chapter 4. Once the tilt correction is applied to the velocity vector, the friction velocity can be calculated from equation 1.4

$$u^*_{tccm}{}^2 = -\overline{u'w'}|^2_{tc}, \tag{1.4}$$

where u^*_{tccm} is the friction velocity and "tccm" indicates "Tilt Corrected Covariance Method" and "tc" is "Tilt Correction".

1.2.3 Reynolds Stress Tensor Invariant Method

This method uses the invariants of the Reynolds stress tensor to form a coordinate system that does not depend on the orientation of the anemometer.

$$\overline{u'_i u'_j} = \begin{bmatrix} \overline{u'u'} & \overline{u'v'} & \overline{u'w'} \\ \overline{u'v'} & \overline{v'v'} & \overline{v'w'} \\ \overline{u'w'} & \overline{v'w'} & \overline{w'w'} \end{bmatrix} \Longrightarrow \begin{bmatrix} \lambda_S & 0 & 0 \\ 0 & \lambda_M & 0 \\ 0 & 0 & \lambda_B \end{bmatrix}$$

As shown above, the Reynolds stress tensor can be expressed as a matrix where the invariants of the Reynolds stress tensor (also called eigenvalues) are located in the diagonal positions of the matrix, where λ_S the smallest and λ_B the biggest eigenvalue. λ_S is typically located in the upper left corner for convention. The three eigenvalues λ_S, λ_M, and λ_b represent the fundamental invariants of the turbulence acting in the directions of the corresponding eigenvectors Λ_S,Λ_M, and Λ_B [5]. Because they are invariants of the Reynolds stress tensor, the eigenvalues will be the same and eigenvectors will point in the same direction regardless of the coordinate system used to represent the data.

Consequently, it does not matter if the anemometer is tilted, as the eigenvalues and eigenvectors are always the same.

The friction velocity for the Reynolds stress invariant method can be obtained from equation 1.5, where β is the angle between the mean wind vector U and the plane defined by the largest and intermediate eigenvectors λ_B and λ_M.

$$u_{tim}^{*\,2} = -(\lambda_S - \lambda_B) sin\beta cos\beta, \tag{1.5}$$

where u_{tim}^* is the friction velocity (tim indicates "Tensor Invariant Method"), and λ_S and λ_B are the smallest and biggest eigenvalues, respectively [5].

An in-depth comparison of the results obtained using these three methods to determine the friction velocity will be presented in Chapter 4. For clarity, the eddy covariance method for calculating friction velocity is also referred in this thesis as "Covariance Method" or "CM", the eddy covariance method with tilt correction is as well referred as "Tilt Corrected Covariance Method" or "TCCM", while the friction velocity calculated using the Reynolds stress tensor invariants is also called "the tensor invariant method" or "TIM".

1.3 Monin–Obukhov Similarity Theory

In the MABL, three stability states exist: stable, neutral and unstable. In the stable state, turbulence and vertical fluxes are suppressed. The unstable state is defined by higher turbulence as well as an increased boundary layer height due to strong vertical motions. The neutral state usually appears for mean wind velocities greater than 15 m/s. In literature it can be found that, during a diurnal cycle, stable conditions are usually observed at night with cooler boundary temperatures while unstable conditions occur in day times with higher boundary temperatures [6].

Using the Monin–Obukhov similarity theory, a dimensionless length known as the Monin–Obukhov length is defined and used to classify the different stability states of the ABL. In this work, we use the Monin–Obukhov similarity theory to determine the influence, it any, of the stability state of the MABL on the friction velocity.

Equation 1.6 provides the definition of the Monin–Obukhov length, where κ is the von Karman constant equal to 0.41, g is the gravitational constant equal to 9.81 m^2/s, $\overline{w'T'}$ is the wall heat flux, $\overline{T_s}$ the mean temperature and u_* the turbulent friction velocity [7].

$$\frac{1}{\zeta} = \frac{-\kappa g}{\overline{T_s}} \frac{\overline{w'T'}}{u_*^3}. \tag{1.6}$$

In this thesis it will be consider that if $0 \leq \zeta < 1000$ then the MABL is stable, if $|\zeta| \geq 1000$ then the MABL is neutral and if $-1000 < \zeta < 0$ the MABL is unstable [8].

1.4 Research Objective

The research goals are:

1) to evaluate parameters such as wind direction, wind velocities, temperature, fluctuating velocities, Reynolds stresses and friction velocity within the MABL over 1 week in August 2019.

2) to investigate whether the Reynolds stress tensor invariant method for calculating friction velocity replicates well the results obtained using the eddy covariance method with and without using tilt correction.

3) to use the Monin–Obukhov similarity theory to study if using TIM similar results are obtained than when using TCCM for calculating friction velocity.

1.5 Approach

1) Compute and interpret wind direction, wind velocities, temperature, fluctuating velocities, Reynolds stresses and friction velocity using the velocity vector data acquired from the sonic anemometers. This will help us understand how these parameters change hourly, daily and weekly so we can understand better the changes in turbulence in a hourly, daily or weekly basis.

2) Compute turbulent friction velocity, first using the eddy covariance method, second using the eddy covariance method with tilt correction method and lastly using the Reynolds stress tensor invariant method. Then, to compare these three methods to understand similarities and differences.

3) Use the Monin–Obukhov similarity theory to determine the stability of the MABL.

4) Evaluate if the Reynolds stress tensor invariant method replicates the eddy covariance method with tilt correction accurately in stable, neutral and unstable conditions.

1.6 Organization of the Thesis

The work presented in this thesis can be divided between an experimental part and an analytical part. The experimental part consisted of the installation of two different sonic anemometers in two different locations: Wood Island and New Castle, both locations located in the state of New Hampshire, in the seacoast region. These anemometers measured the instantaneous velocity vector in m/s and temperature in degrees Celsius. The analytical portion of this thesis included the calculation of fluctuating velocities, Reynolds stresses, wind direction, comparison of three different methods for calculating the friction velocity and the application of the Monin–Obukhov similarity theory to determine the stability of the MABL and to evaluate how the stability of the MABL affects the turbulence in the WBL as manifested on differences in the friction velocity.

CHAPTER 2

THEORY

2.1 Fluid Mechanics Overview

This section provides an overview of fluid dynamics and turbulence concepts needed to make the thesis self-contained.

2.1.1 Definition of a Fluid

Conventionally, three states of matter exist: solid, liquid and gas. Liquid and gas are both fluids, and unlike solids, continuously deform under the influence of an applied force. This deformation is associated with fluid flow [9].

2.1.2 Navier-Stokes Equations

For an incompressible, isothermal Newtonian fluid, conservation of mass is given by the so-called continuity equation

$$\overrightarrow{\nabla} \cdot \overrightarrow{v} = 0, \tag{2.1}$$

where $\overrightarrow{\nabla}$ is the gradient operator and $\overrightarrow{v}$ is the velocity vector field.
Newton's second law of motion is given by

$$\rho[\frac{\partial \overrightarrow{v}}{\partial t} + \overrightarrow{v} \cdot \nabla \overrightarrow{v}] = -\overrightarrow{\nabla} P + \mu(\nabla^2 \overrightarrow{v}) + \rho \overrightarrow{g}, \tag{2.2}$$

where ρ is the fluid mass density, P is pressure, ν is the fluid kinematic viscosity and $\overrightarrow{g}$ is the gravitational vector. For compactness, the gravitational body force is often embedded in the pressure term. The so-called momentum equation then takes the form

$$\rho[\frac{\partial \overrightarrow{v}}{\partial t} + \overrightarrow{v} \cdot \nabla \overrightarrow{v}] = -\overrightarrow{\nabla} P + \mu(\nabla^2 \overrightarrow{v}), \tag{2.3}$$

where the P in Eq. 2.3 includes the gravitational body force (hence it is different than in Eq 2.2). The left hand side of Eq. 2.3 corresponds to inertial forces and the first term in the right hand side corresponds to pressure forces, and the second term are the viscous forces.

2.1.3 Laminar vs Turbulent Flow

Fluid flows can either be laminar or turbulent. Classification of a flow into one of these two categories is typically through the magnitude of the Reynolds number, which is a non-dimensional variable that represents the ratio of inertial forces to viscous forces as given by

$$Re = \frac{UL}{\nu}, \tag{2.4}$$

where U is a characteristic velocity, L is a characteristic length scale and ν is the kinematic viscosity of the fluid.

Turbulent flows are associated with high Reynolds numbers, where inertial forces are large compared to viscous forces. One important characteristic of turbulent flows is irregularity or randomness that causes the instantaneous velocity in a turbulent flow to change rapidly in space and time. This irregularity requires the investigations of turbulence to rely on statistical methods. A common statistical method of analysis, the so-called Reynolds-averaged decomposition, is described below [10].

2.1.4 Reynolds Decomposition and RANS Equation

The instantaneous velocity is decomposed into a mean and a turbulent velocity fluctuation

$$u_i = U_i + u_i', \tag{2.5}$$

where subscript $i = 1, 2, 3$ represents the velocity components, typically denoted by u, v and w. Substituting Eq. 2.5 into Eq. 2.3, then averaging yields the so-called Reynolds-Averaged-Navier Stokes (RANS) equations

$$\frac{\partial U_i}{\partial x_i} = 0, \tag{2.6}$$

$$U_j \frac{\partial U_i}{\partial x_j} = -\frac{1}{\rho}\frac{\partial P}{\partial x_i} + \nu \frac{\partial^2 U_i}{\partial x_j \partial x_j} - \frac{\partial \overline{u_i' u_j'}}{\partial x_j}. \tag{2.7}$$

Equation 2.6 is the mean continuity equation and equation 2.7 is the mean momentum equation, the latter describing the mean dynamics of a turbulent flow. The term $\overline{u_i' u_j'}$ is the Reynolds stress and the last term in equation 2.7 represents the transport of momentum by the turbulent velocity fluctuations.

2.2 Boundary Layers over Rigid Walls

Boundary layers were first studied at the beginning of the 20th century by Ludwig Prandtl, a German physicist considered the father of modern aerodynamics. Prandtl predicted that for fluid flow over or through a fixed boundary, the effect of friction in the fluid is only important in a region adjacent to the solid boundaries, this region was termed the boundary layer [10]. One of the most important characteristics of a boundary layer is the "no-slip condition" which means that the flow velocity at the boundary is the same as the velocity of the boundary. The boundary layer ends when the free-stream region is reached, at a distance δ from the boundary as it can be seen in figure 2.1.

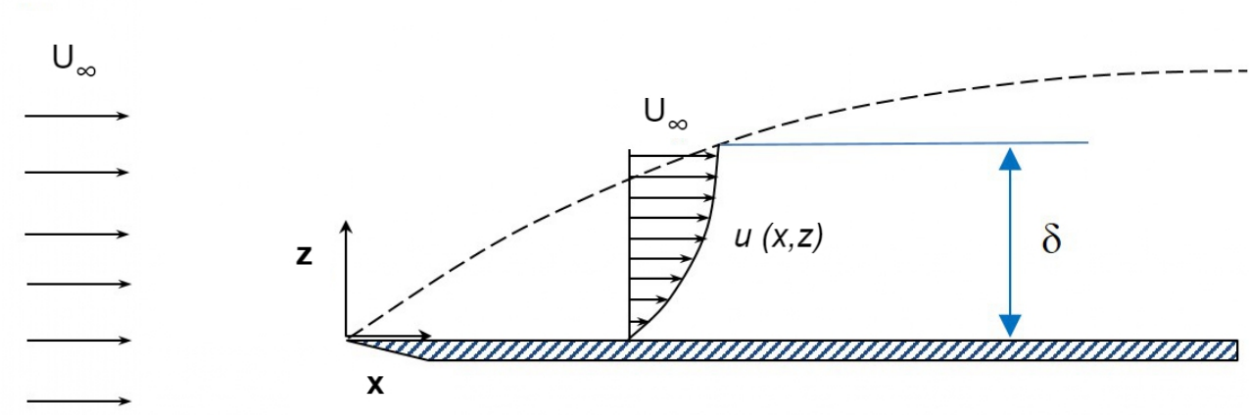

Figure 2.1. Boundary layer and free-stream regions [11].

In figure 2.1, it is observed that from $z = 0$ to $z = \delta$, U, which is the mean stream-wise velocity, increases with the vertical component z, in other words $\frac{\partial U}{\partial z} > 0$. After reaching the free-stream, $U = U_\infty$, and $\frac{\partial U}{\partial z} = 0$.

The RANS equation for the two-dimensional, zero pressure gradient boundary layer flow takes the form

$$U\frac{\partial U}{\partial x} + W\frac{\partial W}{\partial z} = \nu\frac{\partial^2 U}{\partial z^2} - \frac{\overline{u'w'}}{\partial z}, \tag{2.8}$$

where stream-wise pressure gradients associated with the normal Reynolds stresses are neglected. Integrating Eq. 2.8 in the z-direction and applying the no-slip boundary conditions yields an equation for the stresses.

$$\tau_w = \mu\frac{\partial U}{\partial z} - \rho\overline{u'w'} - \int_0^z \left(U\frac{\partial U}{\partial x} + W\frac{\partial W}{\partial z}\right) dz, \tag{2.9}$$

where τ_w is the wall shear stress and $\tau_w = \mu\frac{\partial u}{\partial z}|_{z=0}$.

In the vicinity of the wall, dimensional analysis shows that the last term on the RHS of Eq. 2.9 is small such that close to the wall

$$\tau_w = \mu \frac{\partial U}{\partial z} - \rho \overline{u'w'}. \tag{2.10}$$

The layer near the wall where Eq. 2.10 holds is known as the constant stress layer. Moreover, outside of the very thin viscous region close to the wall, the turbulent shear stress is many times greater than the viscous shear stress such that

$$\tau_w \approx -\rho \overline{u'w'}. \tag{2.11}$$

In brief, measurement of the Reynolds shear stress within the constant stress region and outside of the viscous region provides an estimate of the wall shear stress. The region of the flow corresponding to the constant stress region is $z^+ = 30 < z < 0.2Re_\delta$, where the + denotes normalization by the friction velocity $u_\tau = \sqrt{\tau_w}$ and ν and $Re_\delta = U_\infty \delta / \nu$.

2.3 Boundary Layers over Water

The boundary layer of over an air-water interface is different than the boundary layer over a rigid wall owing to the presence of waves. Specifically, waves can influence the dynamics at the boundary by adding wave-induced perturbations. It is common to use a triple decomposition of velocity such that

$$u_i = U_i + u_i' + \tilde{u}_i, \tag{2.12}$$

where the $\tilde{u}$ is the wave-induced u component of the velocity. The atmospheric surface layer near the air-water interface is often modeled as a constant stress region or constant momentum flux layer, i.e., $\frac{\partial \tau_{total}}{\partial z} = 0$, despite the fact that there is some flux divergence in the atmosphere.

The stresses in the constant stress region thus takes the form

$$\tau_{total} = \tau_w = \mu \frac{\partial U}{\partial z} - \rho \overline{u'w'} - \rho \overline{\tilde{u}\tilde{w}}, \tag{2.13}$$

where $\rho \overline{\tilde{u}\tilde{w}}$ denotes the contribution from the wave-induced perturbations. Similar to boundary layers over rigid wall, outside of the viscous region

$$\tau_{total} = \tau_w = -\rho\overline{u'w'} - \rho\overline{\tilde{u}\tilde{w}}. \tag{2.14}$$

The wave-induced stress component is a strong decaying function with height. The height over the air-water interface where the wave-induced perturbations are important define the wave boundary layer (WBL). As the wave-induced stress component decays, the momentum flux is fully supported by the turbulent flux in the so-called fully turbulent layer. Importantly, the turbulent flux in the fully turbulent layer will depend on the boundary condition provided by the viscous and wave-induced stresses at the interface.

Determining the decay of the wave-induced stress component with height above the air-water interface is nontrivial as direct measurement of the wave-induced velocity perturbations is difficult and deconvolving the wave-induced velocity from the instantaneous velocity is not possible. One approach, owed to Miles (1957), is the assumption that the wave-induced stress is constant across the WBL and sharply drops to zero at a critical height. The critical height is where the wind speed matches the phase speed of the dominant waves. While the Miles theory is useful, the step-like behavior for the wave-induced momentum flux is not physical. It is therefore typically assumed that the wave-induced momentum flux decays exponentially with height [12]. The decay rate is then determined by performing a stress-balance, i.e., fitting a decay rate such that the local stress converges to the total stress as measured in the fully turbulent layer.

In this thesis it is assumed that at the height above the air-water interface where the sonic anemometer measurements are acquired ($\approx$ 4m) is within the fully turbulent layer such that

$$u_* = \sqrt{\frac{\tau_w}{\rho}} \approx \sqrt{-\overline{u'w'}}, \tag{2.15}$$

where u_* is the friction velocity.

This assumption is consistent with the thickness of the WBL given by equation 1.2. Specifically the wave height at the measurement location are typically < 1 meter.

CHAPTER 3

DATA COLLECTION

3.1 Measurement Stations

In this study, two identical sonic anemometers were installed in two different locations on opposite sides of the Piscataqua river. One station is located at the Newcastle coast guard station, in coordinates 43.07, -70.71, and the other station is located on an island close to the shore called, Wood Island, in coordinates 43.06, -70.70. There is a 1.3 km distance between these stations. These two locations were chosen due to ocean proximity, given that an extensively analysis of the MABL was intended as part of a larger project.

Figure 3.1. In this figure are shown both locations were the sonic anemometers were installed: Newcastle in the top left corner and Wood Island in the bottom right corner.

3.2 Experiment Setup

In this section are described all the weather station components and how this tower was set up in place.

As stated before, both sonic anemometers were identical. The sonic anemometers deployed at the two sites were two Applied Technologies SATI/3A. Besides, a tripod was used so the measurements collected by the anemometer were at some height above the ground and also so the tower is more stable. Some straps are also used to stabilize even more the tower and try to correct any tilt that the instruments may have. Then a metal vertical bar was attached to the tripod. This bar had attached a solar panel so the anemometer could continue collecting data for long periods of time. It also had attached a box with all the electronics needed to run the anemometer (a battery, a device to operate the solar panels and several more electronics and power outlets). From this box using

a chord connected to one of the outlets it was possible to control the anemometer functionalities using a laptop. The sonic anemometer installed in Wood Island, NH can be seen in figure 3.2.

Figure 3.2. Weather station installed in Newcastle, NH.

The sonic anemometer is mounted close to the top of the tower as shown in figure 3.2. A graphical representation of the Applied Technologies SATI/3A sonic anemometer is shown in figure 3.3. The three pairs of transducers on three different axis allows the three dimensional wind speed vector to be measured.

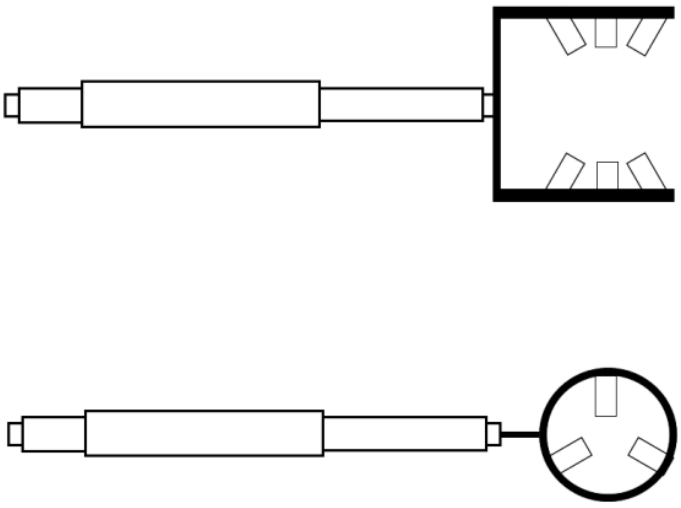

Figure 3.3. SATI/3A ultrasonic anemometer non-orthogonal design with 120° separation between transducers [13].

A sonic anemometer operates by measuring the transit time for a pulse of sound to travel between a pair of transducers. This time is dependent on the distance between the transducers, the speed of sound, and the air speed along the axis of the transducers. The equation for calculating transit time of the signal between the transducers can be seen in equation 3.1:

$$t = L\frac{\sqrt{c^2 - u_n^2} \pm u_d}{c^2 + u^2}, \tag{3.1}$$

where L is the distance between transducers, c is the speed of sound, u is the absolute velocity, u_n is the normal component of velocity and u_d is the parallel component of the velocity.

The parallel component of velocity is calculated following equation 3.2:

$$u_d = \frac{L}{2}(\frac{1}{t_1} - \frac{1}{t_2}), \tag{3.2}$$

where t1 and t2 are the transit times for the two other transducer pairs.

From the sound velocity measurements, the anemometers can be used to obtain sonic temperature information [13].

3.3 Data Collection and the Use of this Data

From these two sonic anemometers, velocities in the x, y and z axis and temperature were acquired. Velocity was measured in m/s and temperature in degrees Celsius. The SATI/3A sonic anemometers collect data at 200 Hz and output averaged data sets at 10 Hz.

Temperature and velocity measurements were obtained for several days between August and September 2019. For this work one continuous week of data was selected: August 14th of 2019 to August 20th of 2019. The data, originally in format .dat was converted into .mat files and loaded in Matlab as structure arrays, which is a Matlab data type that stores data using data containers called fields. The data for each day represented a structure array that contained 5 fields: u, v, w, T and the date of the obtained data with the corresponding time that it was measured.

CHAPTER 4

DATA ANALYSIS AND RESULTS

For this study, data from the sonic anemometer located on Wood Island is used.

4.1 Historical Weather Data for Newington, NH

For the purpose of being able to explain certain behaviors observed in the data, a study of different historical weather parameters was conducted. Weather data for Newington, NH, which is an area close to the sonic anemometer measurement sites, for August 14 to August 20, 2019 was collected and tabulated. The weather data provides parameters such as temperature, humidity, wind speed, pressure and precipitation as shown in table 4.1.

Table 4.1. Newington, NH Weather History from August 14, 2019 to August 20, 2019 [14].

Time	Temperature (K)			Humidity (%)			Wind Speed (m/s)			Pressure (Hg)			Precipitation (in)
Day	Max	Avg	Min	Max	Avg	Min	Max	Avg	Min	Max	Avg	Min	Total
August 1, 2019	303.2	297.0	291.5	98	63.2	33	4.5	2.7	0	30	29.9	29.9	0.16
August 2, 2019	301.5	294.9	287.6	85	54.1	29	5.4	2	0	30	30	29.9	0
August 3, 2019	302.0	295.0	289.8	94	76.9	56	4.5	2.4	0	29.9	29.9	29.8	0
August 4, 2019	299.8	295.3	289.3	93	67.6	36	6.3	2.1	0	29.8	29.8	29.7	0.27
August 5, 2019	300.4	292.9	284.8	91	61.5	32	4.5	2.2	0	29.9	29.9	29.8	0
August 6, 2019	299.3	293.8	288.2	100	82.8	48	6.7	2.7	0	29.8	29.8	29.7	0
August 7, 2019	301.5	294.9	290.9	100	93.3	65	8.9	2.2	0	29.7	29.7	29.7	0
August 8, 2019	302.6	296.2	292.6	100	81.5	49	6.7	3.4	0	29.7	29.5	29.5	1.51
August 9, 2019	301.5	295.9	290.9	90	63.6	37	5.8	3.5	1.3	29.6	29.5	29.5	0.01
August 10, 2019	298.2	293.1	289.3	80	61.2	41	5.4	3.5	1.3	29.7	29.6	29.6	0
August 11, 2019	298.7	292.9	287.0	82	61.9	41	5.4	3.4	0	29.8	29.8	29.7	0.11
August 12, 2019	302.0	295.8	288.7	86	63.6	43	4	2.8	1.3	29.8	29.7	29.7	0
August 13, 2019	300.9	296.0	292.6	100	80.7	64	4.5	2.3	0	29.7	29.6	29.6	0
August 14, 2019	296.5	293.2	289.8	100	82.1	58	4	2.3	0	29.8	29.7	29.7	0.4
August 15, 2019	296.5	291.4	288.2	100	86.7	53	4	1.4	0	30	29.9	29.9	0
August 16, 2019	296.5	291.6	289.8	100	94	71	5.4	2.1	0	30	29.9	29.9	0
August 17, 2019	295.4	293.1	291.5	99	92.3	83	4.5	3.2	0	30	29.9	29.9	0
August 18, 2019	300.4	294.1	290.9	100	93.3	68	5.8	1.7	0	29.9	29.9	29.8	0.06
August 19, 2019	305.4	297.3	293.7	100	85.4	47	6.7	2.5	0	29.8	29.8	29.7	0
August 20, 2019	301.5	296.5	290.9	85	62.5	34	6.3	2.6	0	29.9	29.9	29.8	0.07
August 21, 2019	298.7	294.4	288.7	100	91.2	68	3.6	1.4	0	29.9	29.8	29.7	0
August 22, 2019	303.7	298.5	292.6	99	75.7	47	5.4	2.4	0	29.7	29.7	29.6	0.08
August 23, 2019	298.2	294.3	288.7	72	59.4	43	4.5	2.8	0	29.9	29.8	29.8	0.04
August 24, 2019	294.8	290.8	285.4	86	69.3	53	5.4	2.5	0	30.2	30.1	29.9	0
August 25, 2019	292.6	289.7	285.9	87	71.8	55	5.8	4	1.3	30.3	30.2	30.2	0
August 26, 2019	294.8	289.2	283.2	92	67.7	41	5.8	2.5	0	30.2	30.1	30	0
August 27, 2019	297.6	288.8	255.4	97	68.8	0	5.4	1.8	0	30	28.7	0	0
August 28, 2019	297.0	292.1	288.7	100	84.9	53	6.7	3	0	29.9	29.8	29.7	0
August 29, 2019	301.5	294.3	290.9	99	78.2	42	4.5	2.3	0	29.8	29.7	29.6	1.04
August 30, 2019	302.0	295.4	287.6	93	63.6	40	6.3	3.1	1.3	29.9	29.8	29.8	0
August 31, 2019	298.2	292.9	287.6	84	58.7	33	6.3	3.3	0	30.2	30.1	29.9	0

In addition, data acquired hourly for each day of the week from August 14 to August 20, 2019 is provided in Appendix "Daily Historical Weather data for Newington, NH".

4.2 Wind Direction Analysis

For this study, V^+ is 0 degrees and represents wind from west to east, and U^+ is 90 degrees and represents wind from south to north. The rotation is counter-clockwise, where east is to the right, north is to the top, west is to the left and south is to the bottom of the trigonometric plane, as shown in figure 4.1.

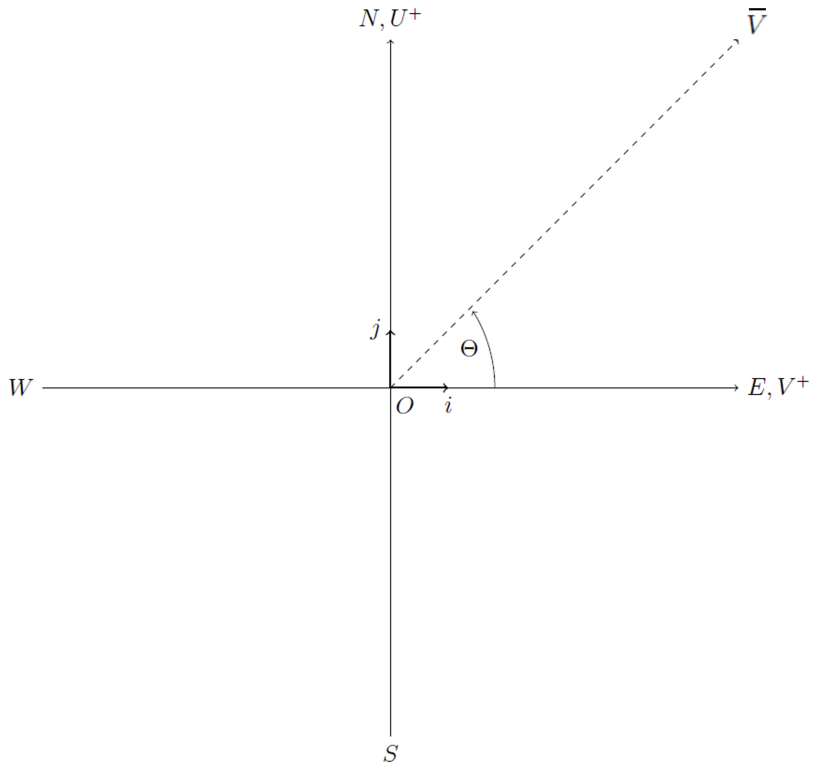

Figure 4.1. Coordinate axes and cardinal directions.

The dashed line indicates represents an arbitrary mean horizontal component of the velocity such that, $\overline{V} = Vcos\theta$ i $+Usin\theta$ j and $\theta = tan^{-1}(\frac{U}{V})$.

Figure 4.2 to figure 4.8, shows, for each day from August 14, 2019 to August 20, 2019, theta, representing the horizontal wind direction corresponding to degrees from V^+. The bottom figures shows, the angle the wind vector forms with each of the three coordinate axis.

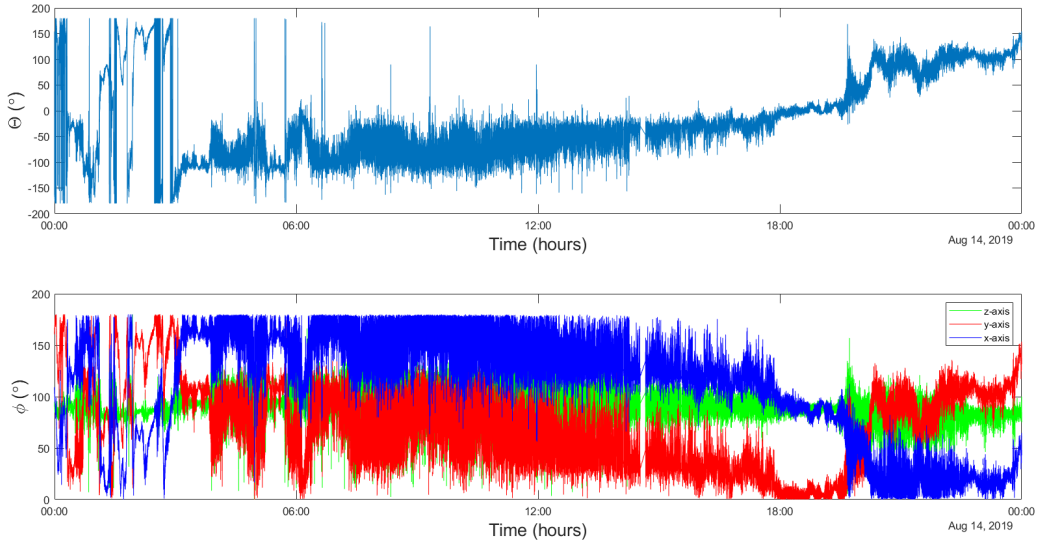

Figure 4.2. From Top to Bottom, Horizontal Wind Direction, "θ", vs Time and Wind Vector Angle with Coordinate Axis "ϕ" vs Time for August 14, 2019.

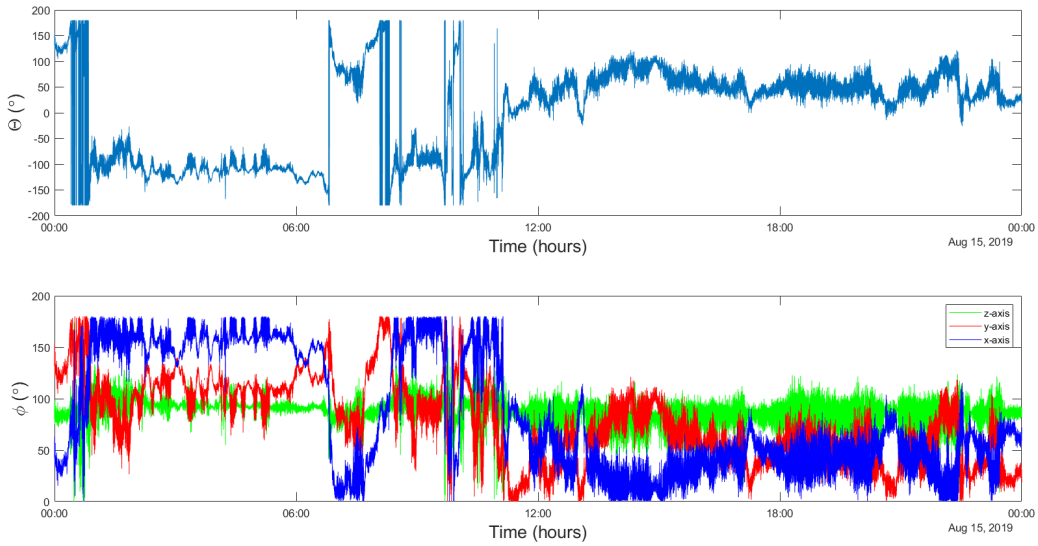

Figure 4.3. From Top to Bottom, Horizontal Wind Direction, "θ", vs Time and Wind Vector Angle with Coordinate Axis "ϕ" vs Time for August 15, 2019.

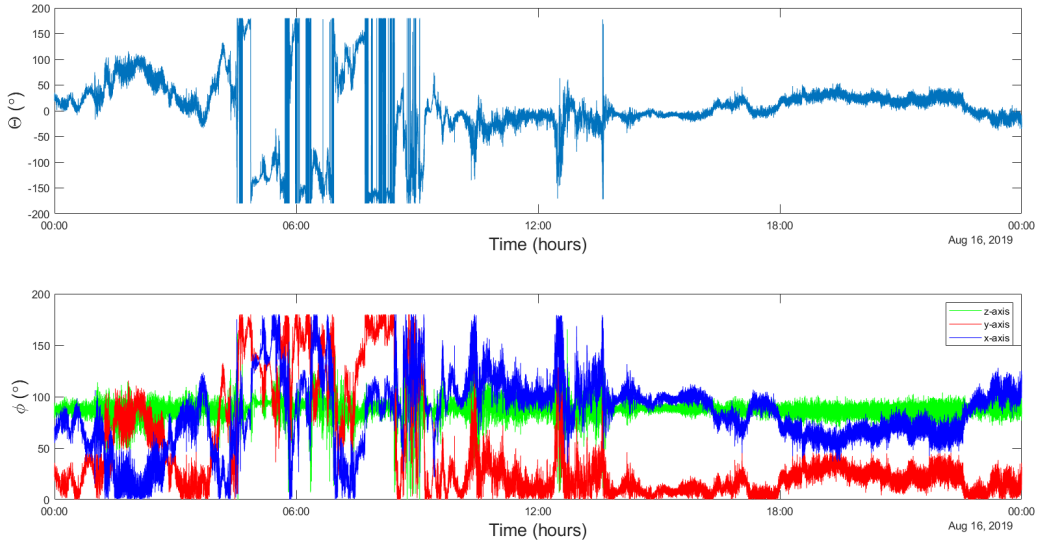

Figure 4.4. From Top to Bottom, Horizontal Wind Direction, "θ", vs Time and Wind Vector Angle with Coordinate Axis "ϕ" vs Time for August 16, 2019.

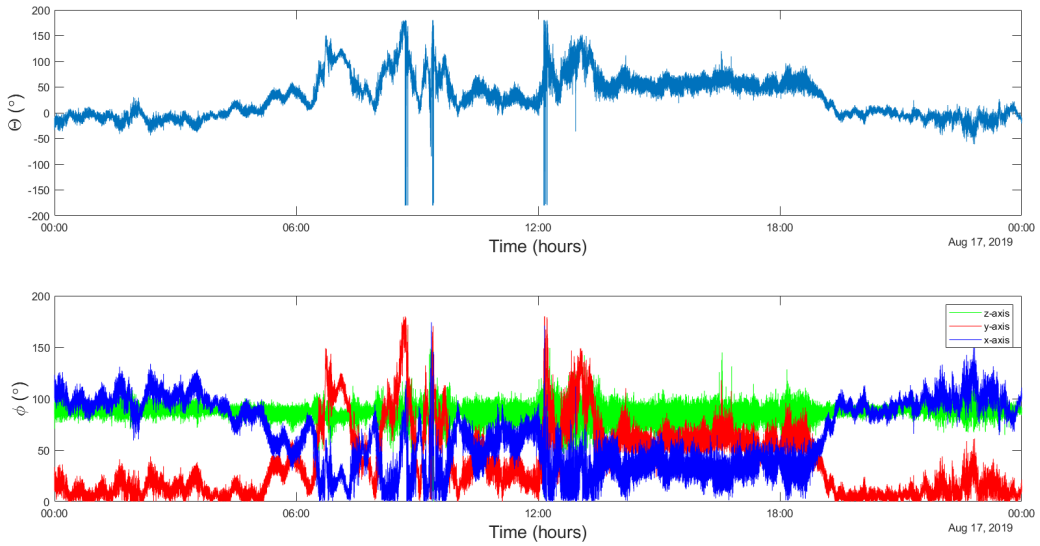

Figure 4.5. From Top to Bottom, Horizontal Wind Direction, "θ", vs Time and Wind Vector Angle with Coordinate Axis "ϕ" vs Time for August 17, 2019.

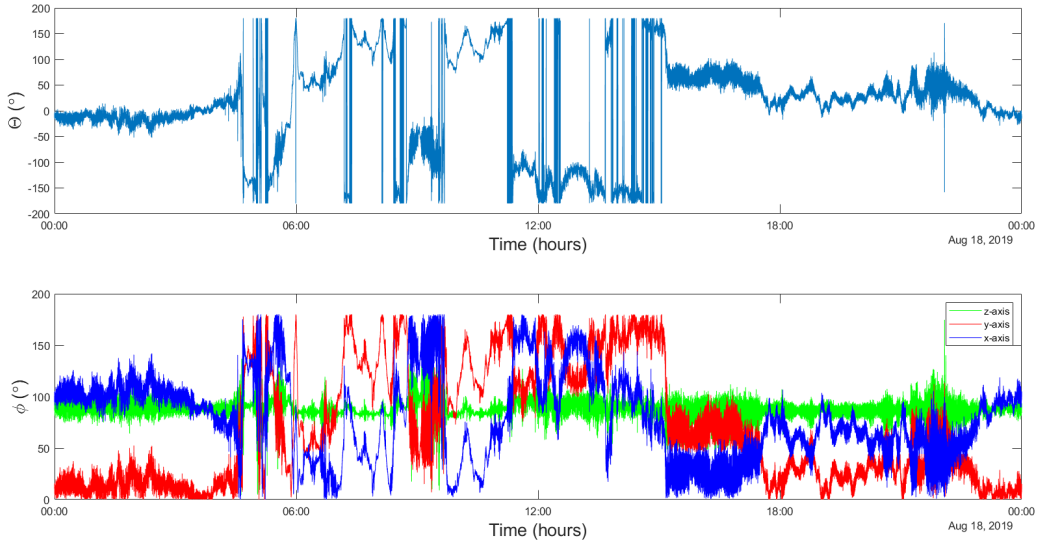

Figure 4.6. From Top to Bottom, Horizontal Wind Direction, "θ", vs Time and Wind Vector Angle with Coordinate Axis "ϕ" vs Time for August 18, 2019.

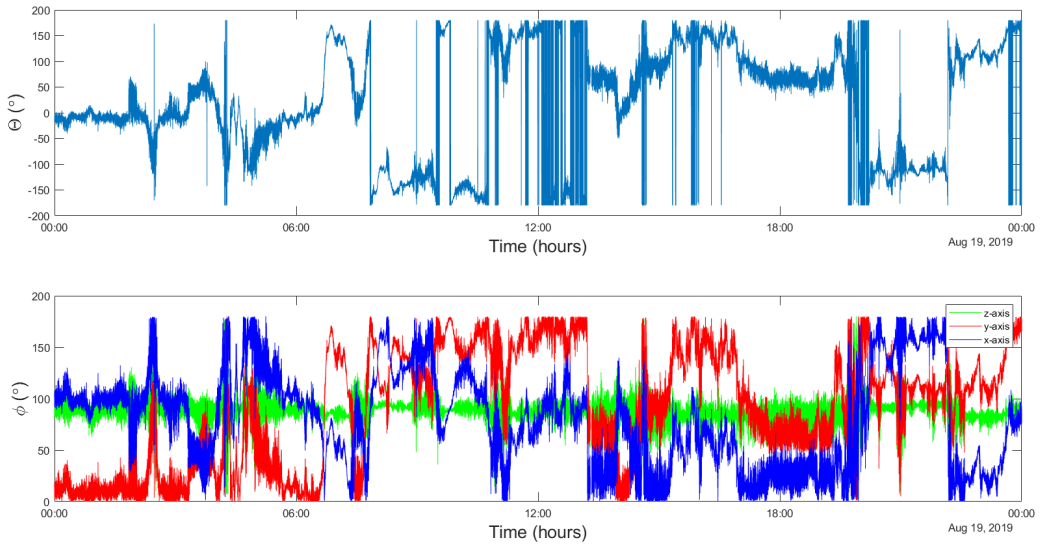

Figure 4.7. From Top to Bottom, Horizontal Wind Direction, "θ", vs Time and Wind Vector Angle with Coordinate Axis "ϕ" vs Time for August 19, 2019.

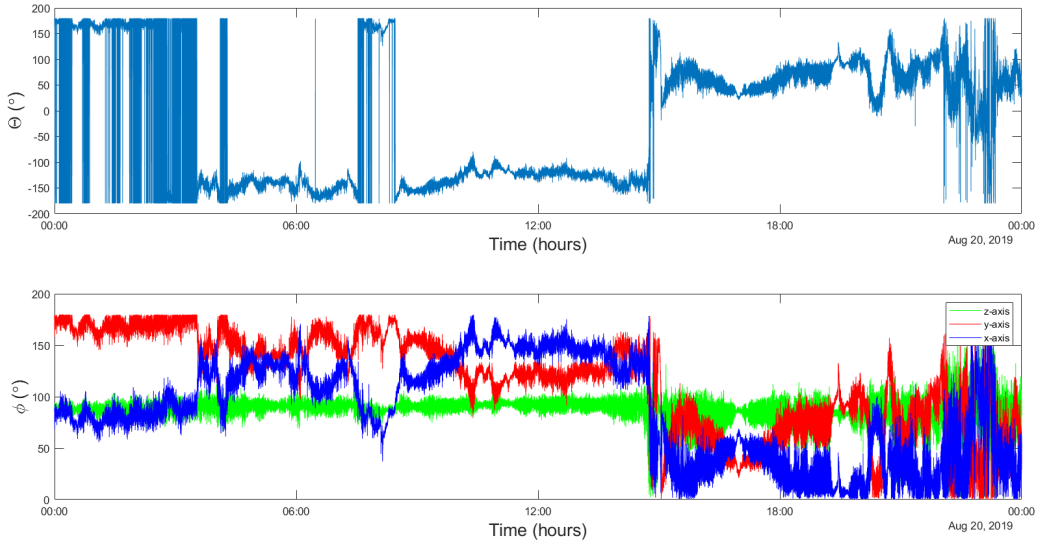

Figure 4.8. From Top to Bottom, Horizontal Wind Direction, "θ", vs Time and Wind Vector Angle with Coordinate Axis "ϕ" vs Time for August 20, 2019.

The main takeaways from the wind direction analysis are:

For August 14, 2019, at the end of the day U is dominant and positive and V is almost 0 and it can be seen how the horizontal wind angle is more or less 90 degrees, which represents north, which is what it is expected. For August 15, 2019, the wind changes direction by about 180 degrees. Wind direction for this day is steady for most of the day but highly variable from 6 am to 12 pm. For August 16, 2019, wind direction is steady for the majority of the day but highly variable from 5 am to 10 am. For August 17, 2019, it is clear that the u component increases from 6 am to 6 pm. For August 18, 2019, wind direction is extremelly variable from 6 am to 3 pm. For August 19, 2019, wind direction is highly variable most of the day and lastly, for August 20, 2019, we can see how wind direction is steady for most of the day but highly variable over a portion of the day. For this day, around 2 pm it can be observed a change of 180 degrees in wind direction.

It can be found that the angle between the wind vector and the z axis, which represents the vertical direction, is not exactly 90 degrees (e.g 86.77 degrees for August 17, 2019 or 87.27 degrees

for August 20, 2019). That means that there is some tilt in our weather station tower. Further on this analysis, tilt correction will be explored.

4.3 Removing Outliers from the Data

Once the data was extracted from the sonic anemometer and transformed in a format which Matlab could read (.mat files), the measured variables were plotted versus time. In all the plots, data outliers were evident. To identify an outlier, the technique of the moving median was utilized with a window length of 5. An outlier was considered to be a value that was more than three local scaled median absolute deviations from the local median within the moving window. Once an outlier was identified, it was replaced by a NaN. In other words, outliers were simply eliminated from the data and not replaces. The results of removal of outliers from the data can be seen in figures 4.9 - 4.15.

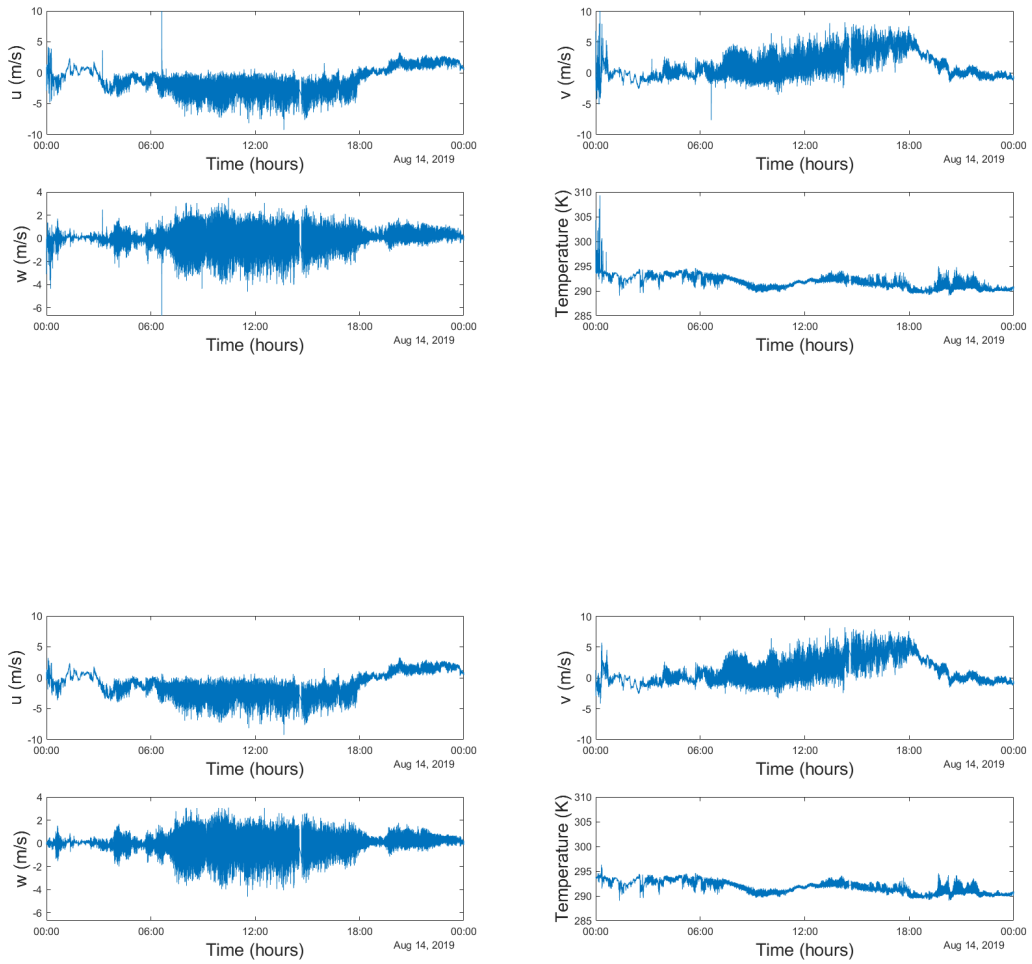

Figure 4.9. From top to bottom time signals of the velocity components and temperature with and without outliers respectively, both for August 14, 2019.

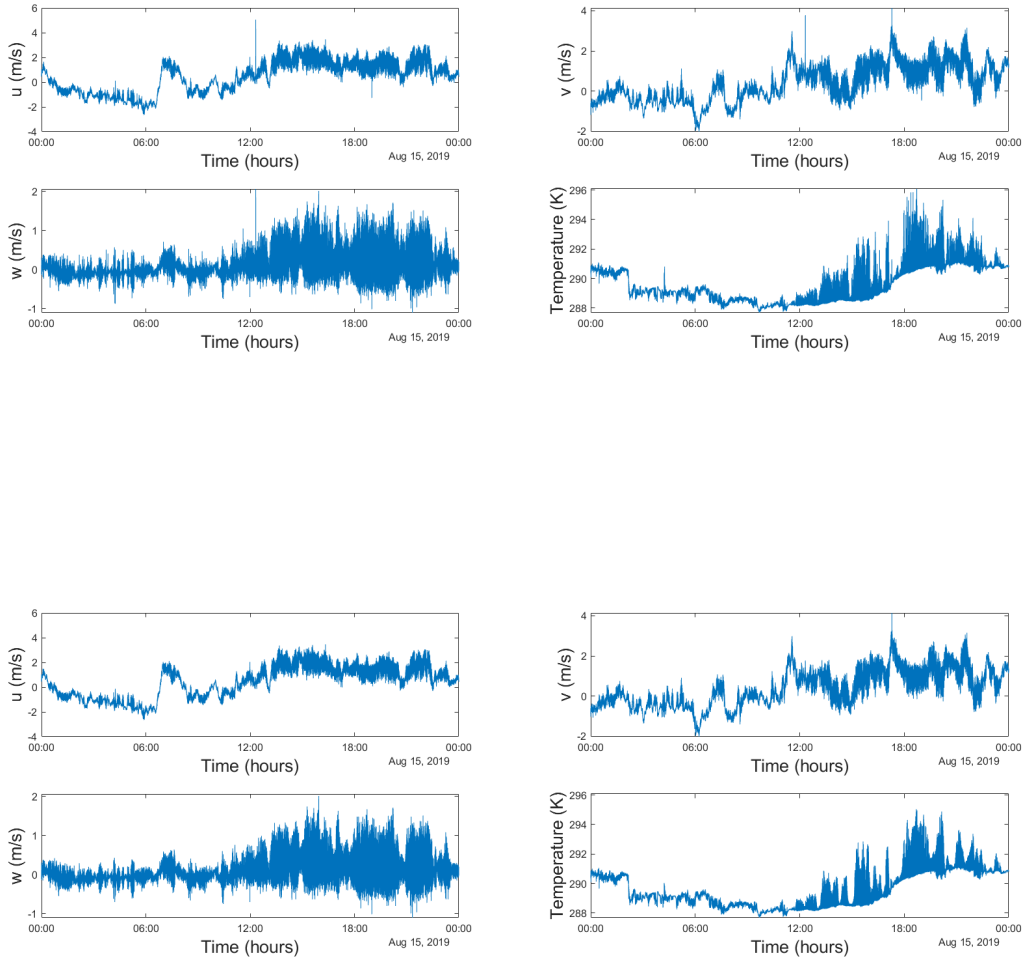

Figure 4.10. From top to bottom time signals of the velocity components and temperature with and without outliers respectively, both for August 15, 2019.

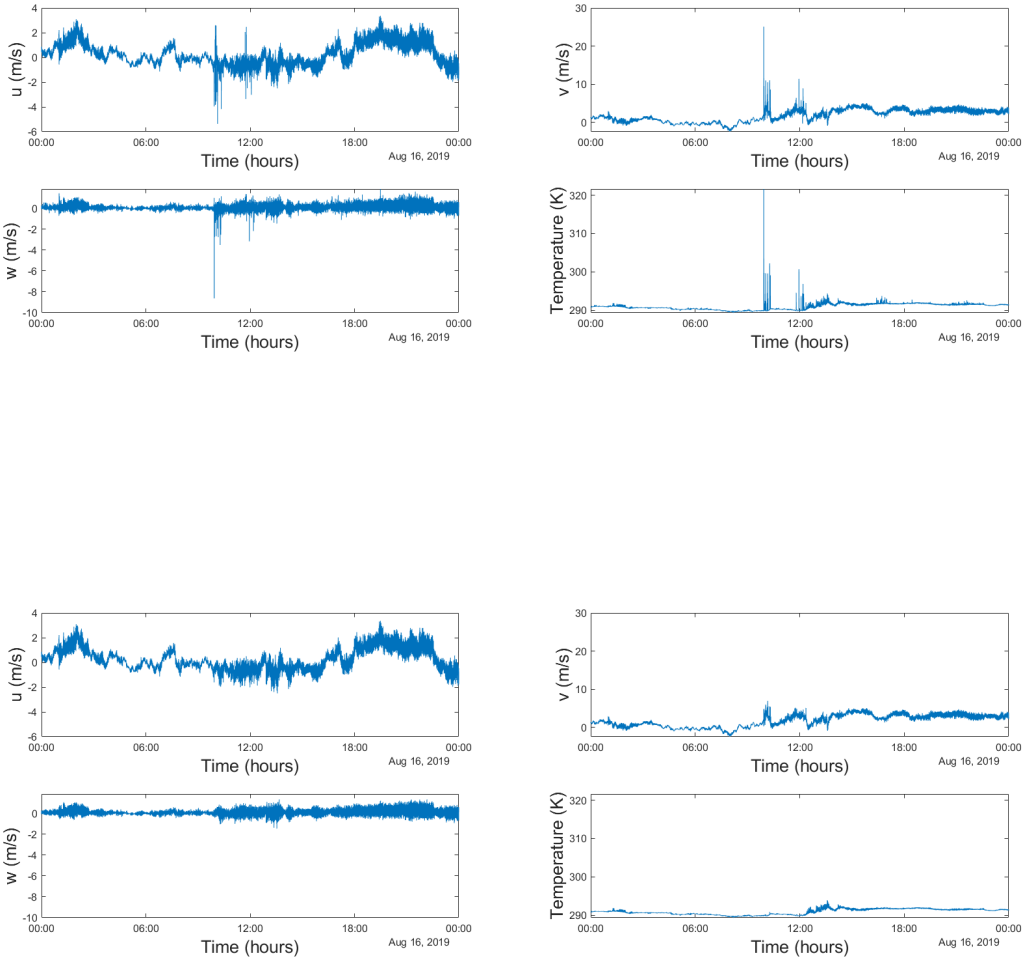

Figure 4.11. From top to bottom time signals of the velocity components and temperature with and without outliers respectively, both for August 16, 2019.

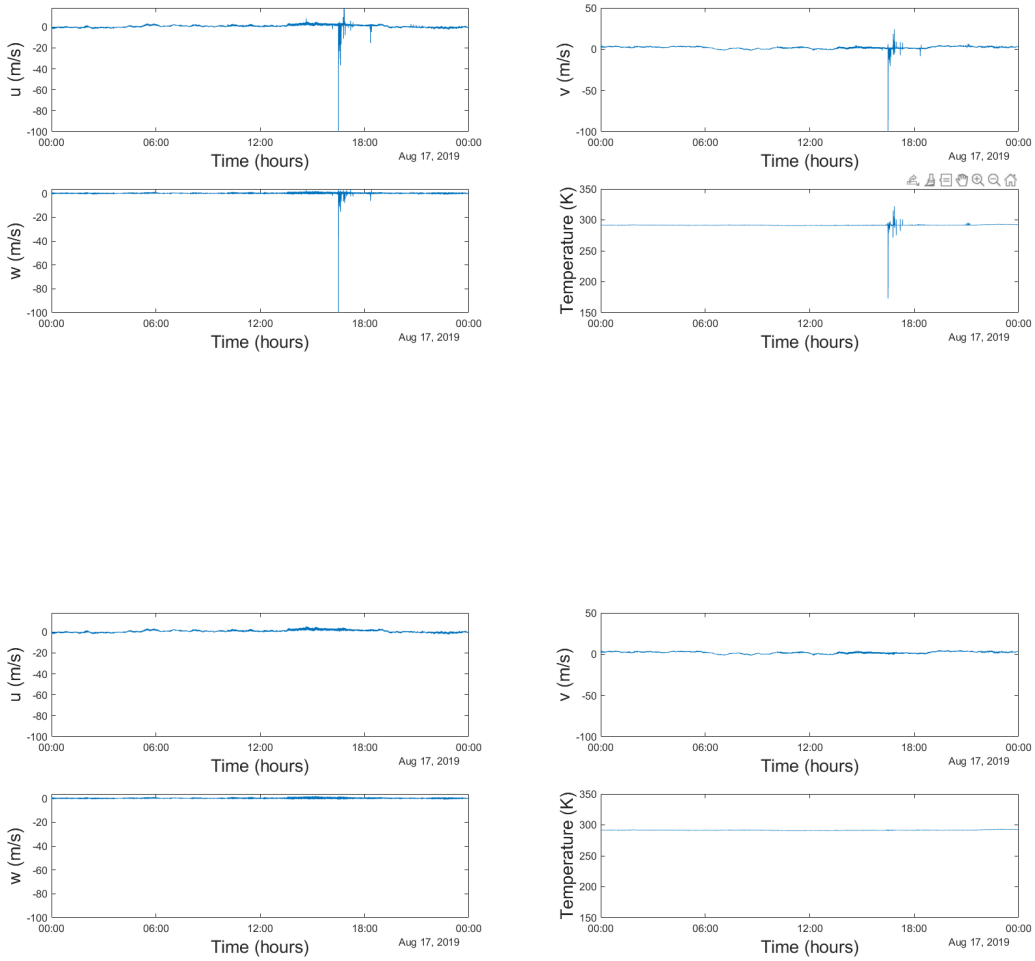

Figure 4.12. From top to bottom time signals of the velocity components and temperature with and without outliers respectively, both for August 17, 2019.

Figure 4.13. From top to bottom time signals of the velocity components and temperature with and without outliers respectively, both for August 18, 2019.

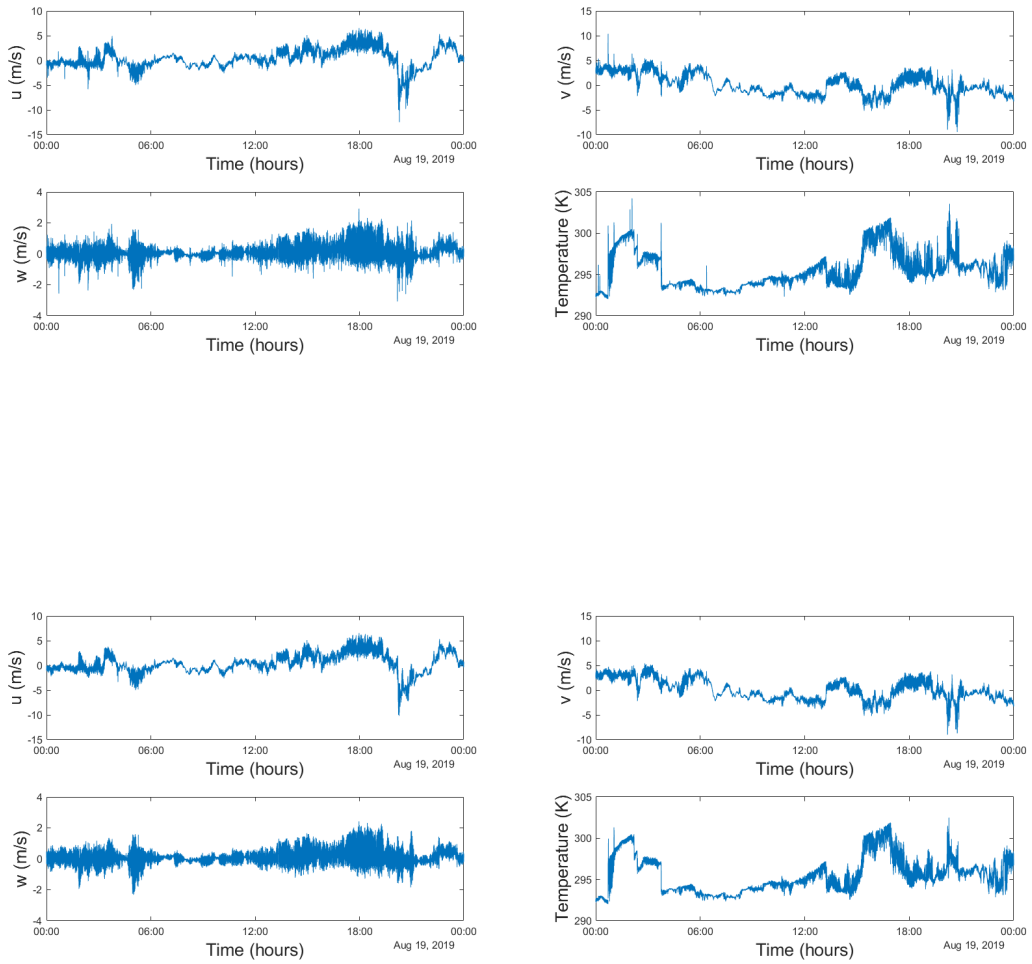

Figure 4.14. From top to bottom time signals of the velocity components and temperature with and without outliers respectively, both for August 19, 2019.

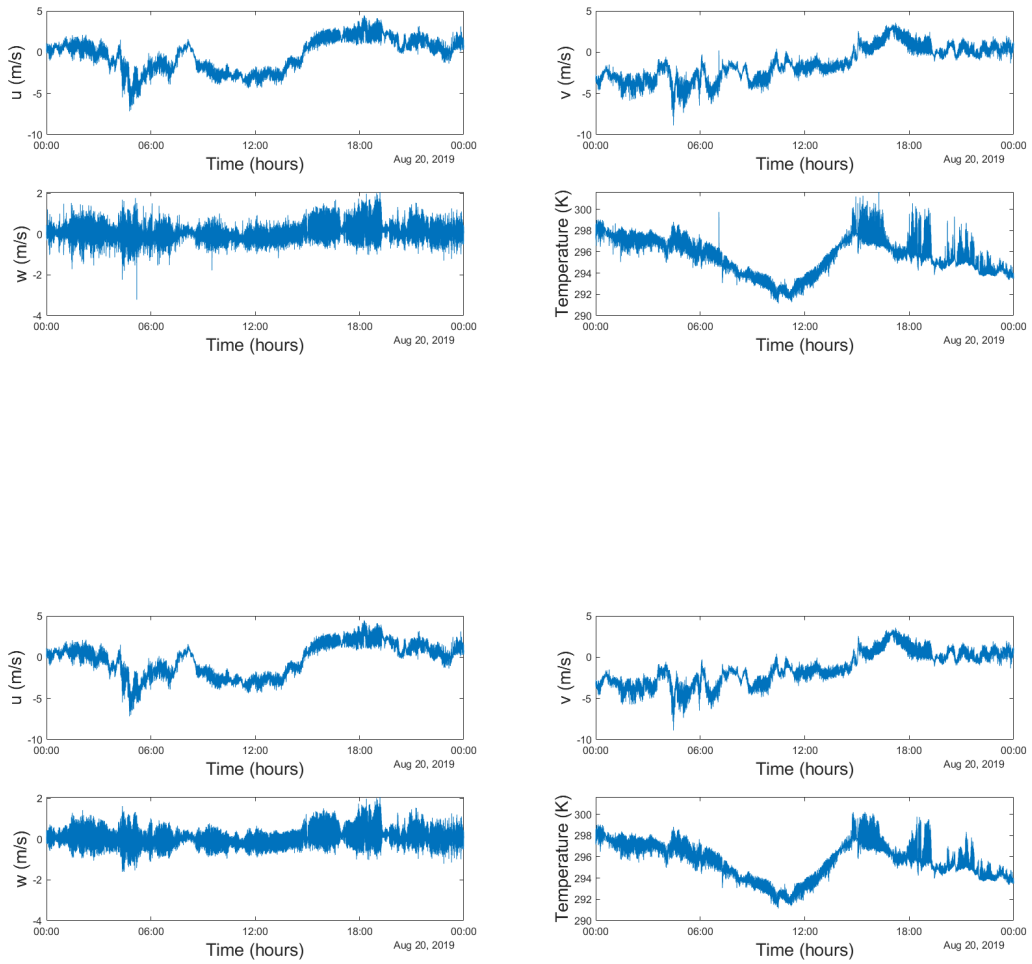

Figure 4.15. From top to bottom time signals of the velocity components and temperature with and without outliers respectively, both for August 20, 2019.

Also, a rough estimate of uncertainties is quantified in table 4.2:

Table 4.2. Outliers removed from the data per day of the week of data analyzed.

Date	Outliers Removed from Data
August 14, 2019	0.58%
August 15, 2019	1.46%
August 16, 2019	0.60%
August 17, 2019	0.45%
August 18, 2019	0.69%
August 19, 2019	0.55%
August 20, 2019	0.73%

As it can be seen in these figures and especially for August 16 and 17 of 2019, the outliers change the overall picture of these plots and prevent observation of trends in the data. For parameters such as Reynolds stresses, friction velocities, among other variables which are calculated from u, v, w and T, the influence of the outliers are compounded as shown in plots 4.9 - 4.15. Results from table 4.1 also confirm a high number of outliers that are present in the data, being August 15, 2019, the day of data analyzed with the highest number of outliers, representing 1.43% of the data for this day.

Consequently, it was then considered that the best approach for the rest of the analysis was to use the data with the outliers removed from it.

4.4 Time Signals of the Velocity Components and Temperature

The dominant components of the wind velocity vector are u and v, with w values close to 0. This shows that the mean velocity is in the horizontal plane.

The magnitudes of u, v and w are greater for August 14, 2019 and August 19, 2019 compared to the rest of analyzed days. The maximum u, v and w were 9.22 , 8.24 and 4.62 m/s respectively for August 14, 2019 and 10.18, 9 and 2.42 m/s respectively for August 19, 2019. For days such as August 15, 2019 the maximum u, v and w were 3.46, 4.14 and 2.01 m/s respectively. Specifically, for August 14, 2019, we can see high variability in the middle of the day whereas for days such as August 15, 16, 18 and 19, 2019 the higher variability is found towards later in the day. For most of the analyzed days of data, temperature increases for the second half of the day, and either

decreases or is roughly constant during the first half of the day. For August 17, 2019, v follows T oddly well.

The plots for u, v, w and T, with outliers removed shown in the previous section are shown in this section but with a different y-axis scale. This scale is the same for u, v and w for each day analyzed. T is the same scale as shown before. Since the velocity components magnitudes and temperature are different between the days, the scales used in the plots are different between different days.

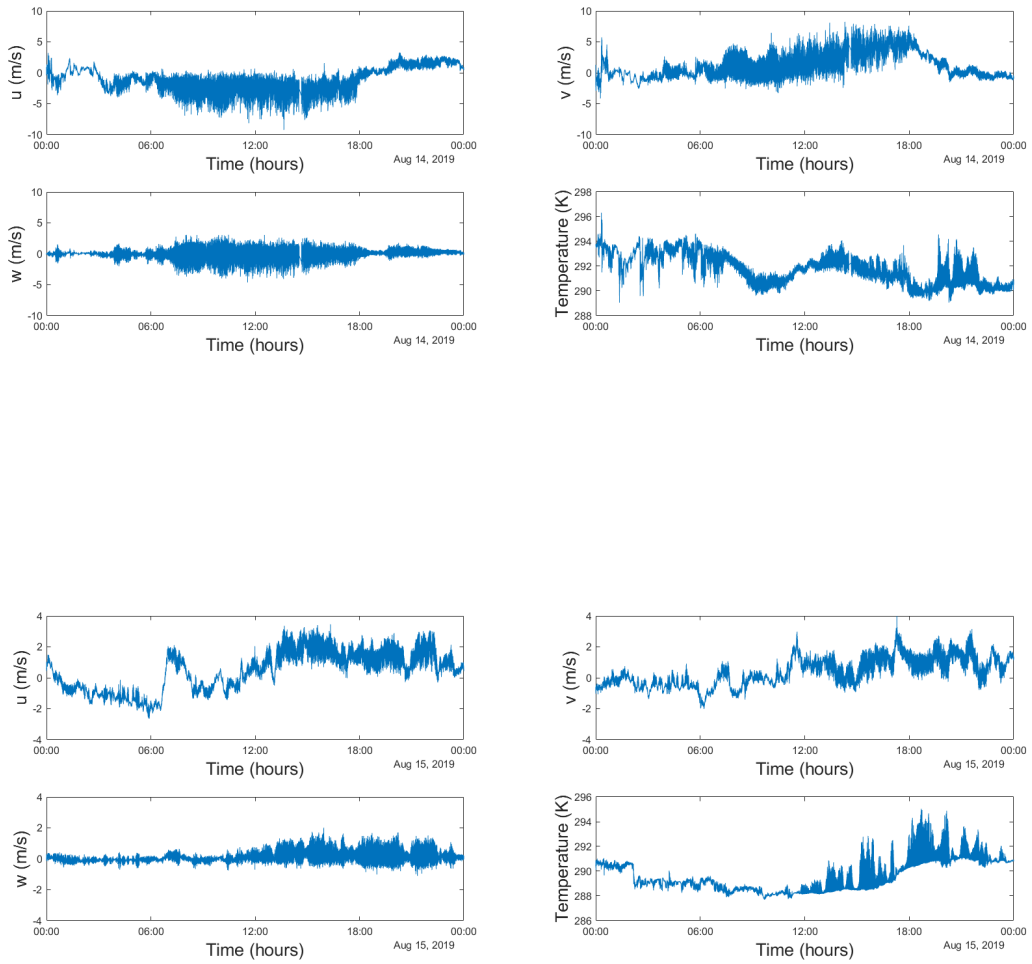

Figure 4.16. From Top to Bottom Time Signals of the Velocity Components and Temperature for August 14, 2019 and August 15, 2019, respectively.

Figure 4.17. From Top to Bottom Time Signals of the Velocity Components and Temperature for August 16, 2019 and August 17, 2019, respectively.

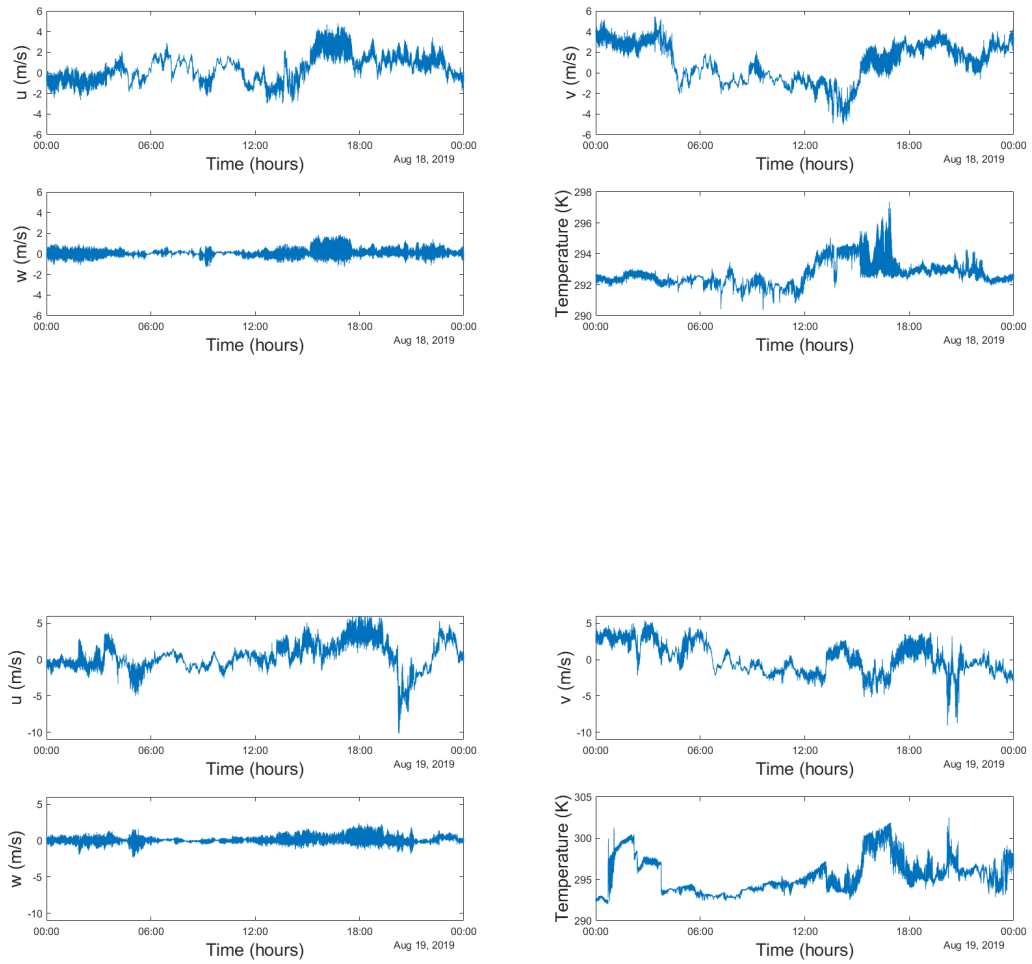

Figure 4.18. From Top to Bottom Time Signals of the Velocity Components and Temperature for August 18, 2019 and August 19, 2019, respectively.

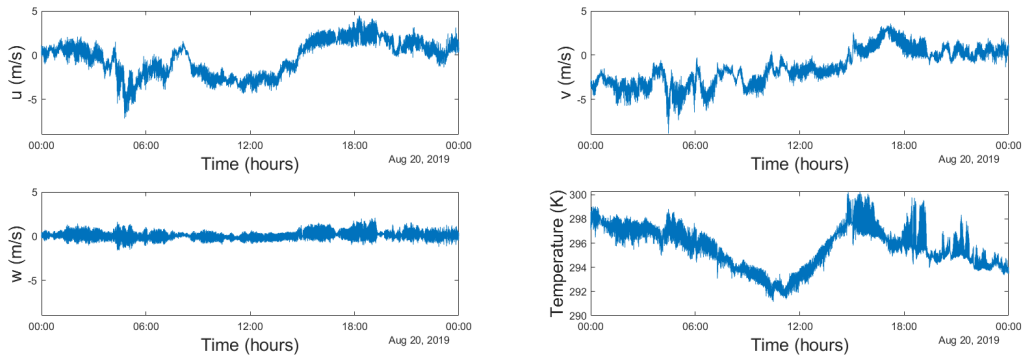

Figure 4.19. Time Signals of the Velocity Components and Temperature for August 20, 2019.

4.5 Fluctuating Velocities and Temperature

The fluctuating velocity and temperture are computed from Reynolds decomposition. For this study, the 10 minutes average of u, v, w and T, were used to calculate the mean components from which the fluctuations were computed for each 10 minutes time frame. The fluctuating velocity and temperature for each 24 hour period are shown in figures 4.20 to 4.23. For u', v', w' and T', there is a clear pattern of the magnitude of these variables being greater in the second half of the day. The figures show a clear correlation between the three components of velocity and temperature.

The magnitudes of u', v' and w' are greater for August 14, 2019 and August 19, 2019 than for the rest of analyzed days. The maximum u', v' and w' were 5.57, 5.79 and 4.15 m/s respectively for August 14, 2019 and 7.62, 5.07 and 2.12 m/s respectively for August 19, 2019, when for days such as August 15, 2019 the maximum u', v' and w' were 1.70, 1.61 and 1.56 m/s respectively.

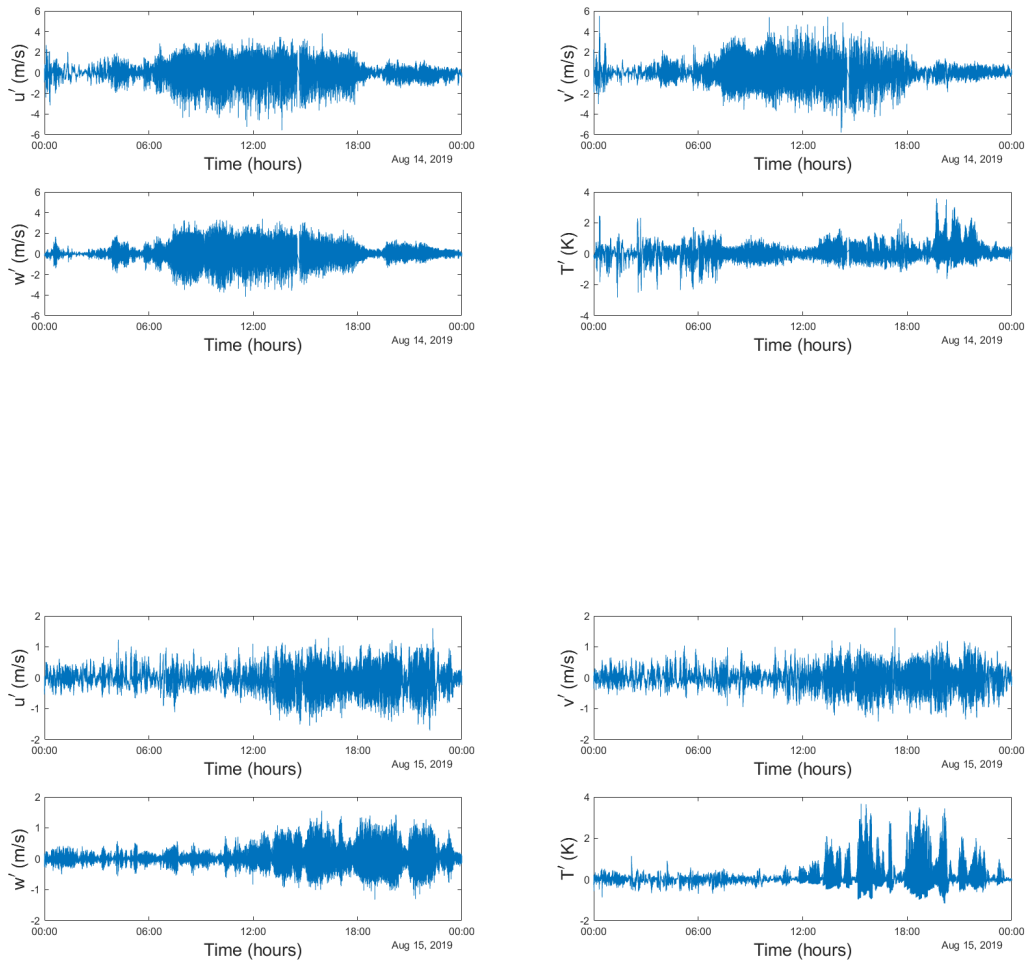

Figure 4.20. From Top to Bottom Fluctuating Velocities and Temperature for August 14, 2019 and August 15, 2019, respectively.

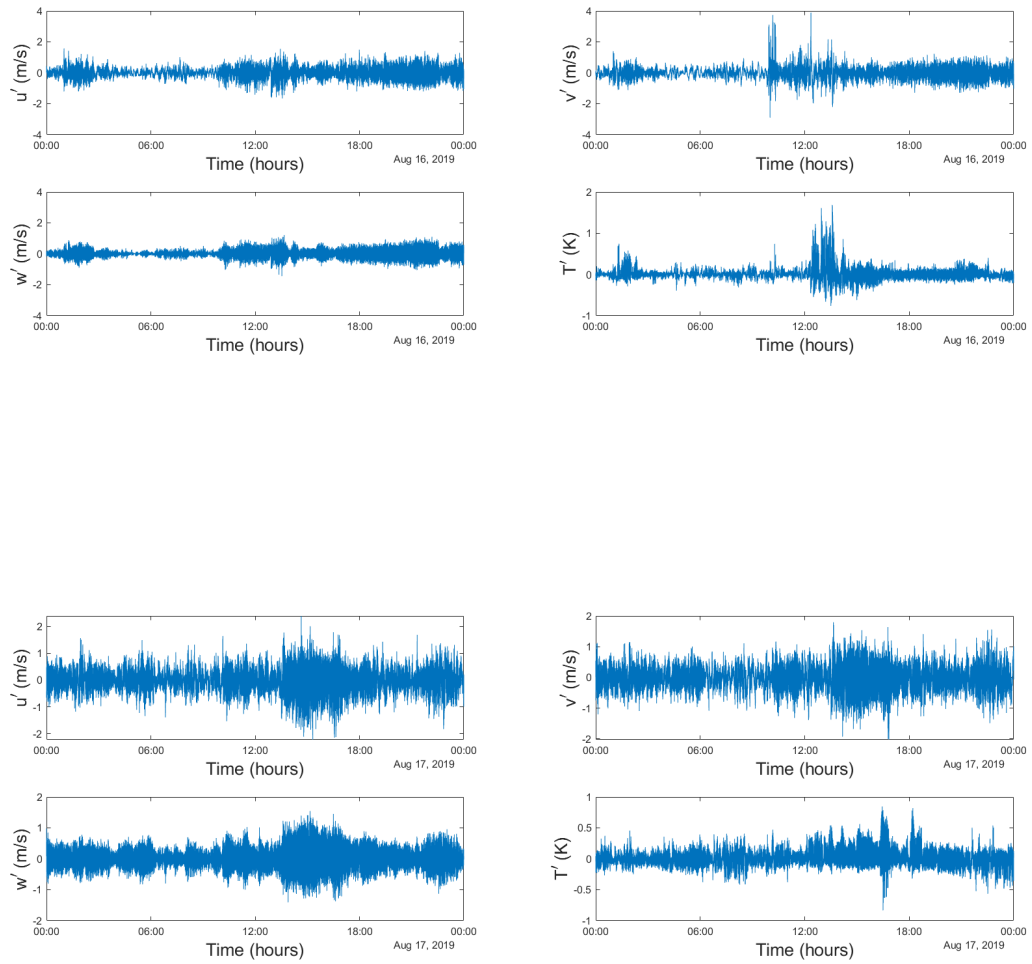

Figure 4.21. From Top to Bottom Fluctuating Velocities and Temperature for August 16, 2019 and August 17, 2019, respectively.

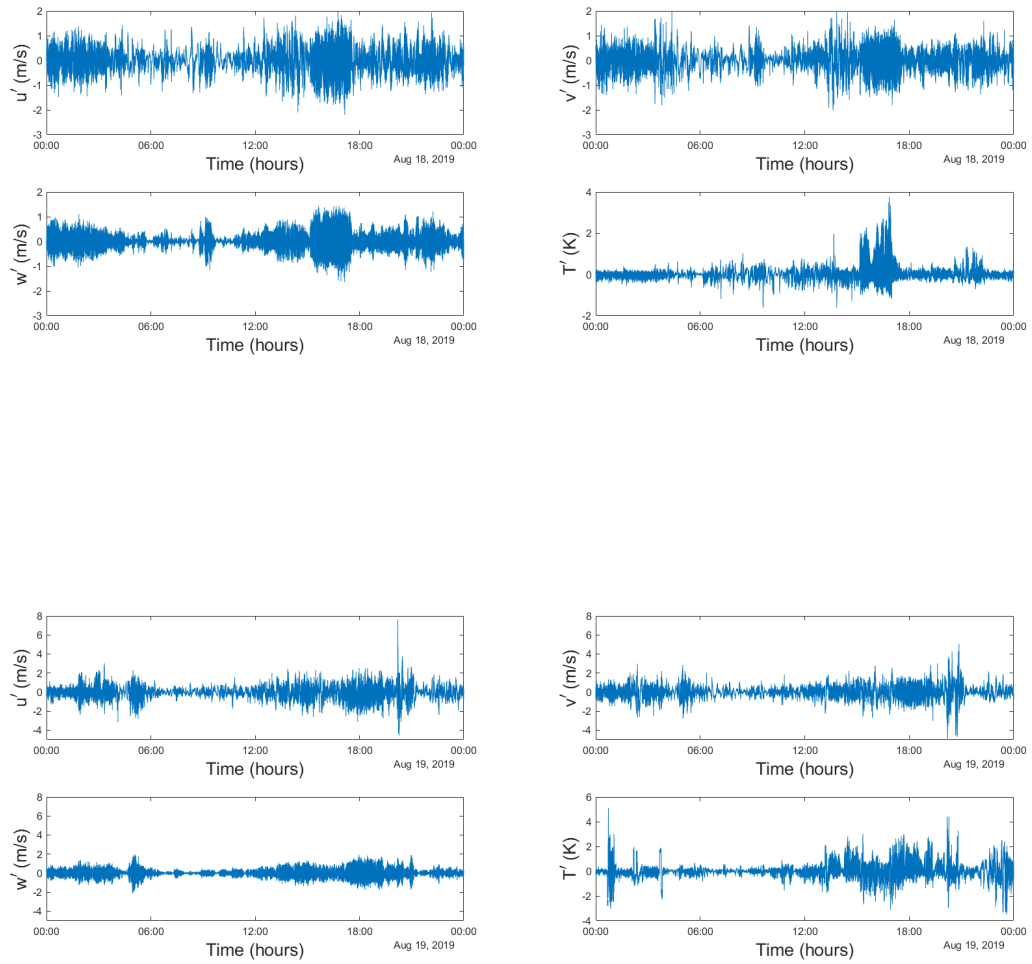

Figure 4.22. From Top to Bottom Fluctuating Velocities and Temperature for August 18, 2019 and August 19, 2019, respectively.

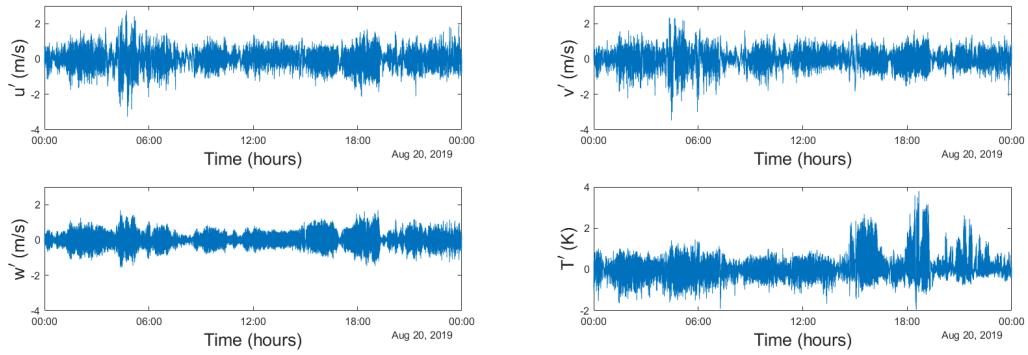

Figure 4.23. Fluctuating Velocities and Temperature for August 20, 2019.

4.6 Reynolds Stresses and Turbulent Heat Flux

To better understand the turbulence that occurs in the WBL, a thorough analysis of the Reynolds stresses and turbulent heat flux was performed. Moreover, it is informative to show how the different Reynolds stresses and turbulent heat flux profiles look when non-dimensionalized.

To calculate the non-dimensional profiles, the maximum wind velocity for each day analyzed was used to normalize the velocity. It was decided to use the maximum wind velocity instead of using the instantaneous wind speed velocity due to the fact that the later could be 0 or close to 0 in some parts of the day, resulting in incredibly big spikes in the variables when normalized.

It does not seem there is a dominant component of the Reynolds shear stress. The magnitudes of $u'w'$, $u'v'$ and $v'w'$ are similar for most of the days analyzed. Nevertheless, the values for $u'w'$, $u'v'$ and $v'w'$ for August 14, 2019 and August 19, 2019, are much greater than the rest of the days at any time of the day.

Comparing to historical wind velocities in Newington, NH for the days analyzed, that are presented in table 4.1, it can be seen that, for August 14, 2019 and August 19, 2019 the average

wind velocity is greater than the rest of the analyzed days (2.3 m/s and 2.5 m/s for August 14, 2019 and August 19, 2019 respectively). Historical wind velocities in Newington, NH, are consistent with the data obtained from the sonic anemometer except for August 17, 2019 where the historical average wind velocity in Newington, NH is greater than the average wind velocity obtained by the sonic anemometer.

For most of the days analyzed, the Reynolds stresses are greater for the second half of the day. This increase in the Reynolds stress in the second half of the day is likely related to the warming up of the ocean during the day. The turbulent heat flux, $w'T'$, is also nominally greater as well for the second half of the day for most of the days. Note that the sign of $w'T'$ is informative, where $w'T'$ + denotes hot (cold) fluid carried upward (downward). For the most part, the Reynolds shear stress is strongly correlated with the turbulent heat flux. For days such as August 14, 17 and 18, 2019, Reynolds shear stresses are greater in the middle of the day, while for August 15 and 19, 2019, these are greater in the second part of the day.

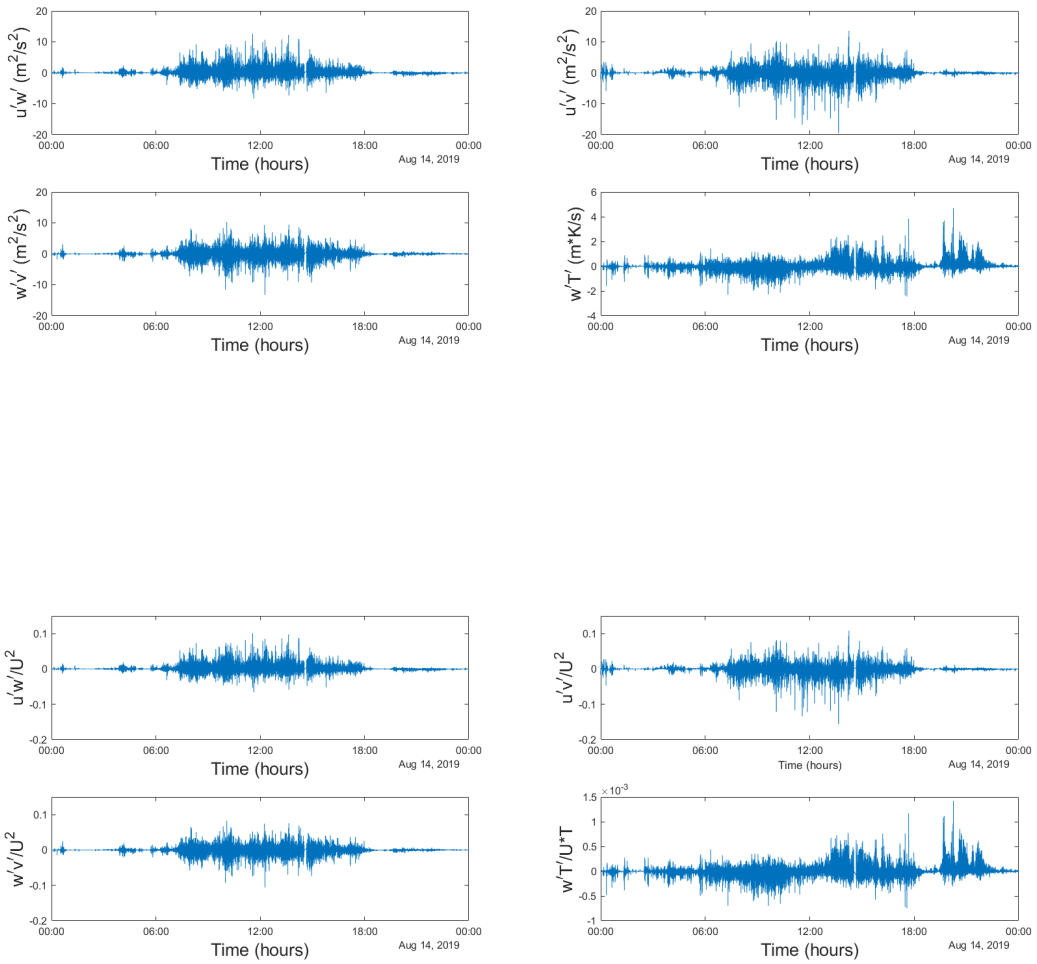

Figure 4.24. From Top to Bottom, Dimensional and Non Dimensional Reynolds Stresses and Turbulent Heat Flux for August 14, 2019.

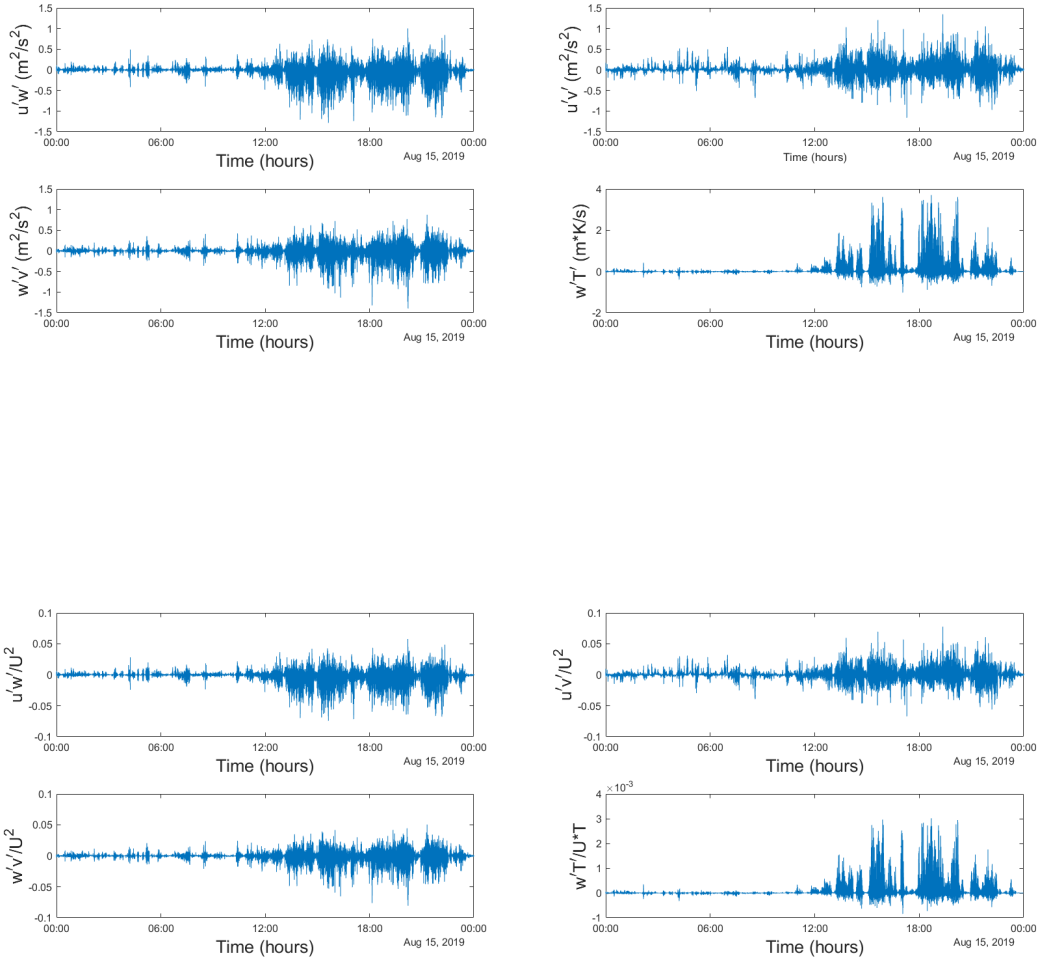

Figure 4.25. From Top to Bottom, Dimensional and Non Dimensional Reynolds Stresses and Turbulent Heat Flux for August 15, 2019.

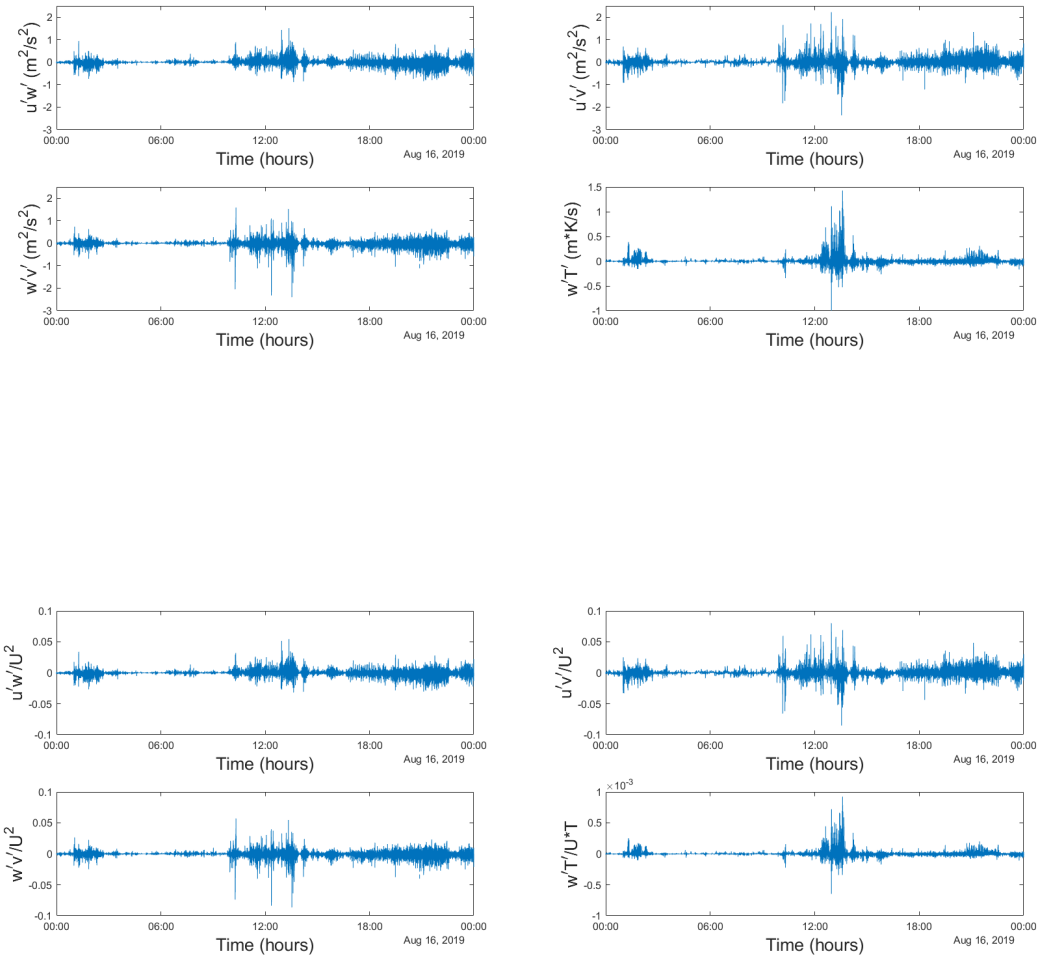

Figure 4.26. From Top to Bottom, Dimensional and Non Dimensional Reynolds Stresses and Turbulent Heat Flux for August 16, 2019.

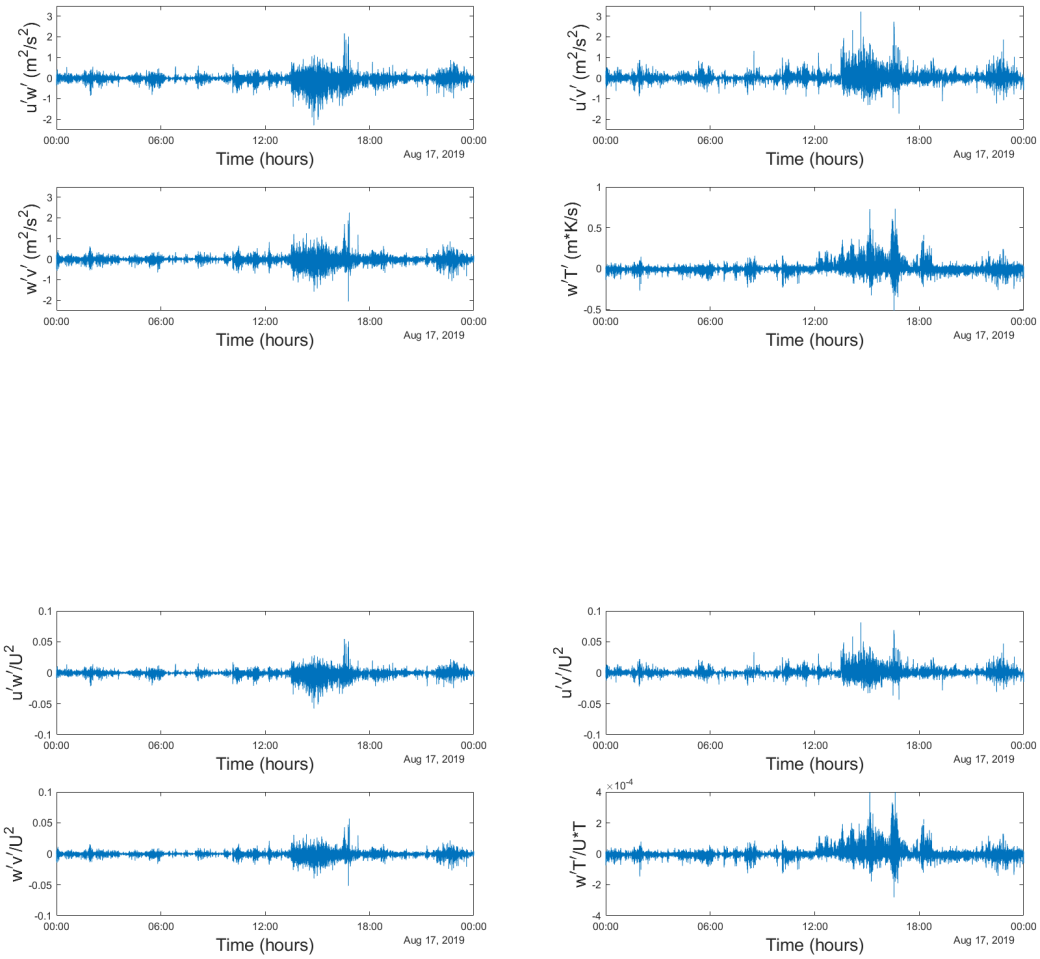

Figure 4.27. From Top to Bottom, Dimensional and Non Dimensional Reynolds Stresses and Turbulent Heat Flux for August 17, 2019.

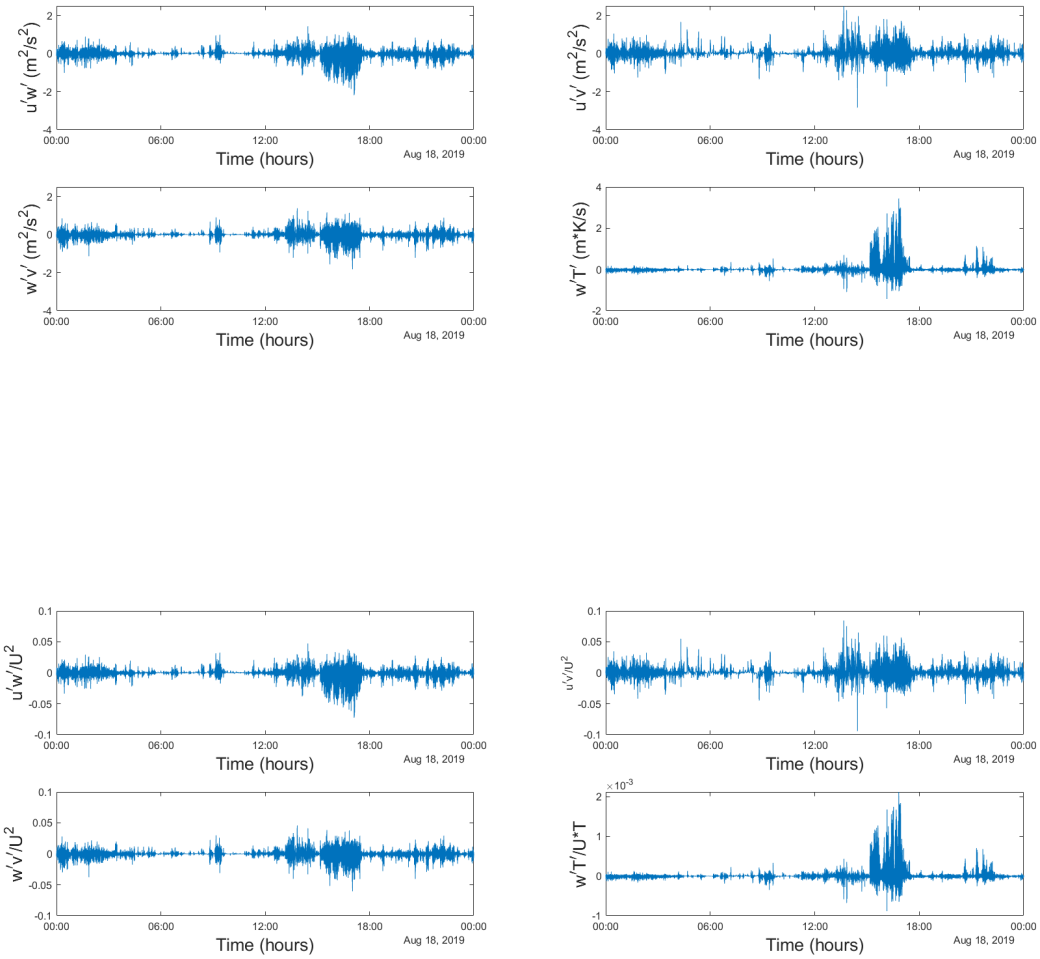

Figure 4.28. From Top to Bottom, Dimensional and Non Dimensional Reynolds Stresses and Turbulent Heat Flux for August 18, 2019.

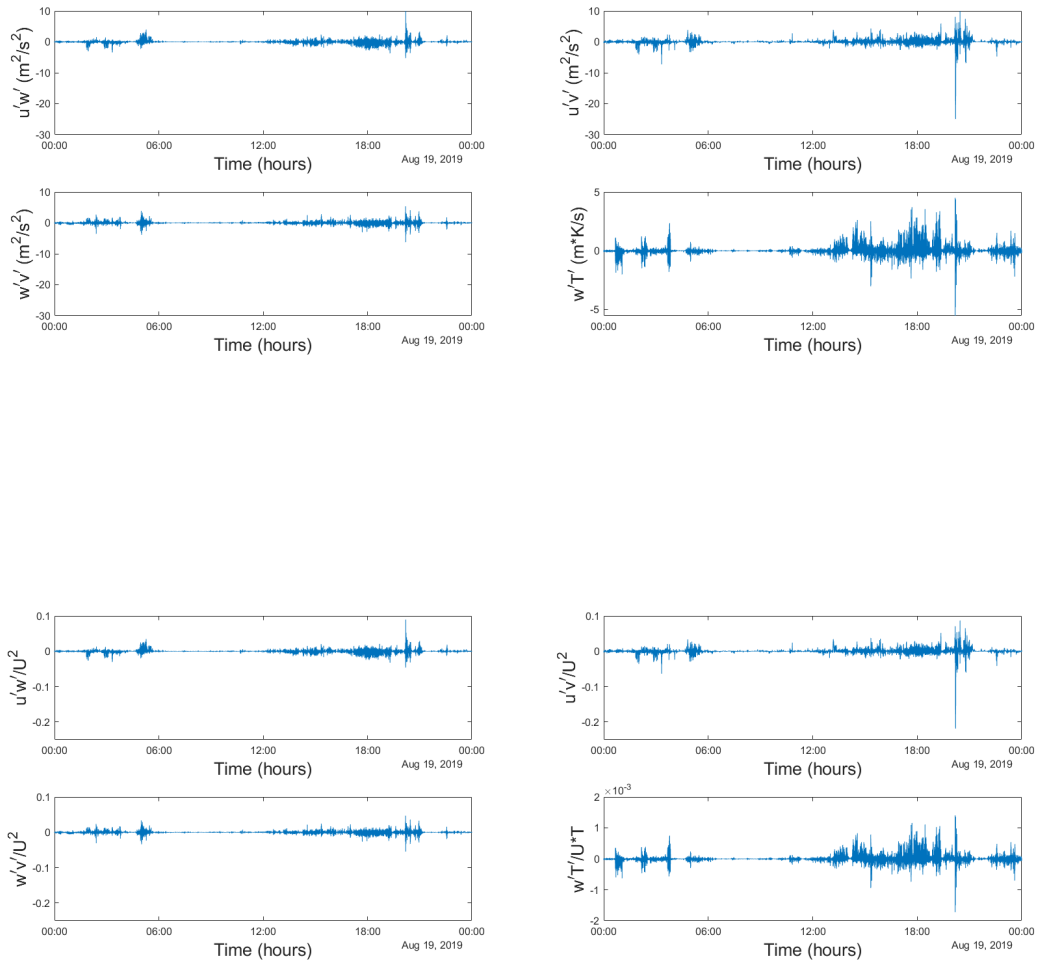

Figure 4.29. From Top to Bottom, Dimensional and Non Dimensional Reynolds Stresses and Turbulent Heat Flux for August 19, 2019.

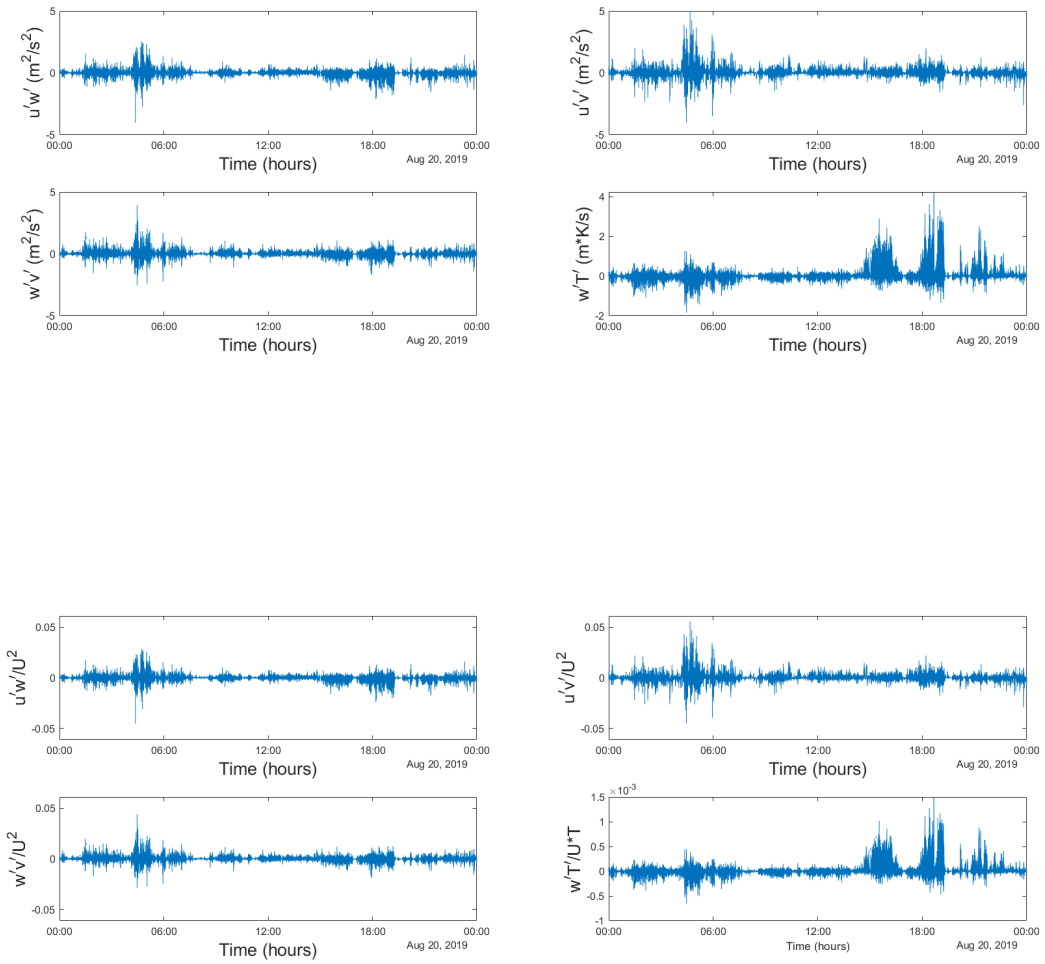

Figure 4.30. From Top to Bottom, Dimensional and Non Dimensional Reynolds Stresses and Turbulent Heat Flux for August 20, 2019.

4.7 Comparing Covariance Method, Tilt Corrected Covariance Method and Tensor Invariant Method for Calculating Friction Velocity

The so-called friction velocity is a parameter that characterizes the turbulence strength and viscous sub-layer thickness [15]. In this study, three different methods were used to calculate the friction

velocity for each of the days analyzed. The first was the eddy covariance method (CM) to calculate friction velocity. The following formula was used to calculate the friction velocity:

$$u^*_{cm} = ((\overline{u'w'}^2 + \overline{v'w'}^2)^{1/2})^{1/2}. \tag{4.1}$$

This u^*_{cm} may not be precise if the coordinate system of the sonic anemometer is tilted relative to the normal vector of the sea surface, since in practice, precise alignment of the sonic anemometer is not possible, tilt correction or other means of correcting for misalignment are after used.

For this reason, the second method for calculating friction velocity uses the eddy covariance method but adding tilt angle correction (TCCM). Equation 4.2 describes the friction velocity obtained using this method.

$$u^*_{tccm} = ((\overline{u'w'}^2|_{tc} + \overline{v'w'}^2|_{tc})^{1/2})^{1/2}. \tag{4.2}$$

The tilt angle correction is performed using the planar fit method [4]. This method consists in performing a two-dimensional linear regression of the vertical velocity component versus the horizontal velocity components. Wind data from different directions is required to use this method and that is why this method can only be used with data collected over long periods, during which the anemometer position remains the same or whose movements are known [16].

The last method for calculating the friction velocity is the Reynolds stress tensor invariant method (TIM). As its name implies, it uses the invariants of the Reynolds stress tensor to calculate the friction velocity, eliminating the need for tilt corrections [5]. The invariants of the Reynolds stress tensor are defined below:

$$\overline{u'_i u'_j} = \begin{bmatrix} \overline{u'u'} & \overline{u'v'} & \overline{u'w'} \\ \overline{u'v'} & \overline{v'v'} & \overline{v'w'} \\ \overline{u'w'} & \overline{v'w'} & \overline{w'w'} \end{bmatrix} \Longrightarrow \begin{bmatrix} \lambda_S & 0 & 0 \\ 0 & \lambda_M & 0 \\ 0 & 0 & \lambda_B \end{bmatrix}$$

The angle that forms the wind velocity vector with the plane determined by the largest and the intermediate eigenvectors is termed β. A graphical representation of β is shown in figure 4.31.

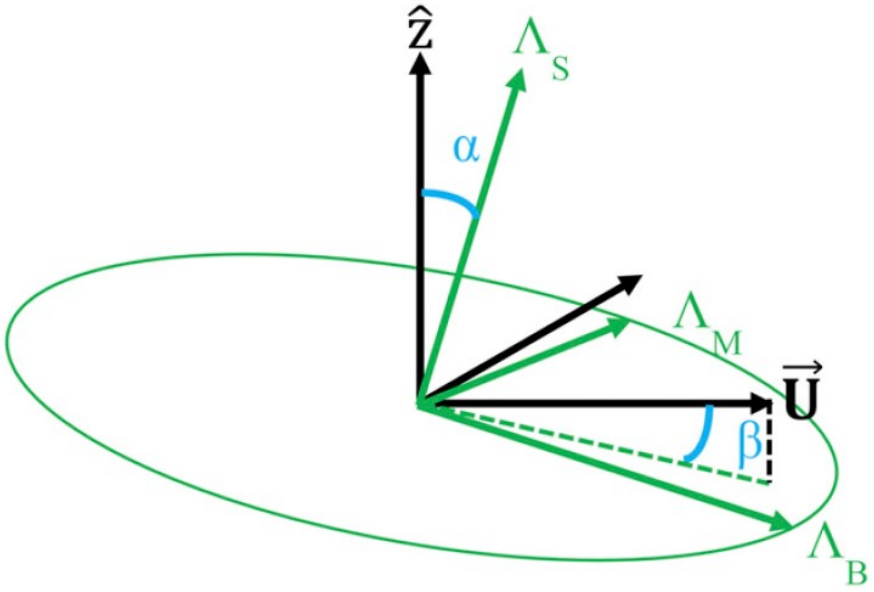

Figure 4.31. In this figure, the coordinate axes and the eigenvectors of the Reynolds stress tensor are represented. Angle α is defined as the angle between the smallest eigenvector with the vertical coordinate z. Angle β is defined as the angle that forms the wind velocity vector with the plane determined by the largest and the intermediate eigenvectors [5].

The process for calculating β is as follows:

(1) The plane determined by the largest and the intermediate eigenvectors are defined by calculating the cross product between Λ_B and Λ_M. Thus, the normal to this plane is calculated:

$$\overrightarrow{n_{\Lambda_B\Lambda_M}} = ||\Lambda_B\Lambda_M|| = ||\Lambda_B|| * ||\Lambda_M|| * sin(\Lambda_B\Lambda_M). \tag{4.3}$$

(2) Once this plane is defined, β is calculated in radians:

$$\beta = sin^{-1}\Big(\frac{|\overrightarrow{n_{\Lambda_B\Lambda_M}}\cdot U|}{(\sqrt{{n_{\Lambda_B\Lambda_M}}_i^2+{n_{\Lambda_B\Lambda_M}}_j^2+{n_{\Lambda_B\Lambda_M}}_k^2})*(\sqrt{u^2+v^2+w^2})}\Big). \tag{4.4}$$

(3) Once β and the eigenvalues are calculated, the friction velocity is determined from:

$${u^*_{tim}}^2 = -(\lambda_S - \lambda_B)sin\beta cos\beta. \tag{4.5}$$

Figures 4.32 to 4.35 shows the friction velocity calculated for each of the three methods for each day from August 14-20, 2019.

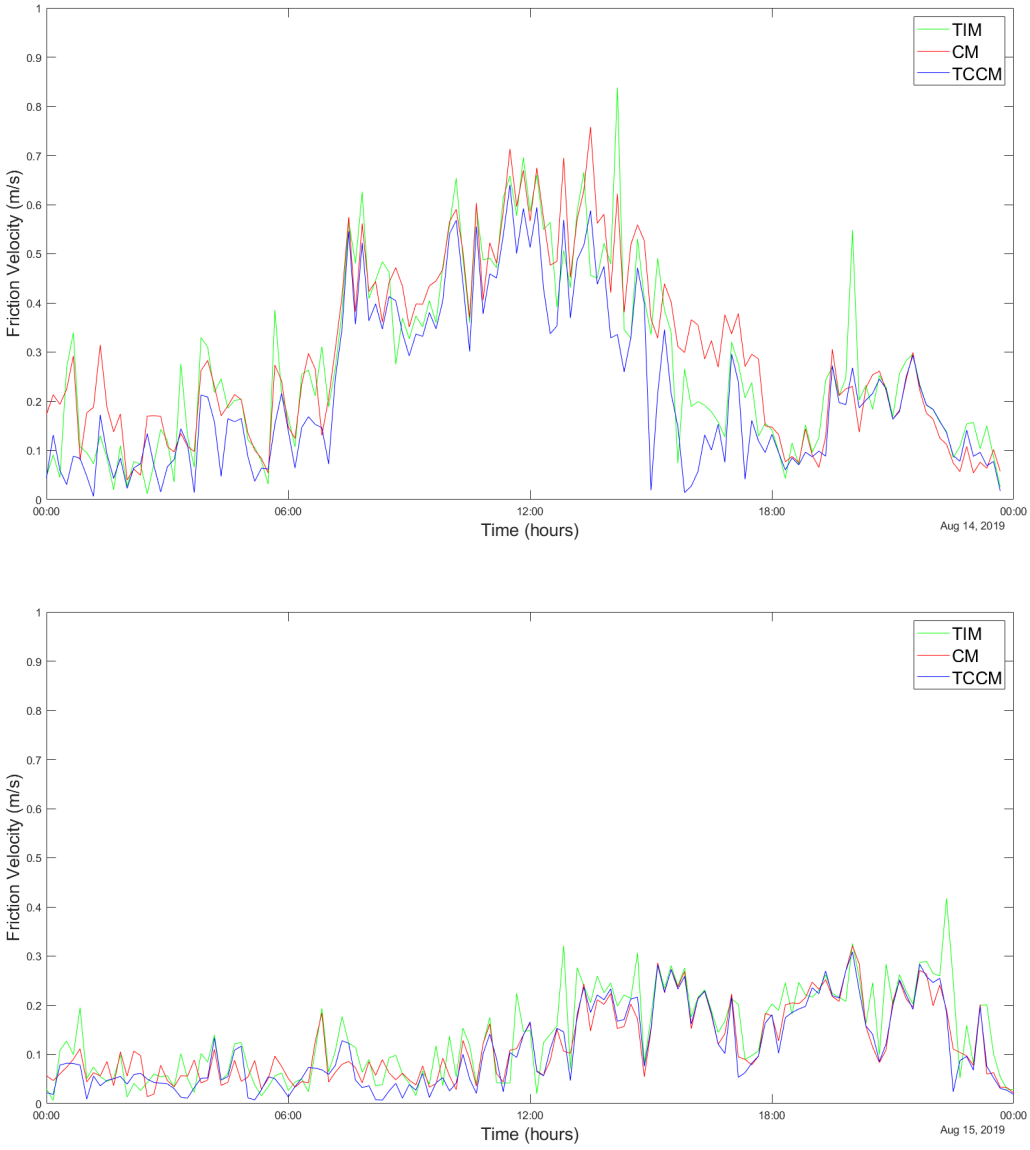

Figure 4.32. From Top to Bottom Friction Velocity for August 14, 2019 and August 15, 2019, respectively. In green is represented the friction velocity obtained following the TIM; in red is represented the friction velocity obtained using the CM; and in blue is represented the friction velocity obtained using the TCCM.

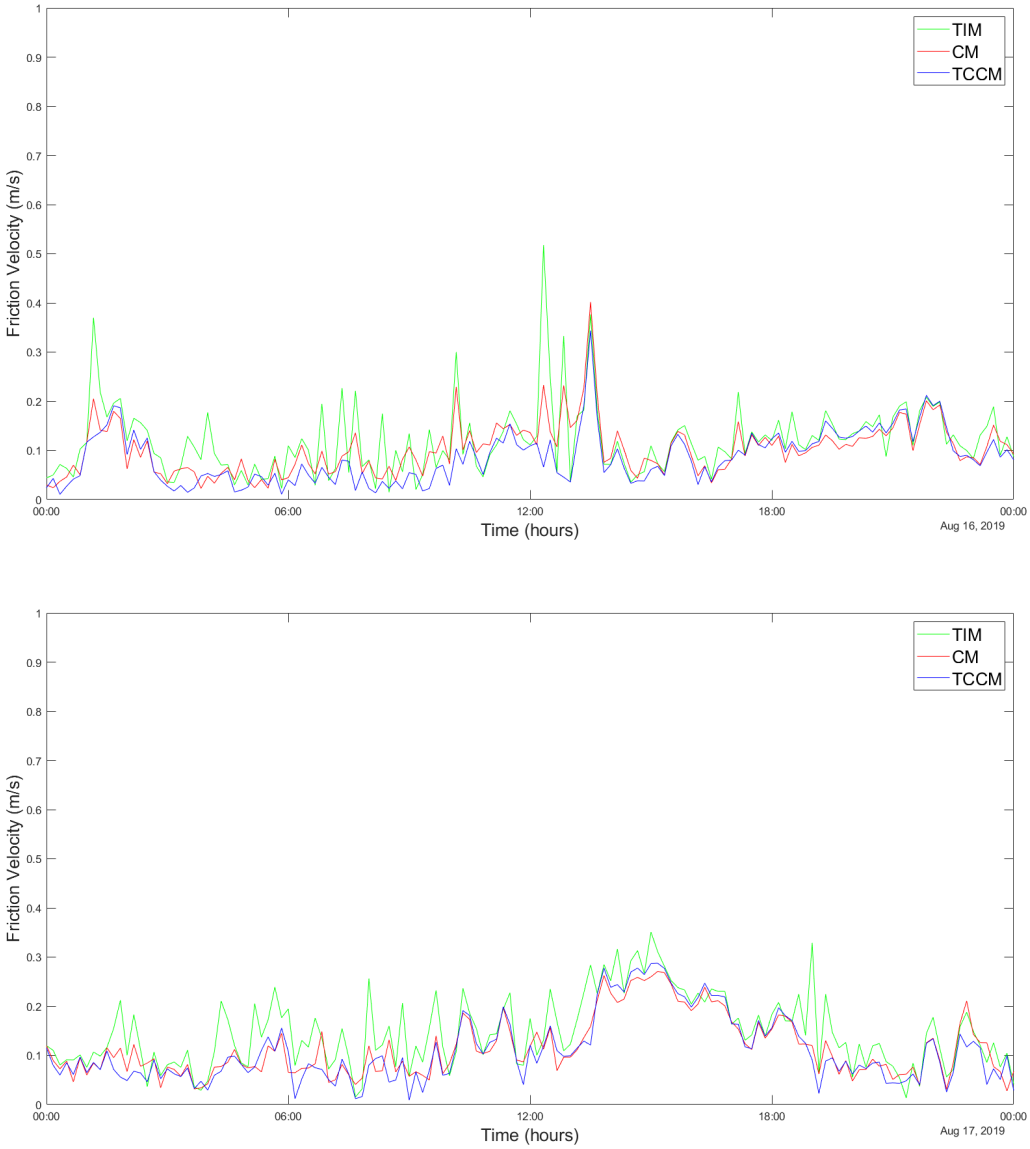

Figure 4.33. From Top to Bottom Friction Velocity for August 16, 2019 and August 17, 2019, respectively. In green is represented the friction velocity obtained following the TIM; in red is represented the friction velocity obtained using the CM; and in blue is represented the friction velocity obtained using the TCCM.

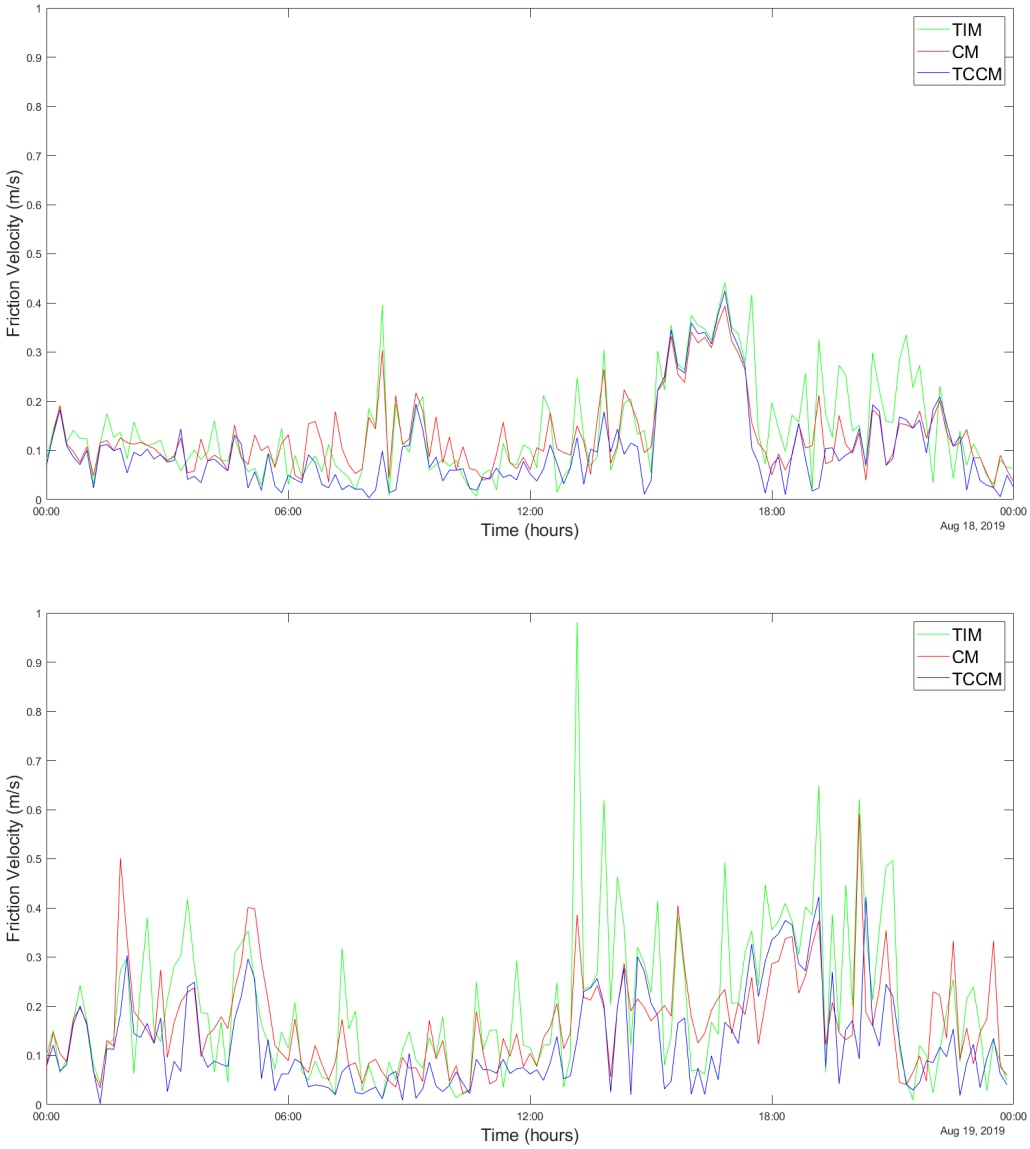

Figure 4.34. From Top to Bottom Friction Velocity for August 18, 2019 and August 19, 2019, respectively. In green is represented the friction velocity obtained following the TIM; in red is represented the friction velocity obtained using the CM; and in blue is represented the friction velocity obtained using the TCCM.

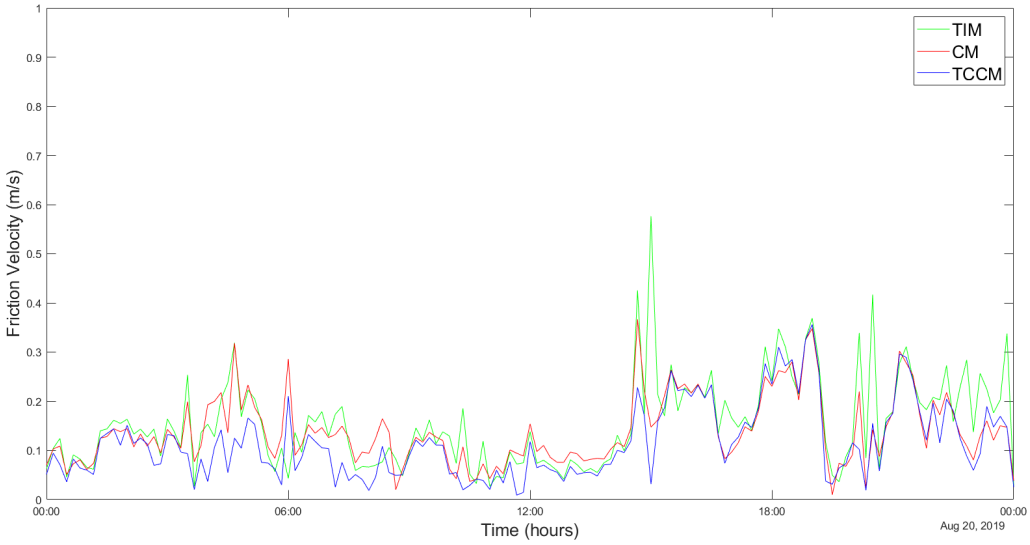

Figure 4.35. Friction Velocity for August 20, 2019. In green is represented the friction velocity obtained following the TIM; in red is represented the friction velocity obtained using the CM; and in blue is represented the friction velocity obtained using the TCCM.

The Mean Squared Error (MSE) was used to determine how similar these three methods are between them. Mean squared error quantifies the amount of error in statistical models. It assesses the average squared difference between different models that are comapred between each other. When two models are identical, the MSE equals zero. As two models are more different between each other, MSE value increases. The results from this analysis can be found in table 4.3:

Table 4.3. Comparison of the three methods for calculating friction velocity based on MSE criteria.

Date	TIM vs CM MSE	TIM vs TCCM MSE	CM vs TCCM MSE
August 14, 2019	0.0076	0.01	0.0113
August 15, 2019	0.0027	0.0029	8.4371e-04
August 16, 2019	0.0024	0.0047	0.0014
August 17, 2019	0.0027	0.0031	6.1898e-04
August 18, 2019	0.0036	0.0059	0.0030
August 19, 2019	0.0138	0.0185	0.0088
August 20, 2019	0.0041	0.0065	0.0021

Observations from the friction velocity plots and MSE analysis:

(i) The values for friction velocity obtained using the three methods are similar for most of the days. The TIM friction velocity values are generally greater than the friction velocity values obtained from the two other methods. The days with the largest differences between methods are August 16, 2019 and August 17, 2019. There is also high peak TIM friction velocity values obtained for days August 19 and 20, 2019, between 12-6 pm for both days.

(ii) Similar to fluctuating velocities, turbulence is greater in the second half of the day for all the three methods for most of the analyzed days. Yet, there are some exceptions, for instance: August 14, 17 and 18, 2019 seem to have high peak values of turbulence between 12-6 pm.

(iii) In table 4.3 seems clear that all these three methods for calculating friction velocity present similar results. MSE values go from 0.000844 to 0.0185, values that are almost 0, thus indicating the similar these three models are between them.

It was also considered interesting for this research to plot friction velocity vs horizontal wind velocity to compare our results to results described in the literature. For brevity, it was considered best to use the friction velocities from only one method. Thus, the friction velocity calculated following the Reynolds stress tensor invariant method was selected to be plotted versus the horizontal wind velocity. Results can be seen in figures 4.36 to 4.39:

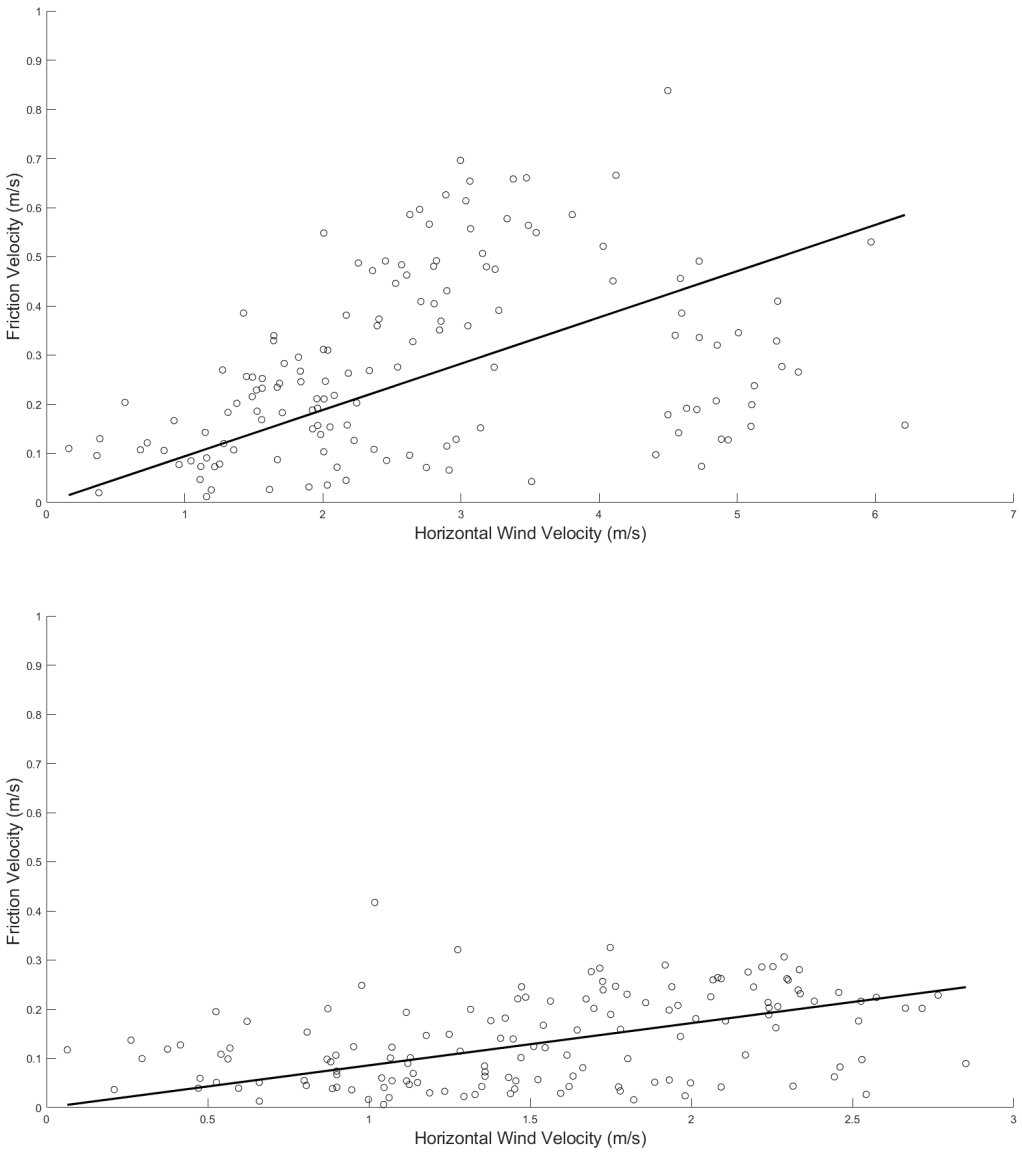

Figure 4.36. From top to bottom friction velocity versus horizontal wind velocity for August 14, 2019 and August 15, 2019, respectively.

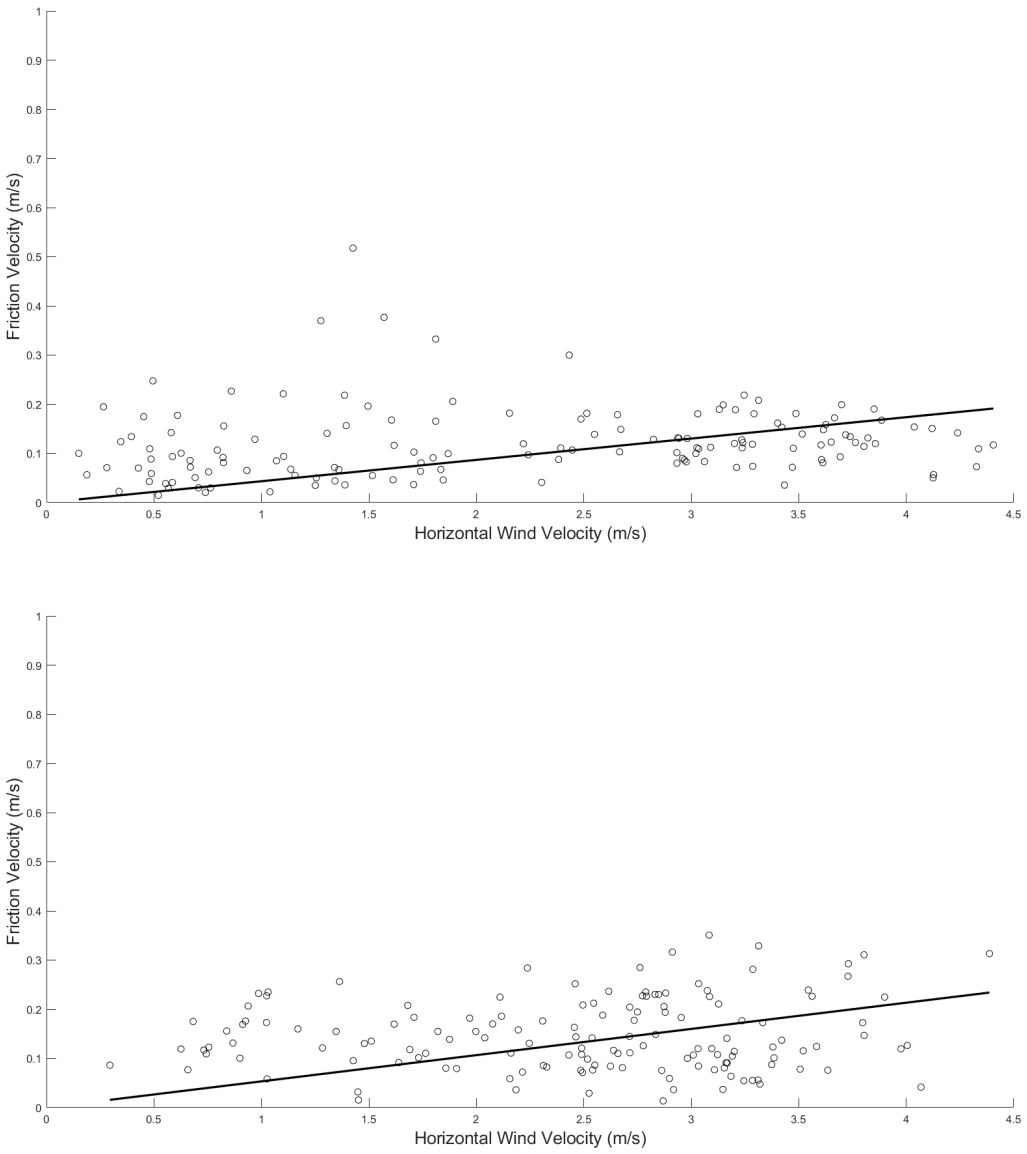

Figure 4.37. From top to bottom friction velocity versus horizontal wind velocity for August 16, 2019 and August 17, 2019, respectively.

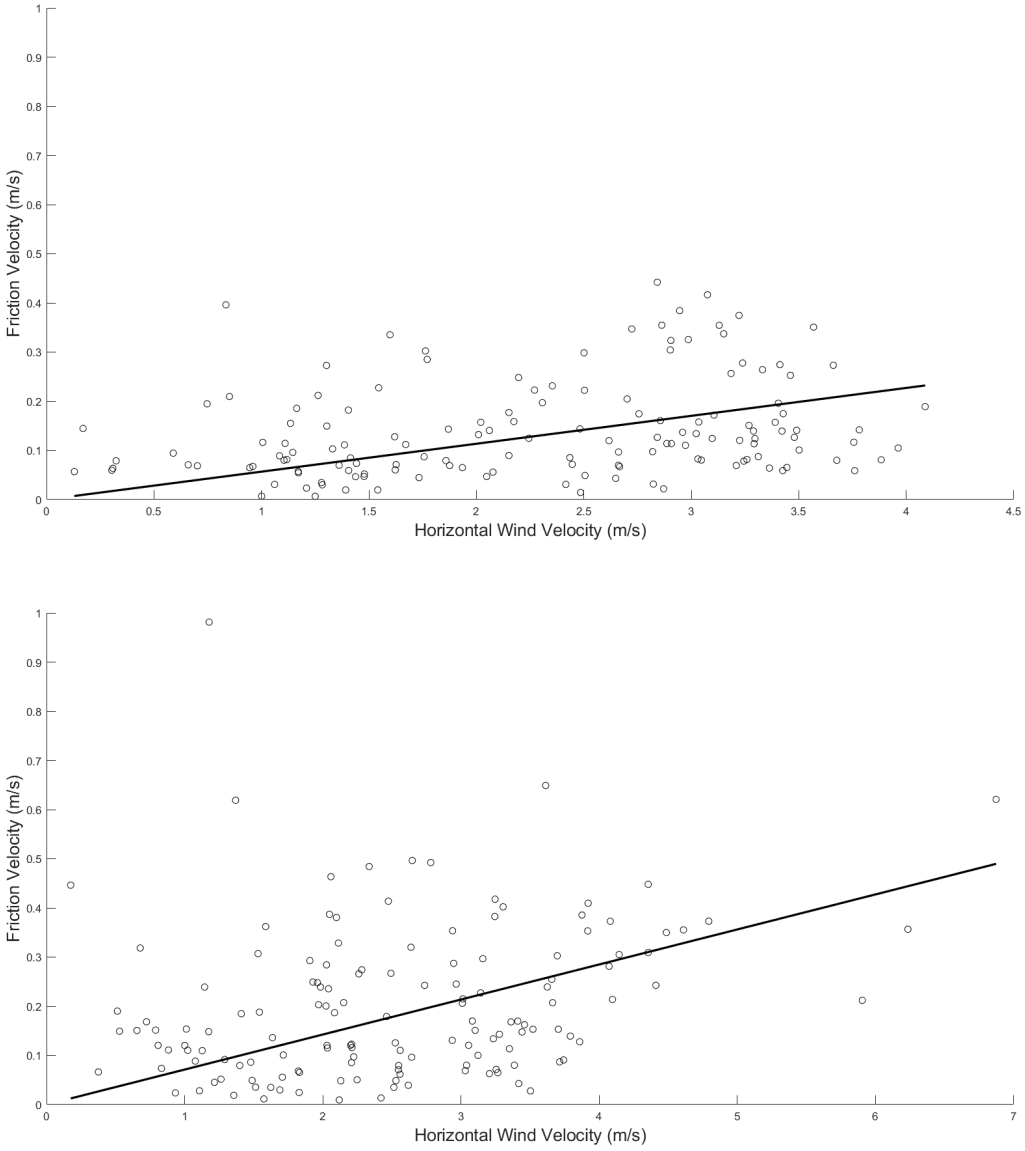

Figure 4.38. From top to bottom friction velocity versus horizontal wind velocity for August 18, 2019 and August 19, 2019, respectively.

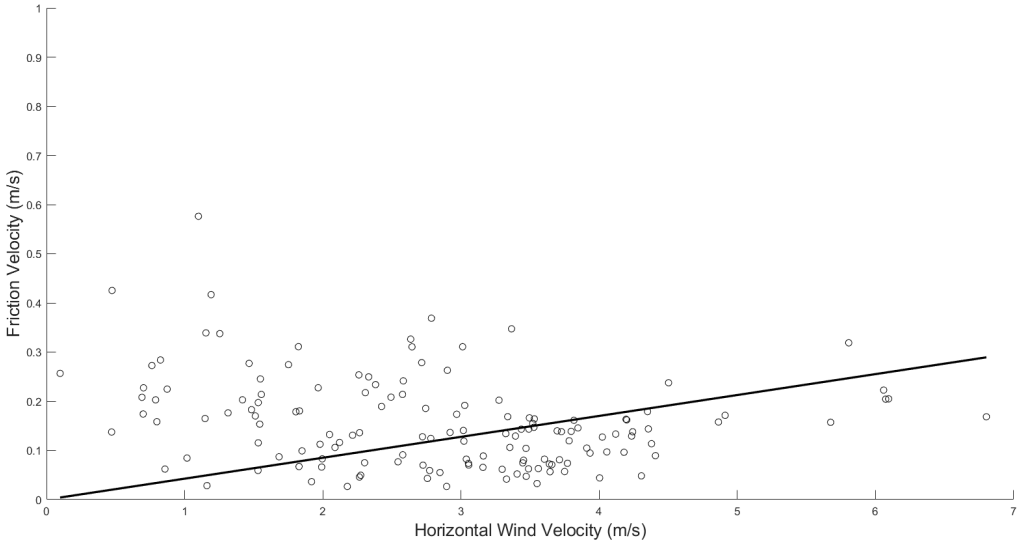

Figure 4.39. Friction velocity versus horizontal wind velocity for August 20, 2019.

Table 4.4. Fitted line slope per day of data analyzed.

Date	**Fitted Line Slope**
August 14, 2019	0.0942
August 15, 2019	0.0859
August 16, 2019	0.0434
August 17, 2019	0.0533
August 18, 2019	0.0568
August 19, 2019	0.0712
August 20, 2019	0.0425

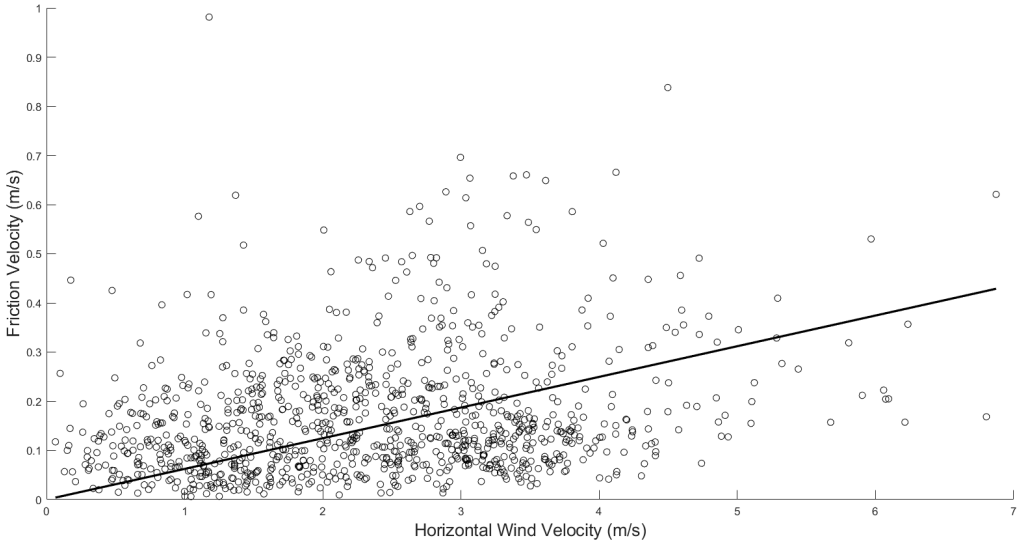

Figure 4.40. Friction velocity versus horizontal wind velocity for August 14-20, 2019.

It must be noted that the friction and horizontal wind velocity values were bin averaged for 10 minutes time frames. Moreover, a boundary condition was applied for friction velocity to be 0 when horizontal wind velocity is equal to 0.

To compare these results to values found in the literature for the relation between friction velocity and horizontal wind velocity, a paper named ”On the Exchange of Momentum over the Open Ocean” by James B. Edson, et al, was used.

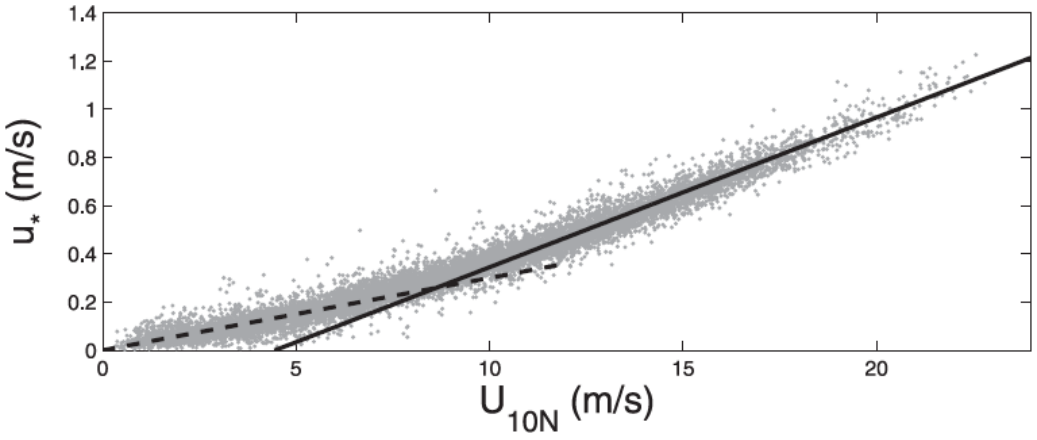

Figure 4.41. Individual estimates of friction velocity vs horizontal wind velocity [17].

In figure 4.41, it can be seen that at low U_{10N} the slope of this fitted line is 0.034, which is less steep than the slope of the fitted line representing the higher U_{10N} velocity, which has an slope of 0.045.

Figures 4.36 to 4.40 show that when the horizontal wind velocity increments the friction velocity increments as well. This is what it was achieved in this analysis and what the literature states. In table 4.4 it is shown the fitted line slope for each day of the week of data analyzed. These fitted lines seem to be more similar to the second phase fitted line from figure 4.41, especially for August 20, 2019 where the slope is almost exactly the same. Figure 4.40 shows friction velocity versus horizontal wind velocity for the entire week of data analyzed and the fitted line for this plot has a slope of 0.062.

4.8 Monin–Obukhov similarity theory

Application of the Monin–Obukhov similarity theory to determine the stability of the MABL and make further corrections in our model in future research is described here.

In the MABL three stability states exist: stable, neutral and unstable. Using Monin–Obukhov similarity theory, a dimensionless length known as Monin–Obukhov length is defined and used to classify the different stability states of the ABL.

Equation 4.6 provides the definition of the Monin–Obukhov length, where k is the von Karman constant equal to 0.41, g is the gravitational constant equal to 9.81 m^2/s, $\overline{w'T'}$ is the wall heat flux, $\overline{T_s}$ the mean sonic temperature and u_* the turbulent friction velocity [7].

$$\frac{1}{\zeta} = \frac{-\kappa g}{\overline{T_s}} \frac{\overline{w'T'}}{u_*^3} \tag{4.6}$$

As stated in Chapter 1, $0 \leq \zeta < 1000$ means that the ABL is stable, $|\zeta| \geq 1000$ corresponds to neutral conditions and $-1000 < \zeta < 0$ refers to unstable conditions [8].

In this section, it will also be investigated how the TIM for calculating friction velocity compares to the TCCM for different stability states. In order to analyze this matter, plots for friction velocity calculated using the TIM vs the TCCM accounting for MABL stability conditions were created. Please note that CM was not considered for this analysis as it was determined, from the previous sections analysis, that TIM and TCCM were the most accurate methods for calculating friction velocity.

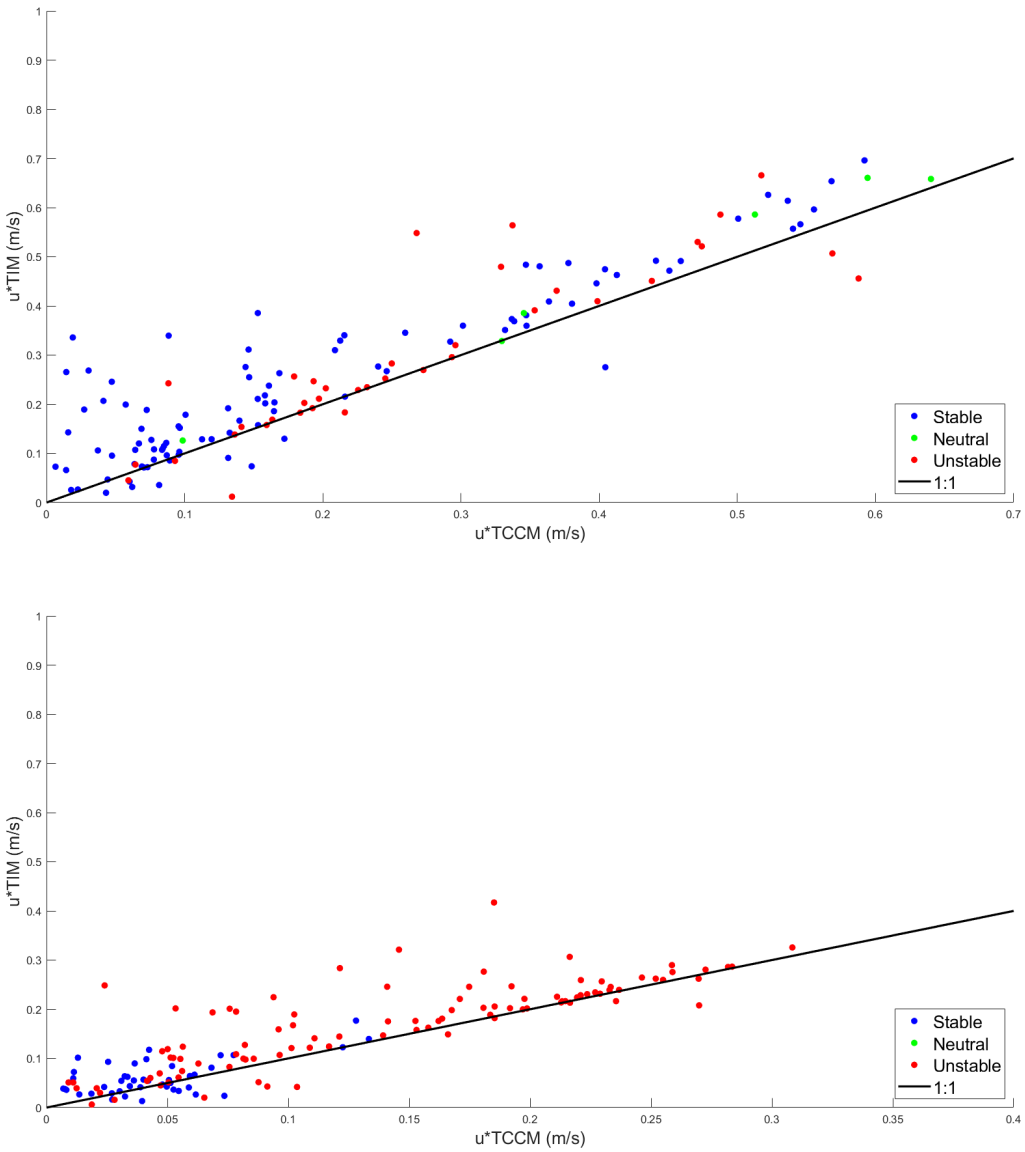

Figure 4.42. From Top to Bottom Friction Velocity calculated using TIM vs Friction Velocity calculated using TCCM for August 14, 2019 and August 15, 2019, respectively. In blue, stable ABL; in green, neutral conditions; and in red, unstable ABL.

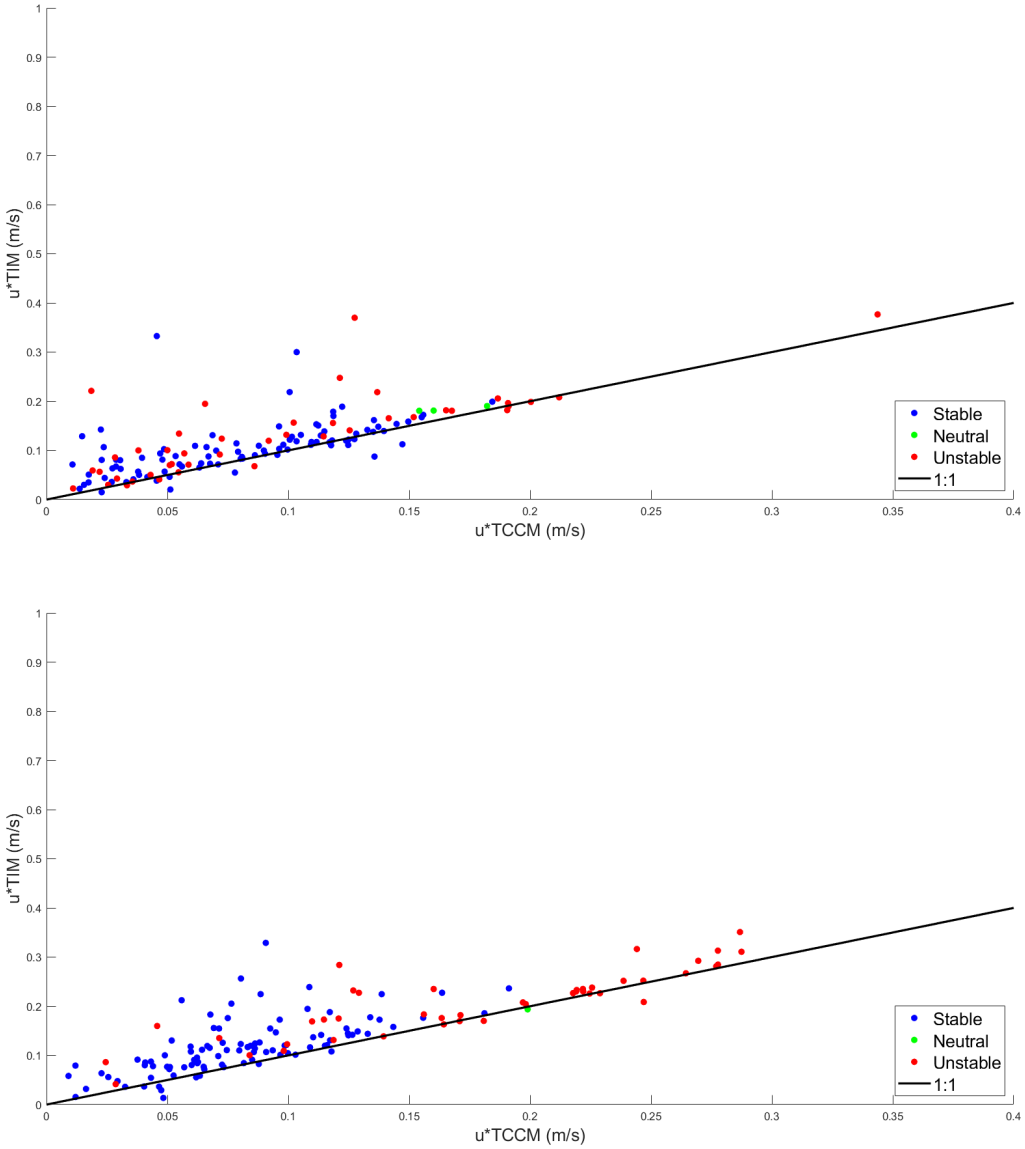

Figure 4.43. From Top to Bottom Friction Velocity calculated using TIM vs Friction Velocity calculated using TCCM for August 16, 2019 and August 17, 2019, respectively. In blue, stable ABL; in green, neutral conditions; and in red, unstable ABL.

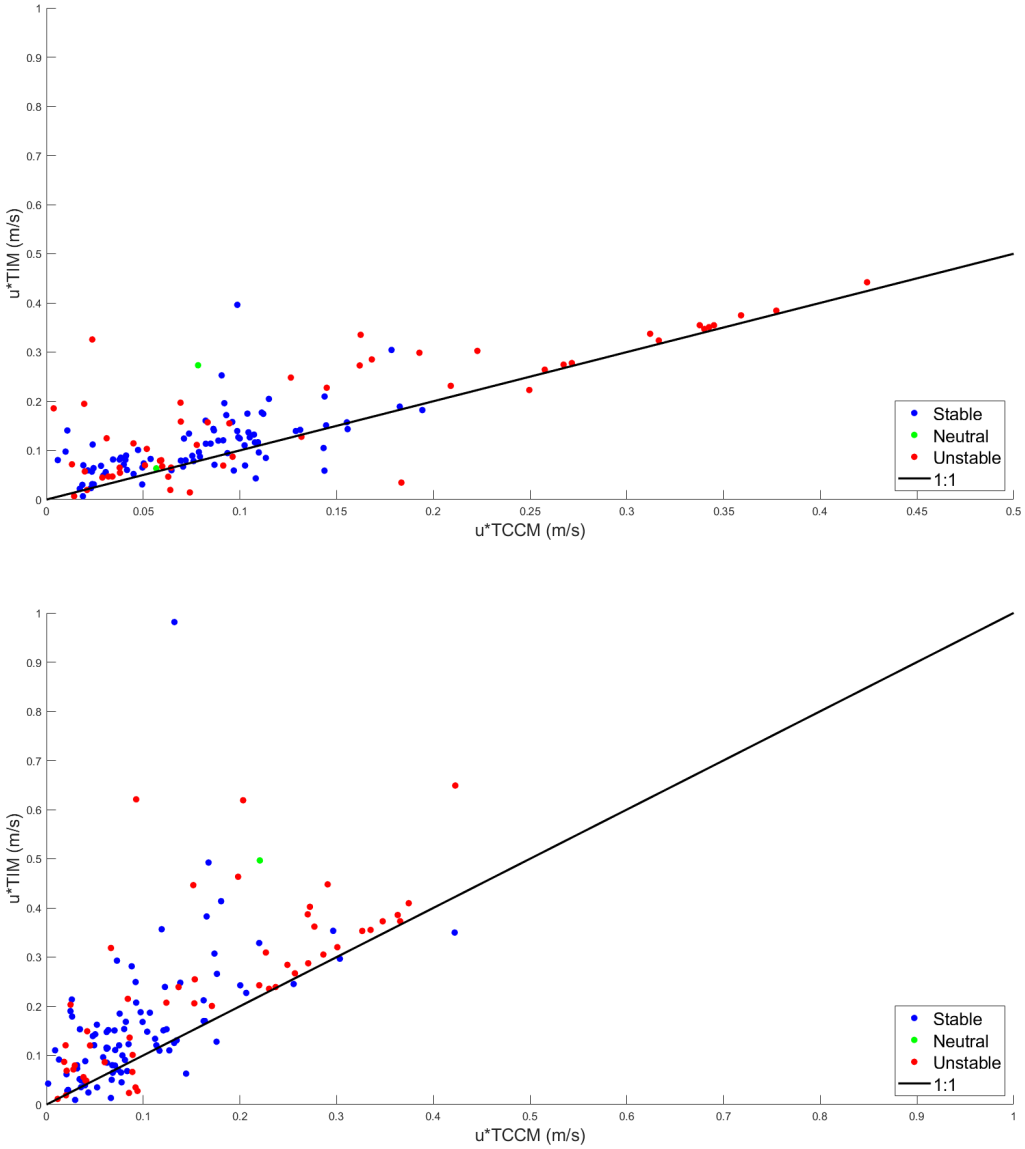

Figure 4.44. From Top to Bottom Friction Velocity calculated using TIM vs Friction Velocity calculated using TCCM for August 18, 2019 and August 19, 2019, respectively. In blue, stable ABL; in green, neutral conditions; and in red, unstable ABL.

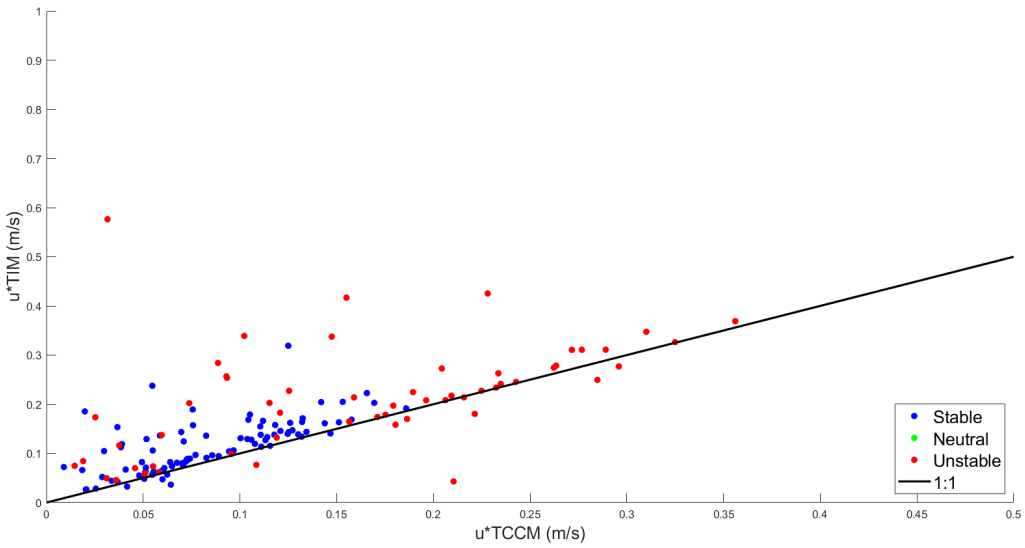

Figure 4.45. Friction Velocity calculated using TIM vs Friction Velocity calculated using TCCM for August 20, 2019. In blue, stable ABL; in green, neutral conditions; and in red, unstable ABL.

In most of the above plots we can see that u^*_{tim}values are greater than u^*_{tccm} values. Overall, it is not clear for what MABL conditions TIM replicates best TCCM, but it seems that unstable state leads to increased shear stress while stable state leads to decreased shear stress.

Friction velocity versus horizontal wind velocity was plotted once again in this section, this time accounting for the different MABL stability states. Results can be found in figure 4.46

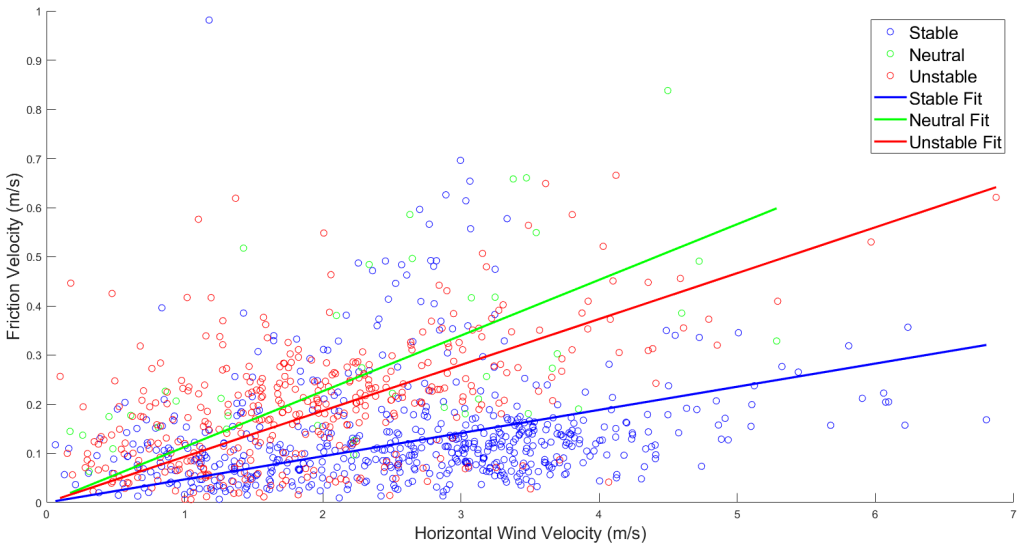

Figure 4.46. Friction velocity versus horizontal wind velocity for August 14-20, 2019 classified by stability states.

Table 4.5 collects the slope for each of the fitted lines obtained for each of the different MABL stability states.

Table 4.5. Fitted line slope for August 14-20, 2019 accounting for different MABL stability states.

Stability State	**Fitted Line Slope**
Stable	0.047
Neutral	0.113
Unstable	0.093

Figure 4.46 show the same exact plot as figure 4.40 but this time accounting for the different MABL stability states. As it is presented in table 4.5, the fitted line slope for stable state is 0.047, which is really similar to the second phase fitted line from figure 4.41. Unstable and neutral fitted line slopes are much greater, 0.113 and 0.093, respectively, and much greater than the fitted lines from the literature.

CHAPTER 5

CONCLUSION AND FUTURE RESEARCH

This work has covered a range of topics expected to provide the reader with a greater understanding on how variables such as wind velocity, temperature, Reynolds stresses, heat flux, friction velocity, MABL stability conditions, among others vary throughout the day in the MABL.

Main conclusions include: that no dominant component of the Reynolds shear stress was found, as the magnitudes of u'w', u'v' and v'w' are similar for most of the days analyzed as it can be seen in figures 4.24-4.30. For the majority of the days analyzed, the Reynolds stresses are greater in the second part of the day. Turbulent heat fluxes are also nominally greater the second half of the day for most days.

Friction velocity computed from the three different methods studied in this thesis are similar for the days analyzed. Table 4.3 compares these three methods based on MSE criteria and shows that when comparing these three methods, MSE values close to 0 to every day of data analyzed. Nevertheless, owing to predicted alignment challenges, only the TIM and the TCCM should be considered to calculate friction velocity. As seen in the Reynolds stress analysis, friction velocity values tend to be greater for the three methods in the second part of the day.

Friction velocity versus horizontal wind velocity was also plotted and the results can be found in figures 4.36 to 4.41. These results were then compared to literature values that can be seen in figure 4.42. It seems that the second phase fitted line found in the literature is much similar that the first phase fitted line found in the literature for all these plots, given the fitted line slopes obtained from this analysis and presented in table 4.4. In terms of MABL stability, it is obvious from the results obtained and that can be seen in figure 4.46 and table 4.5 that for stable state the fitted line is very similar to the second phase fitted line found in the literature. For unstable and neutral states, these fitted lines are much different that what is shown in the literature.

The Monin-Obukhov Similarity Theory (MOST) was analyzed and one of the most important findings obtained from this analysis, is that the friction velocity obtained using the TIM is greater than the friction velocity obtained using the TCCM. Also, it seems that unstable state leads to increased shear stress while stable state leads to decreased shear stress. Lastly, it is unclear from the analysis for what ABL stability conditions does TIM replicates best TCCM for calculating friction velocity.

In terms of future research, there are some topics that would be interesting to further develop. For instance, creating a model that predicts turbulence in the areas where the sonic anemometers captured velocity and temperature data. Exploring the appliance of the MOST theory for ABL stable conditions since it was found that the friction velocity values obtained following the TIM differ, in a higher proportion than when experiencing ABL unstable conditions, for most of the days. Finally, the intend is to explore the comparison of values obtained for the different variables that are analyzed in this thesis for the two different locations where sonic anemometers were installed, Wood Island, NH and Portsmouth Coast, NH, with the purpose of understanding how these variables change from open ocean conditions compared to coastal conditions.

BIBLIOGRAPHY

[1] D. Chalikov. The parameterization of the wave boundary layer*. 1994.

[2] Jonsaon rvar G. Wave boundary layers amd friction factors. 1966.

[3] Dario Camuffo. Atmospheric stability and pollutant dispersion. *Microclimate for Cultural Heritage*, 2014.

[4] Oncley S. P. Stage S. A. Wilczak, J. M. Sonic anemometer tilt correction algorithms. boundary-layer meteorology. 99(1):127–150, 2001.

[5] CHERYL KLIPP. Turbulent friction velocity calculated from the reynolds stress tensor. 2017.

[6] Venkatesh D. Jothiprakasam Hendri J. Breedt a, Ken J. Craig a. Monin-obukhov similarity theory and its application to wind flow modelling over complex terrain. 2018.

[7] Ivan Marusic · Jason Monty Joseph Klewicki Nicholas Hutchins, Kapil Chauhan. Towards reconciling the large-scale structure of turbulent boundary layers in the atmosphere and laboratory. 2012.

[8] Domingo Muñoz-Esparza Joachim Reuder Jaak Monbaliu Jeroen van Beeck and Nicole van Lipzig Sara Porchetta, Orkun Temel. A new roughness length parameterization accounting forwind–wave (mis)alignment. 2019.

[9] Michael Yost. Fluids and solids: Fundamentals. 2004.

[10] Nancy Hall. Boundary layer. 2015.

[11] David Weyburne. Boundary layer thickness. 2016.

[12] J. W. Miles. On the generation of surface waves by shear flows. *Journal of Fluid Mechanics*, 1957.

[13] Alexander S. Boeckenstedt. Validation of h alidation of hts optical t s optical turbulence pr urbulence profiling via sonic ofiling via sonic anemometry. 2020.

[14] Weather Underground. Newington, nh weather history. 2019.

[15] mit.edu. Basics of turbulent flow.

[16] S. Ferrarese-M. Manfrin R. Richiardone, E. Giampiccolo. Use of the planar fit method in tilt and distortion analysis of themean flow. 2002.

[17] James B. Edson et al. On the exchange of momentum over the open ocean. *JOURNAL OF PHYSICAL OCEANOGRAPHY*, 2013.

APPENDIX A

DAILY HISTORICAL WEATHER DATA FOR NEWINGTON, NH

Table A.1. Newington, NH Weather History for August 14, 2019 [14].

14-Aug-19							
Time	**Temperature (K)**	**Humidity**	**Wind**	**Wind Speed (m/s)**	**Pressure (Hg)**	**Precipitation (in)**	**Condition**
11:56 PM	293.2	98 %	NE	1.3	29.67	0.0	Mostly Cloudy
12:07 AM	293.2	94 %	CALM	0.0	29.66	0.0	Fog
12:16 AM	293.2	100 %	CALM	0.0	29.66	0.0	Fog
12:30 AM	293.2	100 %	CALM	0.0	29.67	0.0	Cloudy
12:56 AM	293.7	100 %	N	2.7	29.66	0.0	Fog
1:17 AM	293.2	100 %	N	2.7	29.66	0.0	Mostly Cloudy
1:56 AM	293.7	97 %	N	2.7	29.67	0.0	Mostly Cloudy
2:13 AM	293.2	94 %	NNE	2.7	29.67	0.0	Partly Cloudy
2:56 AM	292.6	89 %	N	3.6	29.67	0.0	Fair
3:56 AM	290.9	87 %	N	3.1	29.68	0.0	Fair
4:56 AM	290.4	82 %	N	3.6	29.70	0.0	Fair
5:56 AM	290.9	73 %	NNE	2.7	29.72	0.0	Partly Cloudy
6:56 AM	292.0	72 %	N	3.1	29.73	0.0	Mostly Cloudy
7:56 AM	293.7	64 %	NNE	3.1	29.75	0.0	Mostly Cloudy
8:56 AM	294.8	62 %	NNE	3.6	29.75	0.0	Mostly Cloudy
9:56 AM	295.9	60 %	NE	3.6	29.76	0.0	Mostly Cloudy
10:56 AM	295.4	62 %	ENE	3.1	29.75	0.0	Mostly Cloudy
11:56 AM	296.5	58 %	ENE	3.6	29.75	0.0	Mostly Cloudy
12:56 PM	296.5	61 %	E	2.7	29.75	0.0	Partly Cloudy
1:56 PM	296.5	69 %	SE	3.6	29.76	0.0	Mostly Cloudy
2:56 PM	295.9	69 %	SE	3.1	29.76	0.0	Mostly Cloudy
3:56 PM	294.8	72 %	ESE	3.6	29.77	0.0	Mostly Cloudy
4:56 PM	294.3	72 %	ESE	3.6	29.78	0.0	Mostly Cloudy
5:56 PM	292.6	81 %	ESE	4.0	29.78	0.0	Partly Cloudy
6:56 PM	291.5	88 %	SSE	2.2	29.79	0.0	Fair
7:56 PM	290.9	91 %	CALM	0.0	29.80	0.0	Fair
8:56 PM	290.4	94 %	CALM	0.0	29.81	0.0	Partly Cloudy
9:56 PM	289.8	94 %	CALM	0.0	29.82	0.0	Mostly Cloudy
10:56 PM	289.8	97 %	CALM	0.0	29.84	0.0	Mostly Cloudy

Table A.2. Newington, NH Weather History for August 15, 2019 [14].

15-Aug-19							
Time	**Temperature (K)**	**Humidity**	**Wind**	**Wind Speed (m/s)**	**Pressure (Hg)**	**Precipitation (in)**	**Condition**
11:56 PM	289.8	96 %	CALM	0.0	29.85	0.0	Mostly Cloudy
12:56 AM	289.3	96 %	NW	2.2	29.85	0.0	Mostly Cloudy
1:56 AM	289.3	97 %	CALM	0.0	29.85	0.0	Mostly Cloudy
2:56 AM	288.2	98 %	CALM	0.0	29.87	0.0	Partly Cloudy
3:43 AM	288.2	100 %	CALM	0.0	29.87	0.0	Fog
3:48 AM	288.2	100 %	CALM	0.0	29.87	0.0	Fog
3:56 AM	288.2	99 %	CALM	0.0	29.87	0.0	Fog
4:15 AM	288.2	100 %	CALM	0.0	29.88	0.0	Fog
4:56 AM	289.3	99 %	CALM	0.0	29.89	0.0	Fog
5:22 AM	288.2	100 %	CALM	0.0	29.89	0.0	Fog
5:31 AM	288.2	100 %	CALM	0.0	29.89	0.0	Fog
5:56 AM	289.3	100 %	CALM	0.0	29.9	0.0	Mostly Cloudy
6:06 AM	290.4	100 %	N	1.3	29.9	0.0	Partly Cloudy
6:56 AM	290.9	100 %	CALM	0.0	29.91	0.0	Mostly Cloudy
7:56 AM	291.5	100 %	ENE	1.3	29.93	0.0	Mostly Cloudy
8:56 AM	292.6	72 %	CALM	0.0	29.94	0.0	Mostly Cloudy
9:56 AM	294.8	62 %	E	3.6	29.95	0.0	Mostly Cloudy
10:56 AM	295.9	56 %	ESE	3.1	29.95	0.0	Mostly Cloudy
11:56 AM	295.9	53 %	E	3.1	29.94	0.0	Fair
12:56 PM	296.5	53 %	E	3.1	29.93	0.0	Fair
1:56 PM	296.5	54 %	ESE	3.6	29.92	0.0	Fair
2:56 PM	296.5	59 %	SE	4.0	29.92	0.0	Fair
3:56 PM	295.4	64 %	ESE	3.1	29.91	0.0	Fair
4:56 PM	294.3	70 %	SE	3.1	29.91	0.0	Fair
5:56 PM	292.6	82 %	SE	3.6	29.92	0.0	Mostly Cloudy
6:56 PM	291.5	92 %	SSE	2.7	29.93	0.0	Mostly Cloudy
7:56 PM	290.9	95 %	SE	2.2	29.94	0.0	Mostly Cloudy
8:47 PM	290.4	100 %	S	2.2	29.95	0.0	Mostly Cloudy
8:56 PM	290.4	97 %	S	2.2	29.94	0.0	Mostly Cloudy
9:56 PM	290.4	97 %	CALM	0.0	29.94	0.0	Cloudy
10:56 PM	290.9	96 %	CALM	0.0	29.96	0.0	Cloudy

Table A.3. Newington, NH Weather History for August 16, 2019 [14].

16-Aug-19							
Time	**Temperature (K)**	**Humidity**	**Wind**	**Wind Speed (m/s)**	**Pressure (Hg)**	**Precipitation (in)**	**Condition**
11:51 PM	290.4	100 %	CALM	0.0	29.96	0.0	Cloudy
11:56 PM	290.4	97 %	CALM	0.0	29.95	0.0	Cloudy
12:50 AM	290.4	100 %	CALM	0.0	29.94	0.0	Fog
12:56 AM	290.4	98 %	CALM	0.0	29.95	0.0	Fog
1:30 AM	290.4	100 %	CALM	0.0	29.93	0.0	Fog
1:44 AM	290.4	100 %	CALM	0.0	29.93	0.0	Fog
1:56 AM	289.8	99 %	SE	1.3	29.93	0.0	Fog
2:19 AM	290.4	100 %	CALM	0.0	29.93	0.0	Fog
2:56 AM	289.8	100 %	CALM	0.0	29.93	0.0	Fog
3:36 AM	290.4	100 %	CALM	0.0	29.93	0.0	Fog
3:56 AM	290.4	100 %	CALM	0.0	29.93	0.0	Fog
4:46 AM	290.4	100 %	ENE	2.2	29.93	0.0	Fog
4:49 AM	290.4	100 %	ENE	2.7	29.93	0.0	Light Rain
4:56 AM	290.4	100 %	E	3.1	29.93	0.0	Light Rain
5:02 AM	290.4	100 %	E	2.7	29.93	0.0	Fog
5:34 AM	290.4	100 %	E	1.3	29.93	0.0	Fog
5:56 AM	290.4	100 %	ENE	2.2	29.93	0.0	Fog
6:04 AM	290.4	100 %	ESE	2.2	29.93	0.0	Fog
6:19 AM	290.4	100 %	E	2.2	29.93	0.0	Fog
6:35 AM	290.4	100 %	ESE	2.7	29.93	0.0	Fog
6:56 AM	290.4	100 %	SE	2.7	29.93	0.0	Fog
7:12 AM	290.9	100 %	CALM	0.0	29.93	0.0	Fog
7:36 AM	290.9	100 %	E	2.2	29.93	0.0	Cloudy
7:56 AM	292.0	100 %	ESE	1.3	29.93	0.0	Mostly Cloudy
8:11 AM	292.0	94 %	CALM	0.0	29.93	0.0	Mostly Cloudy
8:56 AM	293.7	81 %	SE	3.1	29.93	0.0	Mostly Cloudy
9:56 AM	295.4	73 %	E	2.7	29.93	0.0	Mostly Cloudy
10:56 AM	296.5	71 %	SE	2.2	29.93	0.0	Mostly Cloudy
11:56 AM	296.5	74 %	E	4.0	29.93	0.0	Mostly Cloudy
12:56 PM	295.9	71 %	E	4.5	29.93	0.0	Mostly Cloudy
2:56 PM	295.9	74 %	ESE	4.5	29.93	0.0	Mostly Cloudy
3:56 PM	293.7	80 %	ESE	5.4	29.93	0.0	Mostly Cloudy
4:56 PM	293.7	81 %	ESE	4.5	29.93	0.0	Mostly Cloudy
5:56 PM	292.6	86 %	ESE	4.0	29.93	0.0	Mostly Cloudy
6:56 PM	291.5	91 %	E	3.1	29.93	0.0	Mostly Cloudy
7:31 PM	290.9	94 %	E	3.1	29.93	0.0	Mostly Cloudy
7:56 PM	291.5	93 %	ESE	2.7	29.93	0.0	Mostly Cloudy
8:08 PM	290.9	94 %	ESE	2.7	29.93	0.0	Cloudy
8:56 PM	291.5	95 %	E	2.7	29.93	0.0	Cloudy
9:31 PM	290.9	100 %	ESE	3.1	29.93	0.0	Cloudy
9:48 PM	290.9	100 %	ESE	2.7	29.93	0.0	Mostly Cloudy
9:56 PM	291.5	96 %	E	2.2	29.93	0.0	Mostly Cloudy
10:05 PM	290.9	100 %	E	2.2	29.93	0.0	Cloudy
10:38 PM	292.0	94 %	ESE	3.1	29.93	0.0	Cloudy
10:56 PM	291.5	96 %	ESE	3.6	29.93	0.0	Cloudy

Table A.4. Newington, NH Weather History for August 17, 2019 [14].

17-Aug-19							
Time	**Temperature (K)**	**Humidity**	**Wind**	**Wind Speed (m/s)**	**Pressure (Hg)**	**Precipitation (in)**	**Condition**
11:56 PM	291.5	96 %	SE	4.0	29.95	0.0	Cloudy
12:12 AM	292.0	94 %	SE	3.6	29.95	0.0	Cloudy
12:56 AM	292.0	96 %	SE	3.6	29.96	0.0	Cloudy
1:44 AM	292.0	94 %	S	2.2	29.96	0.0	Cloudy
1:56 AM	292.0	97 %	SSE	3.1	29.96	0.0	Cloudy
2:56 AM	292.0	96 %	SE	2.7	29.96	0.0	Cloudy
3:24 AM	292.0	94 %	SE	1.3	29.96	0.0	Cloudy
3:56 AM	292.0	97 %	E	2.2	29.96	0.0	Cloudy
4:07 AM	292.0	94 %	ESE	1.3	29.96	0.0	Cloudy
4:33 AM	292.0	94 %	SSE	2.7	29.96	0.0	Cloudy
4:56 AM	291.5	96 %	SE	3.1	29.95	0.0	Cloudy
5:11 AM	292.0	94 %	SE	3.1	29.95	0.0	Cloudy
5:51 AM	292.0	94 %	SE	2.7	29.95	0.0	Cloudy
5:56 AM	292.0	94 %	SE	3.1	29.95	0.0	Cloudy
6:25 AM	292.0	94 %	SE	3.1	29.95	0.0	Cloudy
6:56 AM	292.6	94 %	SSE	2.7	29.96	0.0	Cloudy
7:41 AM	293.2	94 %	SSE	3.6	29.96	0.0	Cloudy
7:56 AM	292.6	94 %	SSE	3.6	29.95	0.0	Cloudy
8:01 AM	293.2	94 %	SSE	3.1	29.95	0.0	Cloudy
8:56 AM	293.2	93 %	SE	3.1	29.96	0.0	Cloudy
9:11 AM	293.2	94 %	SSE	3.1	29.95	0.0	Cloudy
9:56 AM	293.7	91 %	SE	4.0	29.95	0.0	Cloudy
10:11 AM	293.2	94 %	SSE	4.0	29.95	0.0	Cloudy
10:56 AM	293.7	88 %	SSE	4.0	29.96	0.0	Cloudy
11:11 AM	294.3	88 %	SE	4.0	29.95	0.0	Cloudy
11:56 AM	294.3	87 %	SSE	4.5	29.96	0.0	Cloudy
12:17 PM	294.3	88 %	SE	4.5	29.95	0.0	Cloudy
12:47 PM	294.3	88 %	SSE	4.0	29.95	0.0	Cloudy
12:56 PM	294.8	84 %	SSE	4.0	29.95	0.0	Cloudy
1:16 PM	294.3	88 %	SE	4.5	29.96	0.0	Cloudy
1:56 PM	294.8	86 %	SE	3.6	29.95	0.0	Cloudy
2:16 PM	295.4	83 %	ESE	3.6	29.94	0.0	Mostly Cloudy
2:36 PM	295.4	83 %	E	3.6	29.93	0.0	Cloudy
2:56 PM	295.4	84 %	ESE	3.1	29.92	0.0	Cloudy
3:56 PM	294.8	86 %	SE	4.5	29.90	0.0	Cloudy
4:56 PM	293.7	88 %	E	4.0	29.89	0.0	Cloudy
5:32 PM	293.2	94 %	ESE	3.6	29.89	0.0	Cloudy
5:56 PM	293.2	93 %	ESE	2.7	29.89	0.0	Mostly Cloudy
6:56 PM	292.6	95 %	E	2.7	29.89	0.0	Cloudy
7:36 PM	293.2	94 %	ESE	3.6	29.89	0.0	Cloudy
7:56 PM	292.6	97 %	ESE	3.1	29.90	0.0	Cloudy
8:56 PM	293.2	96 %	E	2.7	29.91	0.0	Cloudy
9:32 PM	293.2	94 %	E	2.2	29.90	0.0	Cloudy
9:56 PM	292.6	97 %	ESE	3.6	29.89	0.0	Thunder in the Vicinity
10:06 PM	293.2	94 %	ESE	3.1	29.89	0.0	T-Storm
10:27 PM	293.2	94 %	ESE	3.1	29.88	0.0	Light Rain
10:56 PM	292.6	99 %	CALM	0.0	29.88	0.1	Light Rain

Table A.5. Newington, NH Weather History for August 18, 2019 [14].

18-Aug-19							
Time	**Temperature (K)**	**Humidity**	**Wind**	**Wind Speed (m/s)**	**Pressure (Hg)**	**Precipitation (in)**	**Condition**
11:36 PM	293.2	100 %	CALM	0.0	29.88	0.0	Cloudy
11:56 PM	292.6	99 %	SE	2.7	29.88	0.0	Cloudy
12:56 AM	292.6	98 %	CALM	0.0	29.88	0.0	Cloudy
1:56 AM	292.0	99 %	CALM	0.0	29.87	0.0	Mostly Cloudy
2:56 AM	292.0	100 %	CALM	0.0	29.86	0.0	Cloudy
3:24 AM	292.0	100 %	CALM	0.0	29.86	0.0	Cloudy
3:56 AM	291.5	100 %	CALM	0.0	29.86	0.0	Mostly Cloudy
4:25 AM	290.9	100 %	CALM	0.0	29.87	0.0	Cloudy
4:56 AM	292.0	100 %	CALM	0.0	29.88	0.0	Fog
5:26 AM	292.0	100 %	CALM	0.0	29.88	0.0	Fog
5:49 AM	292.0	100 %	CALM	0.0	29.88	0.0	Fog
5:56 AM	292.0	100 %	CALM	0.0	29.89	0.0	Fog
6:12 AM	292.0	100 %	CALM	0.0	29.89	0.0	Fog
6:18 AM	293.2	100 %	W	1.3	29.89	0.0	Fog
6:25 AM	293.2	100 %	W	1.3	29.89	0.0	Fog
6:37 AM	293.2	100 %	CALM	0.0	29.89	0.0	Fog
6:47 AM	293.2	100 %	CALM	0.0	29.89	0.0	Cloudy
6:56 AM	293.2	100 %	W	1.3	29.89	0.0	Mostly Cloudy
7:37 AM	294.3	94 %	CALM	0.0	29.91	0.0	Cloudy
7:42 AM	294.3	94 %	VAR	1.3	29.90	0.0	Cloudy
7:56 AM	294.8	91 %	W	2.2	29.90	0.0	Cloudy
8:56 AM	294.8	89 %	W	2.7	29.91	0.0	Cloudy
9:06 AM	295.4	88 %	W	2.2	29.91	0.0	Cloudy
9:26 AM	295.4	83 %	W	2.2	29.91	0.0	Mostly Cloudy
9:56 AM	296.5	80 %	SW	2.2	29.90	0.0	Mostly Cloudy
10:05 AM	295.9	83 %	W	1.3	29.90	0.0	Mostly Cloudy
10:56 AM	298.2	75 %	CALM	0.0	29.89	0.0	Mostly Cloudy
11:56 AM	300.4	68 %	CALM	0.0	29.87	0.0	Mostly Cloudy
12:56 PM	299.8	69 %	ESE	2.7	29.87	0.0	Mostly Cloudy
1:56 PM	299.8	69 %	SE	3.1	29.88	0.0	Mostly Cloudy
2:56 PM	299.8	69 %	SE	4.0	29.87	0.0	Partly Cloudy
3:56 PM	297.6	75 %	ESE	5.8	29.86	0.0	Partly Cloudy
4:56 PM	295.9	81 %	SE	5.4	29.87	0.0	Partly Cloudy
5:56 PM	294.8	90 %	SE	4.0	29.86	0.0	Mostly Cloudy
6:28 PM	293.2	100 %	ESE	3.6	29.87	0.0	Cloudy
6:56 PM	293.2	97 %	ESE	3.1	29.86	0.0	Cloudy
7:11 PM	293.2	100 %	ESE	3.1	29.87	0.0	Fog
7:25 PM	293.2	100 %	ESE	3.1	29.86	0.0	Fog
7:33 PM	293.2	100 %	E	2.7	29.86	0.0	Fog
7:56 PM	292.6	100 %	E	2.7	29.86	0.0	Fog
8:41 PM	293.2	100 %	E	2.7	29.87	0.0	Fog
8:56 PM	292.6	100 %	CALM	0.0	29.87	0.0	Fog
9:08 PM	293.2	100 %	E	2.7	29.87	0.0	Light Rain
9:30 PM	293.2	100 %	E	3.1	29.85	0.0	Light Drizzle
9:56 PM	293.7	100 %	ESE	2.7	29.85	0.0	Fog
10:56 PM	293.7	100 %	ESE	1.3	29.84	0.0	T-Storm

Table A.6. Newington, NH Weather History for August 19, 2019 [14].

19-Aug-19							
Time	**Temperature (K)**	**Humidity**	**Wind**	**Wind Speed (m/s)**	**Pressure (Hg)**	**Precipitation (in)**	**Condition**
11:10 PM	294.3	100 %	E	1.3	29.82	0.0	Fog
11:56 PM	294.3	100 %	N	4.0	29.82	0.0	Fog
12:56 AM	294.3	100 %	E	2.7	29.81	0.0	Fog
1:56 AM	293.7	100 %	CALM	0.0	29.82	0.0	Fog
2:56 AM	293.7	100 %	NW	1.3	29.81	0.0	Fog
3:38 AM	294.3	100 %	W	2.2	29.83	0.0	Fog
3:56 AM	294.3	100 %	W	2.2	29.83	0.0	Cloudy
4:13 AM	294.3	100 %	CALM	0.0	29.83	0.0	Fog
4:22 AM	294.3	100 %	W	1.3	29.83	0.0	Fog
4:56 AM	294.3	100 %	W	2.2	29.84	0.0	Fog
5:20 AM	294.3	100 %	WNW	1.3	29.84	0.0	Fog
5:56 AM	294.3	100 %	WSW	1.3	29.83	0.0	Fog
6:20 AM	295.4	100 %	WSW	2.2	29.84	0.0	Fog
6:45 AM	295.4	100 %	W	2.2	29.84	0.0	Fog
6:56 AM	294.8	100 %	WSW	2.7	29.84	0.0	Fog
7:05 AM	295.4	100 %	WSW	2.7	29.84	0.0	Fog
7:10 AM	295.4	100 %	W	2.2	29.83	0.0	Cloudy
7:21 AM	295.9	94 %	SW	3.6	29.83	0.0	Mostly Cloudy
7:31 AM	297.0	89 %	WSW	2.7	29.83	0.0	Mostly Cloudy
7:46 AM	297.0	89 %	WSW	2.2	29.83	0.0	Mostly Cloudy
7:56 AM	297.6	84 %	WSW	2.2	29.83	0.0	Mostly Cloudy
8:56 AM	299.8	73 %	WSW	2.2	29.82	0.0	Partly Cloudy
9:56 AM	302.0	62 %	SW	4.5	29.82	0.0	Partly Cloudy
10:56 AM	302.6	57 %	SW	4.0	29.81	0.0	Partly Cloudy
11:56 AM	303.7	53 %	WSW	3.6	29.79	0.0	Partly Cloudy
12:56 PM	304.8	51 %	WSW	3.6	29.78	0.0	Partly Cloudy
1:56 PM	305.4	47 %	S	3.1	29.75	0.0	Partly Cloudy
2:44 PM	305.4	49 %	SW	3.6	29.74	0.0	Thunder in the Vicinity
2:56 PM	304.3	50 %	W	3.6	29.75	0.0	Thunder in the Vicinity
2:57 PM	304.3	52 %	WNW	6.7	29.76	0.0	Light Rain with Thunder
3:34 PM	297.0	78 %	W	3.6	29.79	0.0	T-Storm
3:44 PM	295.9	88 %	N	3.1	29.77	0.0	T-Storm
3:56 PM	296.5	92 %	N	2.7	29.77	0.1	Light Rain with Thunder
4:01 PM	297.0	89 %	NNE	2.7	29.76	0.0	Thunder in the Vicinity
4:11 PM	297.0	89 %	E	1.3	29.76	0.0	Mostly Cloudy
4:56 PM	297.0	92 %	W	1.3	29.75	0.0	Mostly Cloudy
5:56 PM	297.0	92 %	CALM	0.0	29.76	0.0	Mostly Cloudy
6:56 PM	297.6	86 %	SSW	2.2	29.78	0.0	Partly Cloudy
7:56 PM	297.0	82 %	WSW	3.1	29.80	0.0	Fair
8:56 PM	296.5	83 %	WSW	3.1	29.81	0.0	Fair
9:56 PM	295.9	85 %	WSW	2.7	29.81	0.0	Fair
10:56 PM	295.9	81 %	W	4.0	29.82	0.0	Fair

Table A.7. Newington, NH Weather History for August 20, 2019 [14].

20-Aug-19							
Time	**Temperature (K)**	**Humidity**	**Wind**	**Wind Speed (m/s)**	**Pressure (Hg)**	**Precipitation (in)**	**Condition**
11:56 PM	296.5	73 %	WNW	6.3	29.82	0.0	Fair
12:56 AM	295.4	78 %	WNW	3.1	29.83	0.0	Fair
2:56 AM	293.7	82 %	W	2.7	29.86	0.0	Fair
3:56 AM	293.2	80 %	WSW	3.1	29.87	0.0	Fair
4:56 AM	292.0	85 %	WNW	1.3	29.90	0.0	Fair
5:56 AM	293.2	77 %	CALM	0.0	29.93	0.0	Fair
6:56 AM	294.8	73 %	NW	2.2	29.94	0.0	Fair
7:56 AM	296.5	67 %	NW	3.1	29.94	0.0	Fair
8:56 AM	298.7	59 %	N	1.3	29.95	0.0	Fair
9:56 AM	300.4	51 %	N	2.7	29.95	0.0	Fair
10:56 AM	300.9	50 %	W	2.2	29.94	0.0	Fair
11:56 AM	300.9	43 %	ESE	2.7	29.93	0.0	Fair
12:56 PM	301.5	34 %	SSE	4.5	29.92	0.0	Fair
1:56 PM	301.5	35 %	SSE	4.5	29.92	0.0	Fair
2:56 PM	300.9	37 %	SE	5.4	29.93	0.0	Fair
3:56 PM	300.4	45 %	SSE	4.5	29.92	0.0	Fair
4:56 PM	298.7	48 %	SSE	4.5	29.90	0.0	Fair
5:56 PM	296.5	54 %	SE	3.1	29.91	0.0	Partly Cloudy
6:56 PM	294.8	63 %	SE	3.1	29.91	0.0	Mostly Cloudy
7:56 PM	293.7	67 %	CALM	0.0	29.92	0.0	Mostly Cloudy
8:56 PM	292.6	73 %	CALM	0.0	29.91	0.0	Mostly Cloudy
9:56 PM	291.5	80 %	CALM	0.0	29.91	0.0	Partly Cloudy
10:56 PM	290.9	83 %	CALM	0.0	29.92	0.0	Fair

APPENDIX B

REYNOLDS STRESS U'W' CLASSIFIED BY WIND COMING FROM LAND/OCEAN

As it was defined in the analysis section, it was considered that V+ is 0 degrees and represents wind that goes from west to the east and U+ as 90 degrees and represents wind that goes from south to the north. The rotation is counter-clockwise, so east is in the right, north in the top, west in the left and south in the bottom of the trigonometric plane.

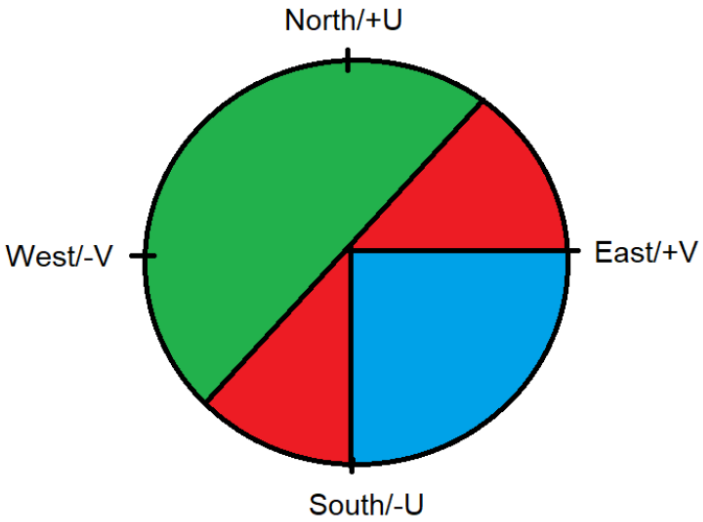

Figure B.1. Representation of wind coming from the land in green, wind coming from the ocean in blue and a mixed region in red. V+ is east and U+ is considered north.

As it can be seen in the image above, it was used between 45 and 225 degrees (green) for the wind from the land, between 270 and 360 degrees (blue) for wind from the ocean and finally an intermediate region (red) that should be partly land partly sea-based wind. In figures B.2 to B.5, it can be found Reynolds stress u'w' classified taking into account wind coming from land or wind coming from ocean. Please note that some of the Reynolds stress magnitudes are much greater for some days than for others, that is the reason of choosing a different scale for each day.

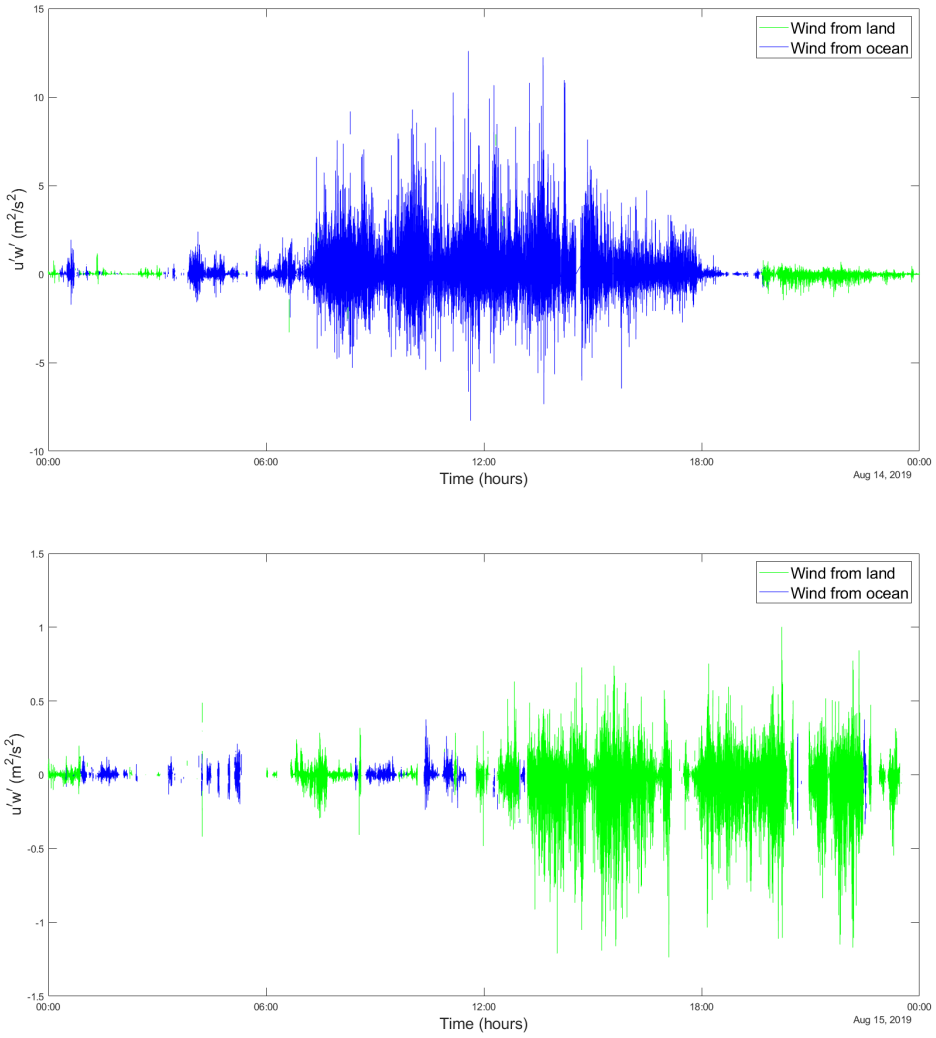

Figure B.2. From Top to Bottom, Reynolds Stress u'w' for August 14, 2019 and August 15, 2019 respectively.

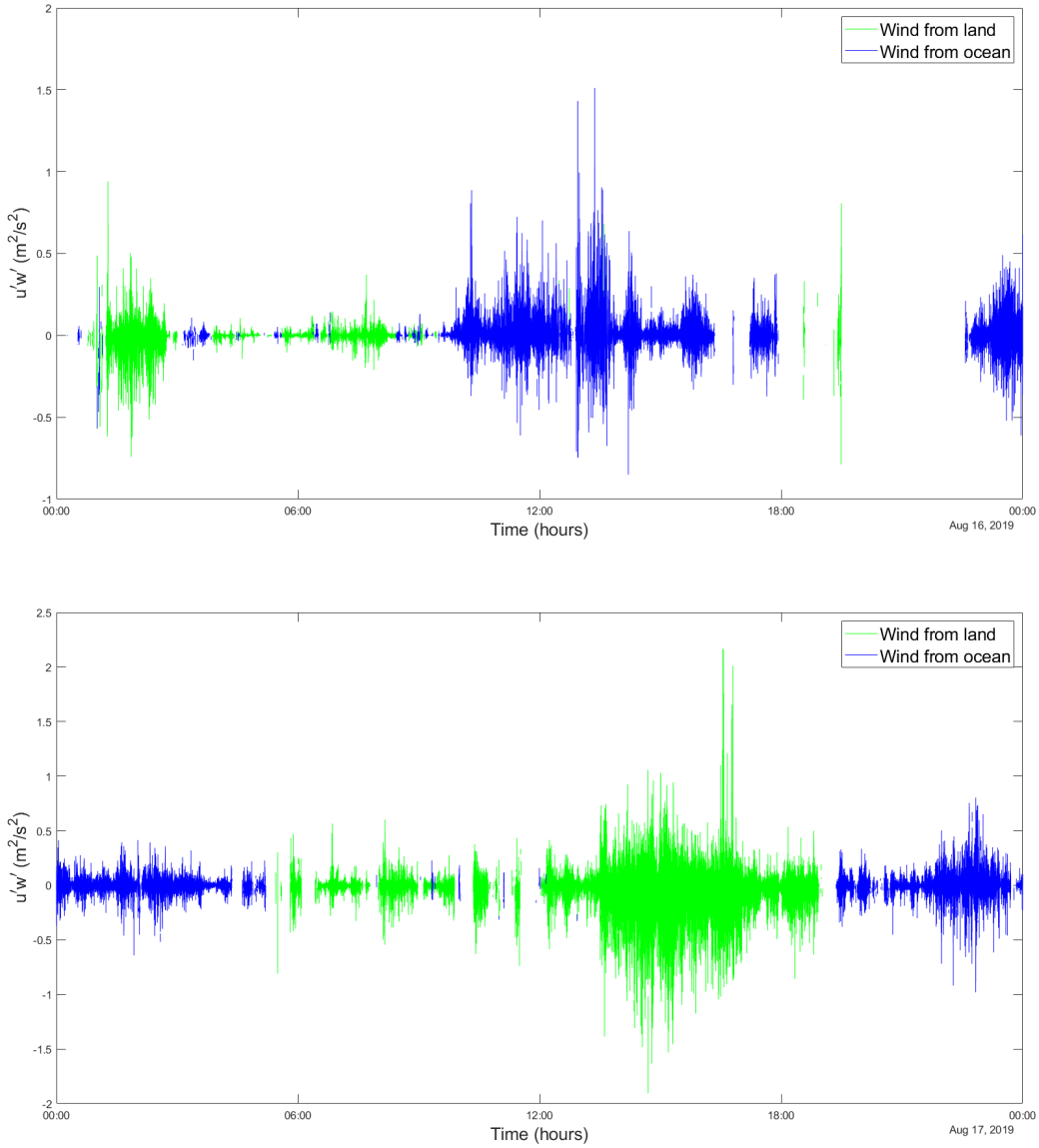

Figure B.3. From Top to Bottom, Reynolds Stress u'w' for August 16, 2019 and August 17, 2019 respectively.

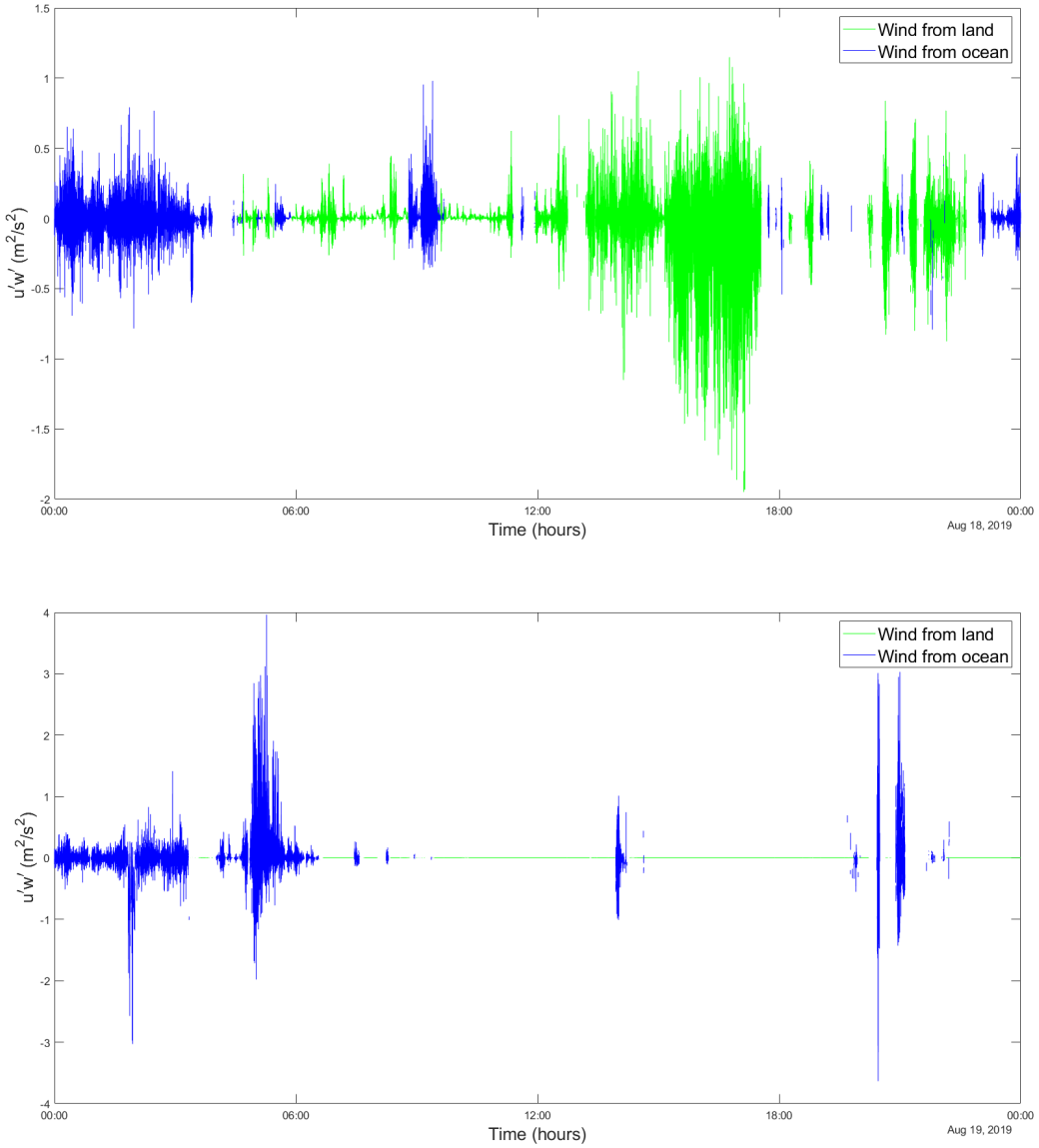

Figure B.4. From Top to Bottom, Reynolds Stress u'w' for August 18, 2019 and August 19, 2019 respectively.

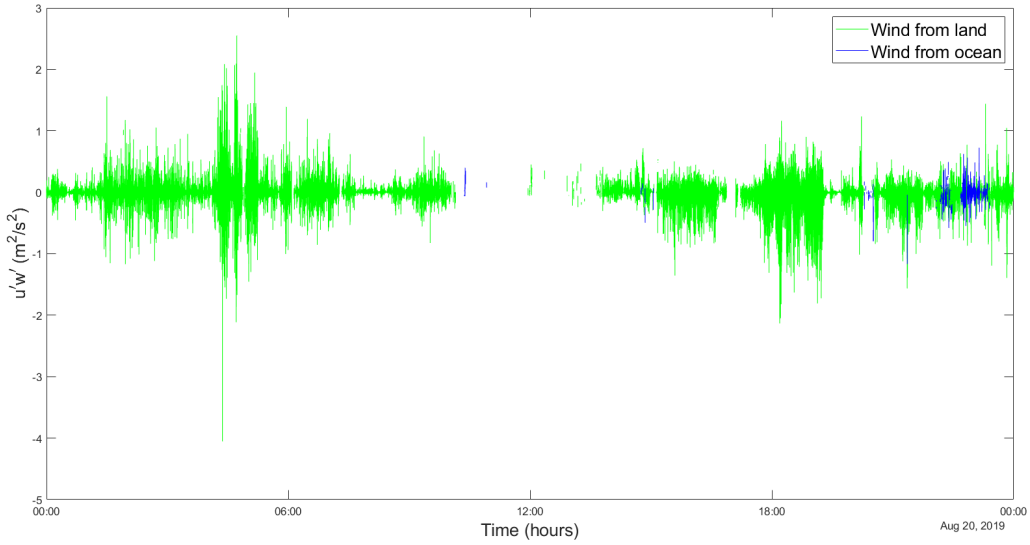

Figure B.5. Reynolds Stress u'w' for August 20, 2019.

APPENDIX C

FRICTION VELOCITY CALCULATED USING THREE DIFFERENT METHODS VERSUS TIME AND HORIZONTAL WIND VELOCITY

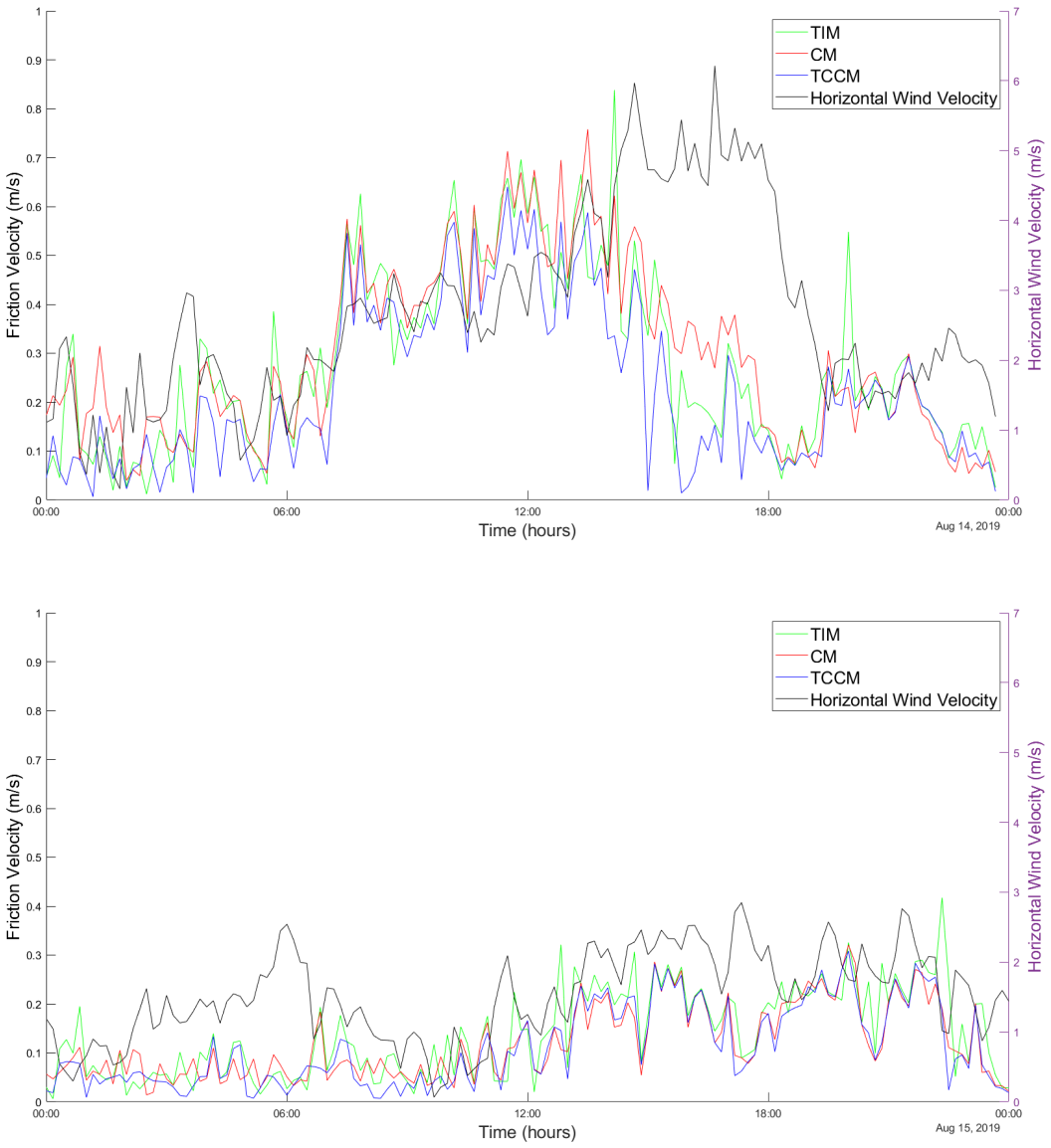

Figure C.1. From Top to Bottom Friction Velocity for August 14, 2019 and August 15, 2019, respectively. In green is represented the friction velocity obtained following the TIM; in red is represented the friction velocity obtained using the CM; in blue is represented the friction velocity obtained using the TCCM; and in black the is represented the horizontal wind velocity.

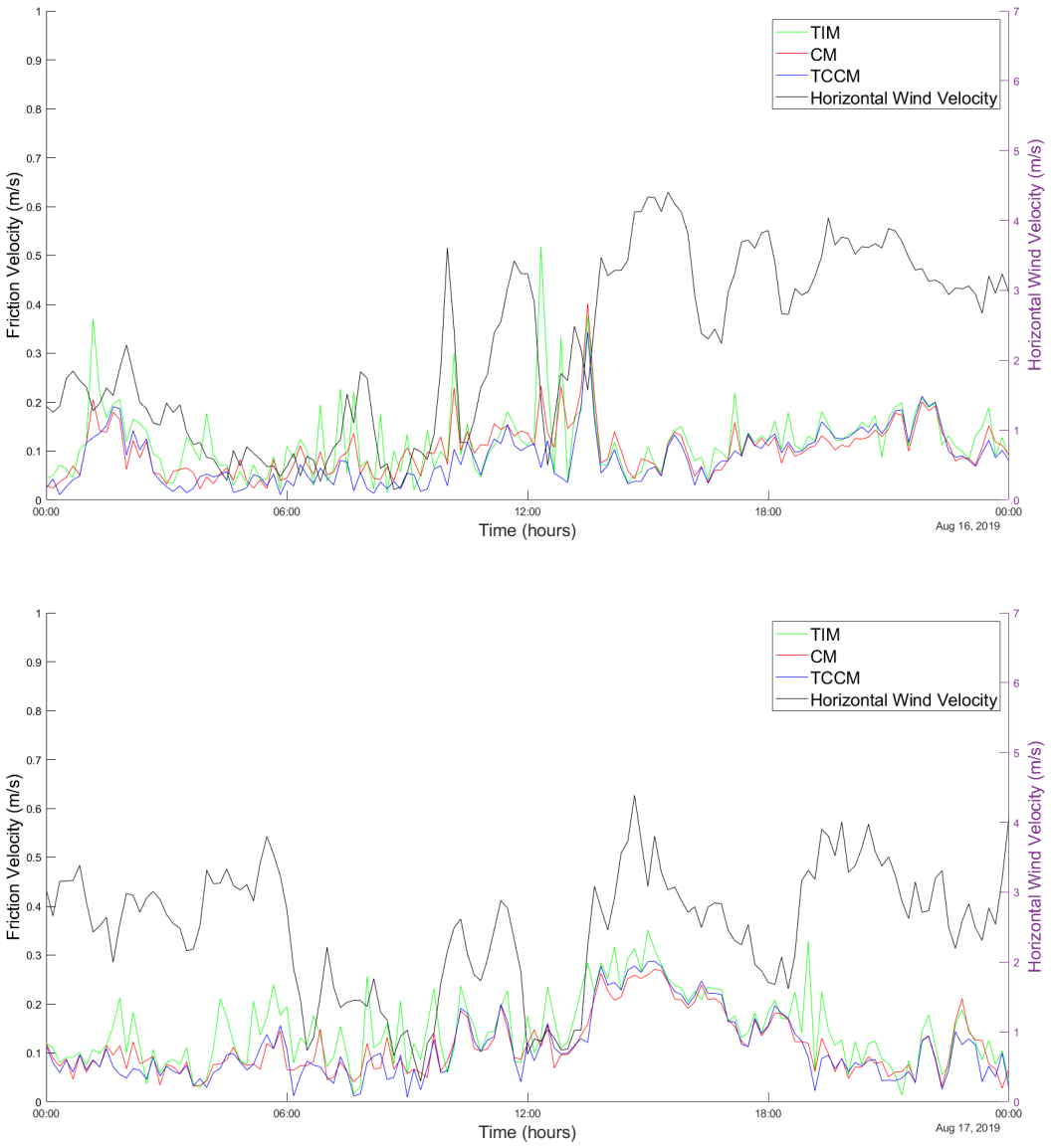

Figure C.2. From Top to Bottom Friction Velocity for August 16, 2019 and August 17, 2019, respectively. In green is represented the friction velocity obtained following the TIM; in red is represented the friction velocity obtained using the CM; in blue is represented the friction velocity obtained using the TCCM; and in black the is represented the horizontal wind velocity.

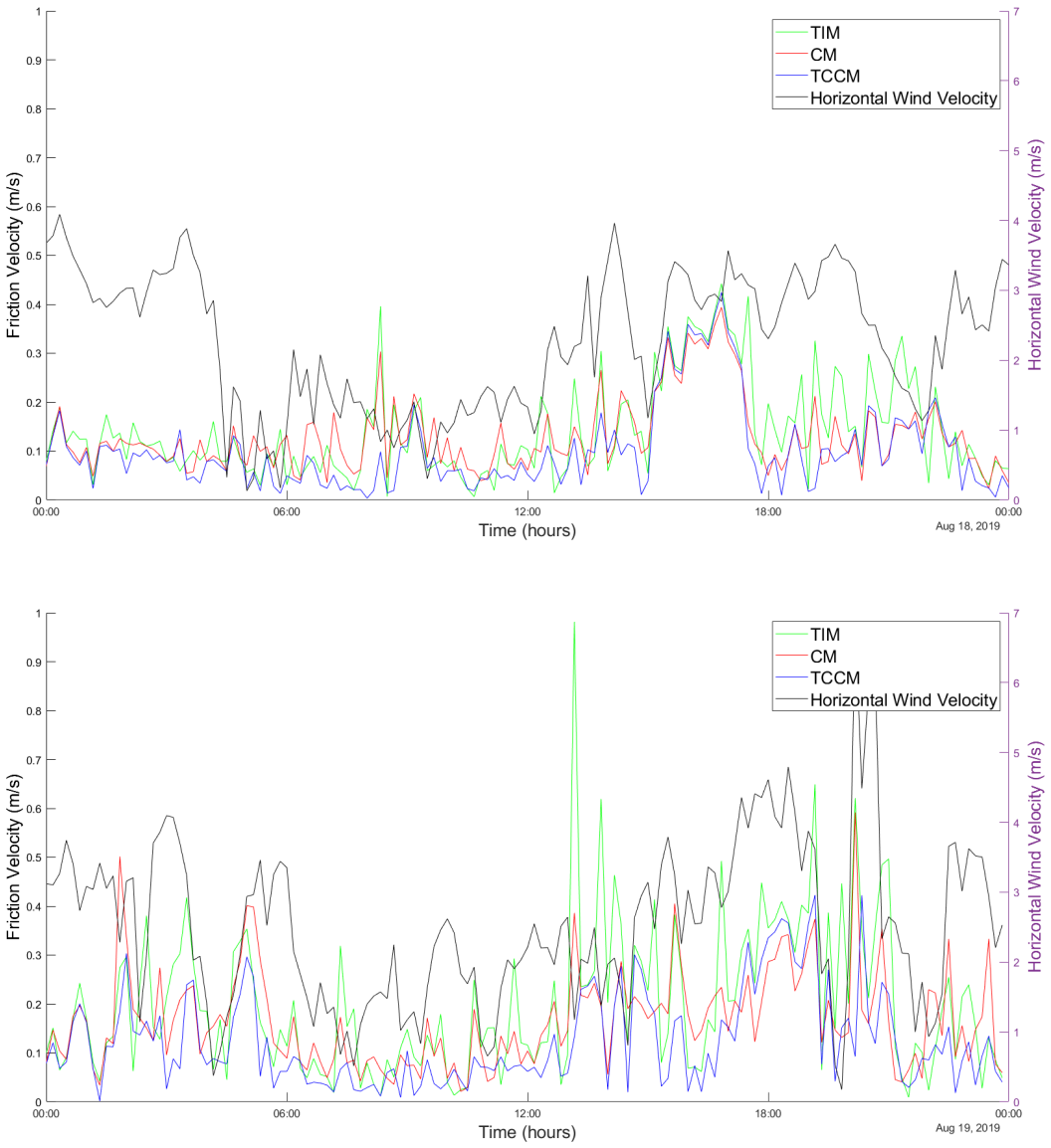

Figure C.3. From Top to Bottom Friction Velocity for August 18, 2019 and August 19, 2019, respectively. In green is represented the friction velocity obtained following the TIM; in red is represented the friction velocity obtained using the CM; in blue is represented the friction velocity obtained using the TCCM; and in black the is represented the horizontal wind velocity.

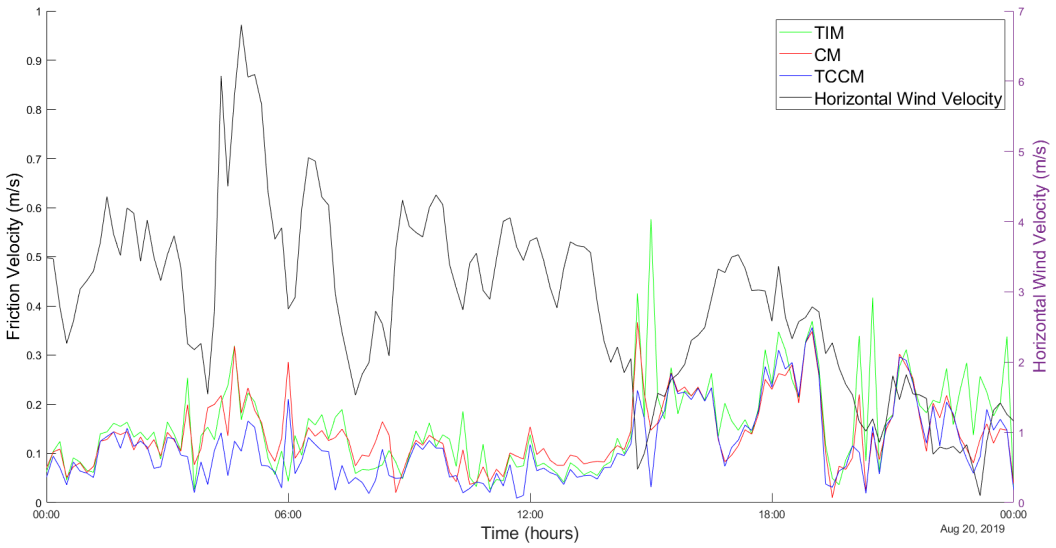

Figure C.4. Friction Velocity for August 20, 2019. In green is represented the friction velocity obtained following the TIM; in red is represented the friction velocity obtained using the CM; in blue is represented the friction velocity obtained using the TCCM; and in black the is represented the horizontal wind velocity.